博 士 学 位 論 文
Doctoral Thesis

論文題目

Thesis Title

Synergy-Based Transferable Control Strategies for Natural Elbow Motion Generation in Transhumeral Prosthesis

東 北 大 学 大 学 院 工 学 研 究 科

Graduate School of Engineering,

TOHOKU UNIVERSITY

専攻/Department: Robotics

学籍番号/ ID No: C0TD9119

氏 名 /Name: Muhammad Hannan AHMED

TOHOKU UNIVERSITY

Graduate School of Engineering

Synergy-Based Transferable Control Strategies for Natural Elbow Motion Generation in Transhumeral Prosthesis

(上腕義手における自然な肘動作生成のためのシナジーに基づく
転用可能な制御戦略)

A dissertation submitted for the degree of

Doctor of Philosophy (Engineering)

Department of Robotics

by

Muhammad Hannan AHMED
(ID No. C0TD9119)

January 8, 2023

Synergy-Based Transferable Control Strategies for Natural Elbow Motion Generation in Transhumeral Prosthesis

Muhammad Hannan Ahmed

Abstract

The field of prosthetics has witnessed remarkable progress in recent years. Advances in robotics and sensor technologies have ushered in the era of bionic limbs, exemplified by the modular prosthetic limb. These prosthetics not only mimic lifelike appearances but also feature numerous degrees of freedom (DOF), enabling them to replicate nearly all human arm and hand movements effectively. This represents a significant advancement for individuals with above-elbow or more severe upper limb amputations. However, the challenge persists in effectively controlling the multiple joints of a prosthetic arm, as the full potential of these functions cannot be realized unless users can control the device easily, quickly, and reliably. This discrepancy results in a growing gap between control methods and hardware improvements.

The lack of controllability is particularly pronounced in the case of transhumeral amputees, who experience the loss of all forearm and wrist muscles. Furthermore, they encounter the intricate challenge of managing the additional DOF associated with the elbow joint. This is crucial for accurately positioning the hand and orienting it to grasp objects, as well as coordinating the movements of various arm joints during reaching activities. Compounded by the constraint of providing electromyography (EMG) signals solely from the upper arm, transhumeral amputees face hurdles in utilizing the myoelectric control approach for a multi-functional prosthesis. While targeted muscle reinnervation (TMR) offers a potential solution by transferring residual arm nerves controlling missing distal muscles and joints to compartments of remaining muscles, this introduces complexities. The resulting control becomes slow, sequential, and counter-intuitive, primarily due to the unavailability of physiologically appropriate muscles in the process.

Advanced practices such as osseointegration, brain-computer interface (BCI), and neuromusculoskeletal implants have emerged to enhance the controllability that transhumeral amputees can exert over their prosthetic devices. These innovative approaches integrate surgical reconstruction procedures with implanted electrodes and a long-term stable neuromusculoskeletal interface to attach the prosthetic arm to the body directly. These techniques hold the potential to offer superior control and intuitive sensory feedback through direct nerve stimulation. However, the clinical implementation of these efforts faces challenges due to the absence of a safe and long-term stable bidirectional interface between implanted electrodes and external prosthetic limbs. Besides requiring highly invasive and specialized surgeries, optimizing these strategies necessitates advanced signal processing techniques, along with

the development of decoding and classification algorithms for sensorimotor signals. The recruitment of willing subjects and extensive training requirements present yet another limitation.

This thesis presents three contributions centered on the prediction of elbow joint motion during arm-reaching movements for transhumeral prosthesis control, with the goal of bridging the gap between control methods and hardware advancements. Our approach involved using residual shoulder motion-based, non-invasive, intuitive, and easily acquired joint angular data signals as control input and training data for our predictive models. We harnessed the predictive capabilities of artificial neural networks (ANNs) to automate elbow joint motion during target-reaching tasks.

In the initial study of this thesis, the aim was to enhance the control of transhumeral prostheses by concentrating on a synergistic approach for the simultaneous control of two DOFs of the elbow joint, with a focus on transferability across multiple users. For transhumeral amputees, a highly accurate and transferable predictive model is imperative, as individual calibration or personalized learning methods prove ineffective due to the inability to provide the necessary data. We introduced synergy-space neural networks as a transferable model for predicting elbow joint motion based on residual shoulder motion. Synergies, observed to be repeatable and shared across subjects in similar tasks, were systematically analyzed for inter-joint coordination during reaching movements. We then explicitly incorporated only the most significant synergy components in the learning process, facilitating more precise and efficient training of the ANN and leveraging the shared nature of these synergies to enhance model transferability. The implementation and evaluation of this method were presented, including discussions on its learnability and robustness for transferability to amputee users. The study involved 14 able-bodied subjects, focusing on arm-reaching movements in the horizontal plane. We tested 36 training strategies for each of the 14 subjects, comparing the synergy-space and conventional neural network learning approaches. The results were evaluated using Pearson's correlation method, root mean square error ($RMSE$), and the analysis of variance ($ANOVA$) test. The offline cross-subject analysis indicated that the synergy-space neural network exhibited approximately 40% less variation in the RMSE, demonstrating its superior robustness to inter-individual variability. This finding holds promise for the development of a synergistic and generalized control strategy applicable to transhumeral prostheses and other rehabilitation applications.

As the second contribution of this thesis, we introduced an innovative motion-cloning strategy using deep reinforcement learning (DRL). Given that the first part of this thesis relied on ANNs to identify and model the synergistic coordination between the shoulder and elbow joints, a critical challenge is associated with obtaining sufficient human motion data collected from different subjects across various activities of daily living (ADL) and conditions. For instance, changes in target height can alter reaching motion, but conducting human experiments for all conditions is impractical. Leveraging the demonstrated ability of DRL algorithms to generate human-like synergistic motion in humanoid agents for redundancy handling and movement optimization, we introduced a DRL-based motion cloning framework utilizing a 7-DOF robot arm model in a mujoco simulation to generate synthetic motion data. This study unveiled the potential of synthetically generated motion

data using a DRL-based simulation to accurately replicate human-like synergistic arm movements and its effectiveness in training predictive models capable of accurately predicting actual human arm movements. We explored various configurations of training motion data, including synthetic, real, and hybrid datasets, to train different ANNs and evaluated their performance by comparing predicted elbow joint motion with real motion data recorded from human subjects during reaching movements. Through our analysis, we confirmed that synthetic motion data closely resembles the characteristics of motion data obtained from human subjects and effectively captures the synergistic patterns of arm-reaching movements, enabling the training of an accurate predictive model. Our evaluations affirm the ability of the ANN trained using synthetic motion data to predict natural elbow motion across multiple subjects accurately. Moreover, motion data augmentation using synthetic motion data can not only supplement limited data availability but also diversify the training data, contributing to improved generalization. These findings have significant implications for creating comprehensive synthetic motion dataset resources for diverse arm movements and advancing strategies for automated prosthetic elbow motion.

In the final phase of this thesis, we introduced a framework for the real-time prediction and evaluation of elbow joint motion during extensive arm-reaching activities. Given the challenges associated with clinical trials on amputee subjects, we developed a virtual reality (VR)-based platform that enables subjects to interact with a 3D workspace and perform reaching tasks with the full range of arm motion. Subjects can conveniently wear sensors on their body using adjustable straps to actively engage with the virtual workspace, controlling the movements of a humanoid actor to perform arm-reaching tasks without the need for any special preparations. Our experiments and validation were conducted in the virtual workspace, initially employed for data acquisition from healthy human subjects and later to verify the efficacy of the trained ANN predictive models. Arm-reaching motion data from six healthy subjects were used to train ANN models, and their performance was initially assessed offline across all subjects to test motion prediction accuracy and robustness to inter-individual variability. In the conclusive phase, we validated the performance of the predictive models on an amputee participant, a right-arm transhumeral amputee, who successfully executed reaching movements in the virtual workspace. Simultaneously, the ANN model predicted the motion of his amputated elbow in real-time. Despite the participant's lack of prior experience with the task or familiarity with the apparatus, our synergy-spaced approach-based ANN predictive model enabled the successful execution of reaching movements toward all target points in the virtual workspace. This successful validation of an amputee subject performing reaching movements toward target points in a virtual workspace demonstrates the potential efficacy of our approach. These findings have significant implications for creating comprehensive virtual workspaces with diverse arm movements, covering various activities for validating and advancing strategies in transhumeral prosthesis control.

Dedication

In loving memory of my dear father...

To my beloved parents and cherished siblings. Thank you for your unwavering love, guidance, and support at every step of my journey. With gratitude for the countless moments of encouragement and the freedom to follow my heart, I am forever grateful.

Inna Lillahi wa Inna Ilayhi Raji'un. [2:156]
Indeed we belong to Allah, and verily to HIM we shall return. [2:156]

Contents

List of Figures

List of Tables

Chapter 1

Introduction

As you begin reading, try raising your hand and performing the most unusual gesture you can imagine. Observe how this simple act requires little effort. Much like this, we seamlessly execute intricate arm movements in our daily lives, often without conscious consideration.

For instance, when you are slicing a delicate piece of cake, you effortlessly adjust the pressure of your grip on the knife handle. Similarly, when you find a key about to slip from your grasp just before unlocking a door, you instinctively respond by tightening your hold. Remarkably, these actions happen without the need for a conscious thought process such as, 'The key is slipping; I must tighten my grip,' or 'I need to adjust my knife grip for precise slicing.' This illustrates the intricacy of the human arm, which possesses a multitude of degrees of freedom, presenting a fascinating challenge for control. It is a powerful tool for both perceiving and interacting with the environment, embodying a high level of sophistication in facilitating physical as well as social interactions.

"Amputation" is a medical term that describes the surgical removal of all or a portion of a limb or extremity, resulting in the absence of that limb. Such procedures can be necessitated by trauma or diseases. However, it's important to recognize that not all instances of limb absence stem from acquired conditions; some individuals are born with congenital absence or variations. Consequently, we can collectively refer to this diverse population as individuals with limb absence (LA), encompassing both those who have undergone amputations and those born with limb differences.

Approximately 2 million Americans, constituting 1 in 200 people, are living with LA, with an additional 28,000,000 individuals at risk of amputation. The USA witnesses around 185,000 amputations annually, and this figure is projected to more than double by 2050 [1]. Among those with LA, roughly 3% are affected by upper extremity amputations. Recent data highlights that trauma-induced upper limb loss occurs at a rate of 3.8 cases per 100,000 people. When examining trauma-related upper limb amputations, the loss of digits, especially a single finger, is the most prevalent (2.8 cases per 100,000). Beyond this, the distribution of upper limb amputations follows with trans-radial (47%) and trans-humeral levels (25%) being

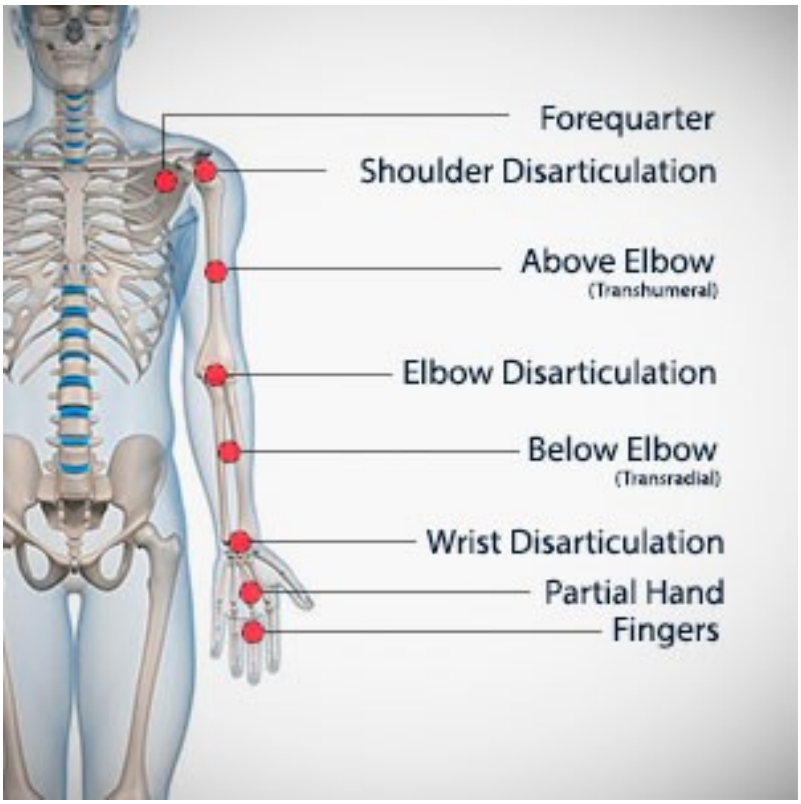

Figure 1.1: Levels of upper limb amputations [3].

the next most frequent, while elbow disarticulations are the least common (2.1%) [2].

The foremost cause of upper limb amputations, accounting for approximately 80% of cases, is trauma, with factors like traffic accidents being predominant, followed by complications stemming from diseases such as cancer, tumors, and diabetes [4]. The classification of upper extremity amputations encompasses a range of levels, including forequarter, shoulder disarticulation, transhumeral, elbow disarticulation, transradial, wrist disarticulation, and transcarpal, illustrated in Figure 1.1. In broad terms, these can be categorized into two groups: (1) *Below-Elbow*, also known as *Transradial amputation*, affecting the region between the elbow and wrist, and (2) *Above-Elbow*, also referred to as *Transhumeral amputation*, involving the area between the shoulder and elbow. Regardless of the specific level, the absence of an upper limb can be profoundly impactful on both the individual and their family due to its effects on social and physical functioning [5].

Upper limb amputations at any level significantly impede the performance of the activities of daily living (ADLs), whether at home, work, or in social settings, with proficiency decreasing as the level of amputation rises. Specialized care is essential to address the multifaceted challenges presented by the population with upper limb Absence (ULA). A *prosthesis* is a device designed to replace a missing body part or limb, aiming to assist users in performing daily tasks and ultimately enhancing their overall quality of life.

1.1 Background

The journey of prosthetic users is defined by the possibilities and constraints of a device designed to facilitate their ADLs. In particular, perceiving a bionic hand as a functional and naturally integrated limb is fundamental to encouraging the consistent use of the device and reducing the risk of abandonment. Research has delved into understanding the needs of upper limb prosthesis users [4][6][7], seeking to establish guidelines and enhance current prosthetic solutions based on user satisfaction and their desired ADLs. Broadly, user requirements can be distilled into intuitive control, user-friendliness, and sensory feedback. Additionally, investigations have explored users' proficiency in controlling prosthetic devices [8] and the development of user-driven prosthetic arm designs [9] tailored to excel in specific workplace scenarios.

We have witnessed significant advancements in upper limb prosthetic technology, evolving from the early use of hooks to body-powered mechanical systems and now to the present era of bio-inspired robotic systems. Remarkable progress has been made, particularly for below-elbow amputees, with a wide array of advanced prosthetic solutions available in the market. These range from simple yet robust open-close gripper designs to sophisticated bionic hands equipped with individually activated joints for each finger [10], offering precise control to accomplish a multitude of tasks.

Individuals with higher levels of amputation, such as transhumeral amputees, face a unique challenge in finding prosthetic solutions that can provide them with a multi-functional upper limb. Thanks to the strides made in robotics and sensor technologies, we are now capable of developing sophisticated, state-of-the-art upper extremity prostheses such as the DEKA arm [11] and the Modular Prosthetic Limb (MPL) [12][13]. Notably, these prostheses not only exhibit a lifelike appearance (see figure 1.2) but also boast numerous degrees of freedom (DOF). This extensive range of motion empowers these devices to replicate nearly all human arm and hand movements effectively, marking a potential breakthrough for individuals with above-elbow or more severe upper limb amputations.

But the problem is that "*Function*" does not equal "*Functionality*". It is essential to understand that having an abundance of functions does not necessarily translate to enhanced functionality. Even the most intricate prosthetic devices, equipped with numerous functions, might not offer practical benefits to users if they cannot access and utilize these functions swiftly, effortlessly, and consistently. This gap between prosthetic hardware's capabilities and control methods has been widening over the years, posing a significant challenge for advancements in prosthetic technology.

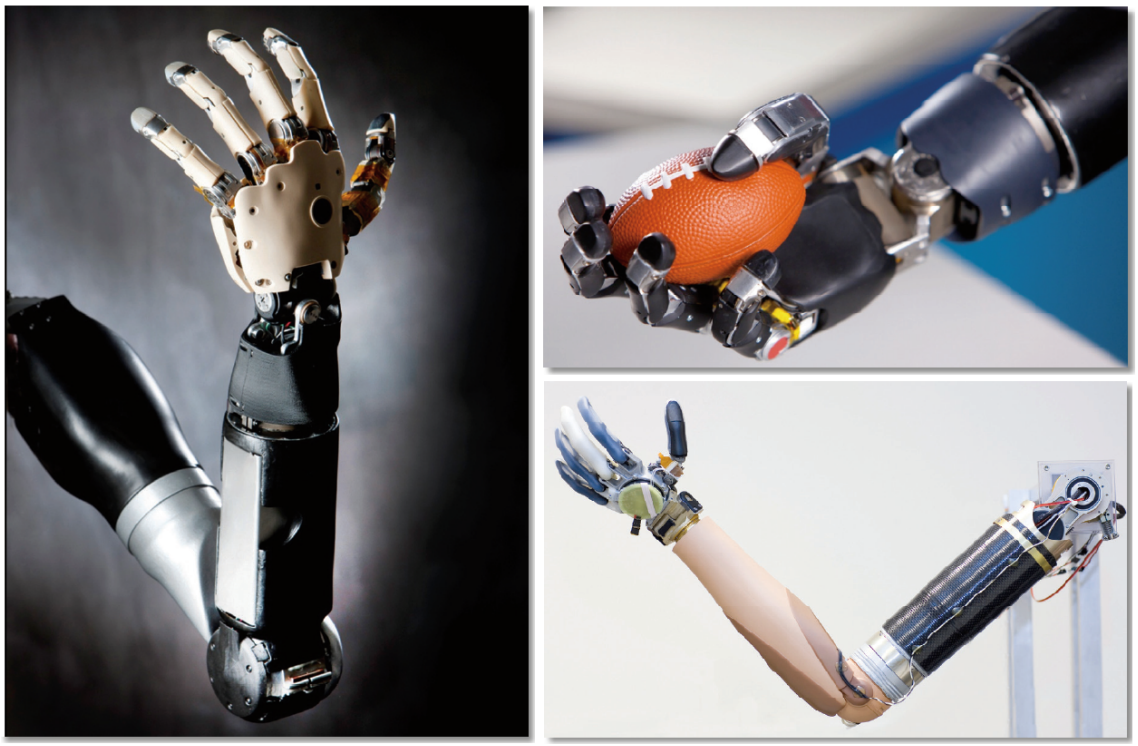

Figure 1.2: The Modular Prosthetic Limb, human like robotic arm having numerous sensors in the upper arm and hand with 26 DOF and 17 DOC [13].

The current challenge lies in bridging the gap between prosthetic devices and their users. This limitation in control strategies arises from the discrepancy between the number of control signals an amputee can provide and the available functions in the prosthesis. Degrees of Freedom (DOF) represent the number of independently operable functions within a system, while Degrees of Control (DOC) indicate the number of functions controllable by the user. For instance, consider the Modular Prosthetic Limb (MPL) with 26 DOF but only 17 DOC. This means that while the MPL offers 26 distinct joint movements, the user can execute these through just 17 distinct control commands.

In the realm of Myoelectric control, a widely used Electromyography (EMG)-based approach for prosthetic arms [14], the number of input signals the user provides is consistently fewer than the DOC. Even the commercially available prosthetic elbows, such as the Dynamic Arm [15] and the ErgoArm [16], are also controlled via myoelectric signals. This challenge is even more pronounced for transhumeral amputees, yielding complex control schemes when they have to control an entire prosthetic limb. They can only provide EMG signals from their upper arms to manage a prosthesis with multiple active degrees of freedom, including a powered elbow, wrist, and hand.

Advanced signal processing techniques like pattern recognition for EMG signals have been developed to address these issues. These techniques can identify activation patterns to classify a greater number of distinct commands based on differences in muscular activities associated with the same myoelectric control inputs [14][17]. Surgical innovations, such as Targeted Muscle Reinnervation (TMR), have also been

employed to enhance users' control capabilities over a prosthesis. TMR involves relocating residual nerves that have lost their function due to amputation to reinnervate new target muscle sites [14]. While pattern recognition and TMR control schemes provide transhumeral amputees with improved control over multi-functional prosthetic limbs, they often result in slow, sequential, and unnatural control because the physiologically appropriate muscles are not available. These counter-intuitive control strategies and limited functionality cause the development of compensatory strategies and the high rejection rate of these devices [18][19].

For many transhumeral amputees, the challenge of effectively controlling an active elbow prosthesis is compounded by the need to coordinate reaching tasks, adding an extra layer of complexity to control schemes. So far, finding an intuitive and functional control strategy for managing multi-joint prostheses in transhumeral amputees remains a significant hurdle. Beyond the issue of available residual muscles, myoelectric control faces constraints stemming from factors like skin impedance, electrode placement, and muscle fatigue. These factors collectively impact the quality of EMG signals used as control inputs. Thus, relying solely on myoelectric control strategies seems insufficient. Numerous investigations have explored alternative approaches, including those based on myokinetic signals [20] utilizing residual kinetic activity of the limb, ultrasound signals [21], and mechanomyography [22], which leverages muscle contraction-induced vibrations as control signals. Drawing insights from the study of the Central Nervous System (CNS) and human motor control abilities, bio-inspired approaches have also been employed to develop more natural and intuitive control strategies [23].

When it comes to tasks like target reaching or controlling the prosthetic elbow joint motion for transhumeral amputees, the ultimate goal is for the prosthetic device to seamlessly integrate with the human body. The residual limb motion strategy [24][25] is a promising approach to achieving automatic control of the prosthetic elbow joint by leveraging the natural coordination between joints. Studies on Joint Coordination approaches have provided evidence of recurring patterns in joint kinematics during grasping or reaching tasks in upper limb movements. For instance, correlations have been found between elbow flexion and humeral inclination during reaching [26] and between hand azimuth and movement direction during grasping [27]. Additionally, research has indicated that coordination in joint kinematics can vary depending on the task [28][29], suggesting the need to tailor the upper limb control scheme for different tasks, such as reaching tasks in horizontal and vertical planes. It's worth noting that the relationship between human upper limb kinematics is inherently nonlinear, and there has been promising progress in modeling this relationship using various Artificial Neural Network (ANN) architectures [30][31][32].

In this thesis, our aim has been to investigate strategies that enhance the intuitive control of prosthetic elbows for transhumeral prosthesis users. Our approach centers around refining the estimation of elbow joint motion through the utilization of residual shoulder motion, thereby enabling automatic control of the prosthetic elbow. The initial study within this thesis delves into the application of synergy-space neural networks as a promising motion estimation technique for replicating natural elbow motion. It addresses the challenge of effectively transferring the predictive model to amputee users. To accomplish this, we have developed a more robust model

that incorporates Kinematic Synergies and Recurrent Neural Networks (RNNs) to advance towards a more natural and intuitive control scheme.

In the second study of this thesis, we explored synthetic motion generation to enhance the predictive models' performance. We leveraged the powerful learning capabilities of the deep reinforcement learning (DRL) algorithm to replicate human arm reaching motions. Our approach addresses the need for extensive human motion data, encompassing various subjects and activities of daily living (ADL) tasks, to train these predictive models effectively. To achieve this, we employ synthetic motion data, which enriches and diversifies the training dataset used for refining the predictive model when combined with real motion data obtained from human subjects.

Finally, in the third study of this thesis, we crafted a predictive model tailored for the real-time estimation of prosthetic elbow joint motion during far-reaching movements of the arm within a simulated 3D environment.

This section introduces the background of several concepts used in this thesis, including the motor synergy concept and its calculation, and the residual limb motion strategy. The knowledge of ANNs and DRL necessary to understand this thesis is also explained in this section.

1.1.1 Motor Synergies

Human beings possess a remarkable ability to orchestrate intricate and efficient movements, leveraging the dynamics of their complex musculoskeletal system. The challenge of controlling and constantly fine-tuning numerous degrees of freedom (DOF) within this system poses a significant computational hurdle. To navigate the inherent redundancy in the musculoskeletal structure and generate voluntary movements, the central nervous system (CNS) must synchronize the activation of numerous muscles, each comprised of thousands of motor units. This begs the question: How does the CNS manage the intricacies of this intricate, nonlinear relationship between adjustments in DOF settings and their resulting effects?

Neuroscience research has firmly established the concept of motor synergies within the central nervous system (CNS) [33][34][35]. This concept streamlines control by amalgamating multiple degrees of freedom (DOF), significantly alleviating the CNS's computational burden. This concept has several interpretations, but the most common one involves the CNS employing a considerably smaller set of variables to govern a large group of muscles. As a result of the co-activation of these muscles, which employs fewer neural commands, referred to as motor synergies, the electromyography (EMG) activities of these muscles tend to be both spatially and temporally correlated, known as Muscle Synergies. Simultaneously, this coordinated muscle activation fosters a degree of synchronization among closely related joints, resulting in coupled angular movements in various joints, referred to as Kinematic Synergies [36].

Recent findings by d'Avella [37] suggest that the CNS approaches movement generation and control in a task-dependent manner, signifying that synergies act as a bridge between task-level objectives (e.g., reaching and grasping an object) and execution-level commands (e.g., muscle identification and activation) necessary to achieve those objectives. Consequently, to address redundancy, the CNS identifies and manipulates the task-relevant degrees of freedom while considering all task constraints. This surplus of DOF enables the CNS to flexibly utilize degrees of freedom that align with the task's requirements [38], resulting in sophisticated and synergistic motion generation. This may elucidate how humans can naturally execute complex, energy-efficient movements with minimal conscious effort.

The concept of synergies has played a pivotal role in explaining a wide spectrum of motor behaviors, as evidenced by numerous investigations. For instance, a study in [39] meticulously analyzed locomotor step cycles in neonates, toddlers, preschoolers, and adults to elucidate the progression from rudimentary to sophisticated movements during development. Their findings showcased the ability to replicate EMG profiles by amalgamating two to four fundamental patterns (i.e., muscle synergies) encompassing the activity of twelve muscles, reflecting bilateral muscle activation. Notably, two of these fundamental patterns were consistently identified across all subjects, indicating that these locomotor primitives persist throughout development. This suggests a degree of shared synergies among individuals performing similar tasks, potentially valuable in developing a generalized control model for prostheses using data from able-bodied subjects.

Intriguingly, the authors in [40] took a unique approach by documenting the emergence of motor synergies in simulated multi-joint robotic agents. In a simulated environment, these agents underwent training to learn running skills via deep reinforcement learning algorithms and were assessed based on performance-energy indices. The joint-space synergy analysis of the trained agents revealed the development of motor synergies, even though synergy constraints were never explicitly incorporated into the reward function. These results underscore the inherent energy efficiency associated with synergistic movements.

Synergies during Human Arm Movements

Daily activities, such as reaching for objects within our immediate surroundings, demand a precise orchestration of limb movements. This process of controlling directional limb movements involves a series of intricate operations, specifically sensorimotor transformations, essentially translating the visual information of the target's location on the retina into activation patterns for the relevant muscles that guide the limb toward the target. However, not all of the arm's mechanical degrees of freedom (DOF) are fully engaged during actual movements, like reaching for and grasping an object. This underutilization is due to the inter-joint coupling effect caused by the correlated electromyography (EMG) activities of different arm muscles, commonly referred to as muscle synergies.

Figure 1.3: The experimental setup, as illustrated in [44], encompassing five distinct sectors (frontal, right, left, horizontal, and up) for upper limb reaching tasks.

In terms of kinematics, redundancy emerges in human arm-reaching movements because, for any given hand position, there exists an infinite array of possible arm postures. Likewise, numerous sets of muscle activation patterns can sustain each of these arm postures, introducing redundancy at the muscular level. Consequently, determining the optimal arm posture for a desired hand position exemplifies a redundancy challenge routinely navigated by the central nervous system (CNS). The CNS often accomplishes this by generating reproducible behaviors, underpinning the concept of synergies [41]. This underscores the goal-oriented approach of the CNS, favoring the coupling of DOFs rather than their independent control, ultimately yielding more natural and energetically efficient motion.

Extensive research efforts have delved into the examination of muscle and kinematic synergies within the human arm during a wide spectrum of movements [37][42] [43]. A particularly comprehensive analysis was conducted by d'Avella in [44], where they systematically characterized the muscle synergies involved in healthy arm movements across various upper limb reaching tasks encompassing sectors such as the horizontal plane, upward motions, frontal movements, and both left and right directions within the peripersonal workspace, as depicted in Figure 1.3. Even amid these highly diverse upper limb movements, it was remarkable that the original electromyography (EMG) envelopes could be effectively reconstructed using a reduced set of muscle synergies. Notably, these synergies exhibited a level of repeatability and were shared, to some extent, among sectors and across different subjects.

In their study [41], the authors conducted an analysis of kinematic synergies observed in various arm postures during unrestricted, natural human arm movements. This investigation involved the calculation of inter-joint coupling, examining both untrained and rapid catching movements. In these catching exercises, participants were instructed to intercept a ball thrown toward them along sixteen different trajectories. Remarkably, the findings revealed that only three synergies were necessary to effectively capture 90% of the variance in the recorded data, despite accounting for ten joint angles, including 7 degrees of freedom (DOF) of the arm and 3 of the shoulder girdle. A similar outcome was also observed in [45], where joint angular velocities during reaching motions were analyzed.

These results provide compelling evidence that a reduced number of kinematic synergies, although potentially sacrificing some precision, can aptly represent and reconstruct the natural reaching movements of the human arm.

Extracting Synergies

Over the past few decades, extensive research has uncovered motor primitives, commonly referred to as synergies, at multiple levels, including electromyographic, kinetic, and kinematic domains. Typically, the identification of these components has relied on unsupervised learning algorithms such as independent component analysis (ICA), principal component analysis (PCA), and non-negative matrix factorization (NMF), among others. The formalization of synergy extraction methods has been presented in works by various authors [46][47][48]. The fundamental process for extracting synergies can be distilled into the following key steps:

- Data Acquisition and Preprocessing:
  Collect and preprocess data during the execution of complex behaviors. This data can encompass various types, such as EMG activity or joint angles, depending on whether muscle or kinematic synergies are being investigated.
- Computational Analysis:
  Utilize computational techniques like PCA or NMF to discern the set of synergies inherent in the recorded data.
- Evaluation:
  Assess whether combinations of these synergies effectively capture and replicate the observed data.

Our study employed spatial synergies derived from angular movement data of the arm's joints. The concept of inter-joint coordination during human arm reaching movements suggests that a set of degrees of freedom (DOF) may exhibit simultaneous covariations. These movement primitives are known as Spatial Synergies, assuming that the ratios of signals characterizing different DOFs remain constant over time [46]. The spatial synergy decomposition is represented as equation 1.1.1, where $x^l(t)$ denotes the source signals of individual DOF at time point t in trial number l, and N signifies the total number of spatial synergy components. The variables w_n represent the spatial patterns of the kinematic synergies, assumed to remain consistent across trials, while $c_n^l(t)$ represents the corresponding activation signals that vary for each trial.

$$x^l(t) = \sum_{n=1}^{N} w_n \cdot c_n^l(t) + residuals \tag{1.1.1}$$

We can represent equation 1.1.1 in a simplified matrix form as 1.1.2 by excluding the *residuals* term. In this representation, X represents the source signals, W defines the synergy components, and C constitutes the corresponding activation signals matrix.

$$X = W \cdot C \tag{1.1.2}$$

For our computational analysis, we employed Principal Component Analysis (PCA), one of the most extensively utilized algorithms for solving equation 1.1.2. The central concept behind PCA is to minimize the reconstruction error E, as defined in equation 1.1.3, concerning W and C, with $\|\cdot\|_F$ representing the Frobenius Norm. All computations were carried out in Python using the "*scikit-learn*" library.

$$E^2 = \|X - W \cdot C\|_F^2 \tag{1.1.3}$$

1.1.2 Residual Limb Motion Strategy

A promising control scheme for transhumeral prostheses is rooted in the residual limb motion strategy. This approach capitalizes on the natural relationships between joints in the human arm to automatically control the prosthetic elbow joint [49]. Upper limb prostheses for transhumeral amputees are designed with numerous DOFs to mimic the mobility of a human arm. Consequently, these prostheses can execute a wide range of movements through a myriad of joint configurations, similar to a healthy limb. However, the challenge lies in selecting the most natural kinematic solution.

Research into healthy arm movements has revealed that natural motions are task-centered. Instead of individually controlling each joint or muscle, the emphasis is placed on the object or hand's motion [27]. Furthermore, Studies have also indicated evidence of coordinated joint movements, particularly the coupling of the shoulder and elbow joints in the upper limb [50]. Thus, coupling joint motions in a transhumeral prosthesis to replicate a human-like control strategy holds promise. The concept was initially introduced in [51], where a mechanical system was developed to link wrist rotation and elbow flexion to residual limb motion. This demonstration illustrated that the residual limb mobility of a transhumeral amputee could be harnessed to automatically operate the elbow joint.

Establishing the coordination relationship between joints, like predicting elbow motion based on shoulder kinematics, opens the door to more intuitive control strategies. The function governing elbow motion in relation to shoulder kinematics is inherently nonlinear, and various regression tools have been explored to approximate it. Among these tools, artificial neural networks (ANNs) have consistently shown their prowess in achieving superior prediction results [30], [52]. However, it's important to note that ANNs demand a diverse and substantial amount of motion data for effective model training.

In many studies, camera-based motion capture systems have been employed to collect training data. However, this approach has limitations in the context of prosthetic users, as it is often impractical to use such systems outside a controlled laboratory environment. Previously, goniometers were used for kinematic data recording [31][32].

Fortunately, the advent of inertial measurement units (IMUs), highly accurate embedded motion sensors, has opened up new possibilities. These IMUs allow for the implementation of upper limb coordination-based automatic prosthesis control strategies without being bound by specific working environments.

1.1.3 Artificial Neural Network (ANN)

Various studies have explored the application of different artificial neural network (ANN) architectures for deciphering inter-joint coordination during human arm movements. In one instance, the authors in [53] utilized a radial basis function network (RBFN)-based neural network, while [54] employed a time-delayed adaptive neural network (TDANN) to estimate distal joint angles. ANNs are computational models inspired by the workings of biological neural networks, allowing them to "*learn*" how to perform tasks or model relationships between variables solely through examples, without the need for explicit task-specific programming.

A prominent neural network model is the feedforward neural network, which propagates signals in a unidirectional manner, moving from the input layer through the hidden layers to the output layer. Each layer comprises interconnected units or nodes known as "*Neurons*" or "*Perceptrons*." These neurons receive inputs, compute their internal states, and pass information to the next layer until the final desired output is computed.

The information flow from neurons in layer $l-1$ to the k^{th} neuron in the subsequent layer l can be mathematically expressed as in equation (1.1.4). Here, w^l_{kj} represents the weight associated with neuron j in layer $l-1$ for the incoming k^{th} node in layer l, and b^{l-1}_k is the bias for the k^{th} neuron in layer $l-1$. The variable n denotes the total number of nodes in layer $l-1$, and σ represents the activation function. Activation functions, such as Step, Sigmoid, or tanh, define the output of a node based on the given input values.

$$a^l_k = \sigma(w^l_{k1}a^{l-1}_1 + w^l_{k2}a^{l-1}_2 + \cdots + w^l_{kn}a^{l-1}_n + b^{l-1}_k) \tag{1.1.4}$$

Building on this concept, the computational process of a neural network for generating output in response to a given task can be summarized as follows:

(i) Calculate the weights w for the information received from the previous layer and add the bias b.

(ii) Apply the activation function σ to the result from step (i) and transmit the output value to the next layer.

(iii) Iterate through steps (i) and (ii) until reaching the final output layer.

The above process is commonly referred to as the "*learning*" or "*training*" of the neural network. During this phase, the neural network automatically determines the weights and bias parameters necessary for calculating the output. ANNs rely on a critical component known as the "*loss function*" to achieve the best output results. This function assesses how accurately the neural network models the provided data. There are several types of loss functions, including mean squared error (MSE), mean absolute error (MAE), and root mean squared error (RMSE), among others, used for this purpose.

If the predicted values significantly differ from the actual results, the loss function outputs a high error value. The neural network seeks to optimize the weight and bias parameters throughout the learning process to minimize this loss and provide the most accurate results. This optimization is carried out by various algorithms and methods that modify parameters like weights, bias, and learning rate. One commonly used optimization method is gradient descent. It computes the gradient of the parameters, indicating the direction in which the loss function decreases the most, and adjusts the parameters accordingly (either increasing or decreasing their values).

Equations (1.1.5) and (1.1.6) illustrate the updating rules for weights w and bias b, where η represents the learning rate, and L is the loss function. Since data is typically randomly selected from the training dataset in mini-batches, stochastic gradient descent (SGD) is often preferred. Recent developments have introduced other optimization methods, such as Momentum, Adagrad (an adaptive gradient method), and Adam, to enhance the training process further.

$$w = w - \eta \frac{\partial L}{\partial w} \tag{1.1.5}$$

$$b = b - \eta \frac{\partial L}{\partial b} \tag{1.1.6}$$

The purpose of loss functions and optimization algorithms is to train neural networks efficiently. However, they can sometimes lead to a common problem known as "*overfitting*." Overfitting occurs when the loss function for the training dataset reaches a very low value, but the neural network performs poorly when presented with new, real-world input data. Essentially, the neural network has memorized the training examples instead of learning to generalize to novel situations, which is the primary objective of neural network training. To combat overfitting, various techniques such as "*weight decay*" and "*dropout*" are employed. Dropout, for instance, enhances generalization by randomly deactivating nodes, or neurons, along with their connections in the neural network layers during the learning process.

Recurrent Neural Network (RNN)

The feedforward neural network featured a straightforward configuration where neurons in each layer were weighted, and the resulting sums were passed on to the next layer. During this forward propagation, no consideration was given to the order of input data, rendering it unsuitable for processing time-series data. In contrast, the recurrent neural network (RNN) is specifically designed to handle sequential or time-series data. The information flow in an RNN still follows a unidirectional path, similar to a feedforward neural network. However, the key distinction lies in the consistent structure of each layer within the RNN (as depicted in Figure 1.4).

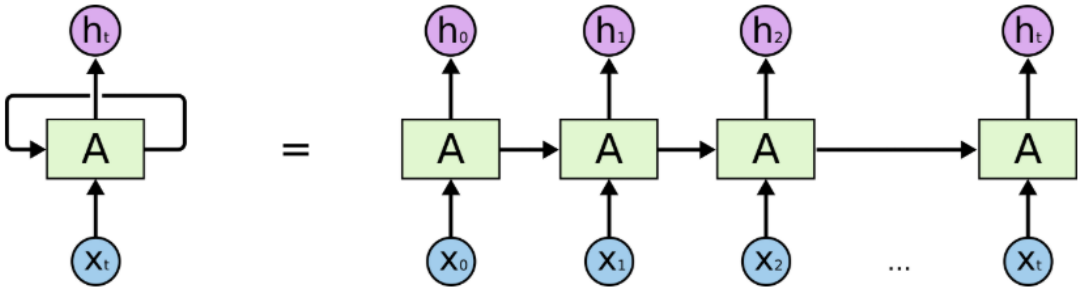

Figure 1.4: An unrolled simple recurrent neural network [55].

RNN excels in processing data that evolves over time, as it has the ability to memorize past information and leverage it for accurate predictions. Equation (1.1.7) represents the general computation for the output in an RNN, where h_t denotes the output at a specific time t, computed based on the input x_t and the previous output h_{t-1}, which encapsulates past information. In this context, h is referred to as the hidden state, as it retains information from previous states within the hidden layers.

$$h_t = \tanh\left(h_{t-1}W_h + x_tW_x + b\right) \tag{1.1.7}$$

However, there's a downside to simple RNNs known as the "*vanishing gradient problem.*' This issue emerges as time-series data gets longer. When we're using backpropagation, a common method for adjusting the network during training, the gradient (which guides how much we update the network's weights) gets multiplied by the weight matrix each time it flows through an RNN layer.

This multiplication causes the gradient to shrink exponentially. Consequently, the initial layers in the network don't get updated effectively during each training session (refer to figure 1.5).

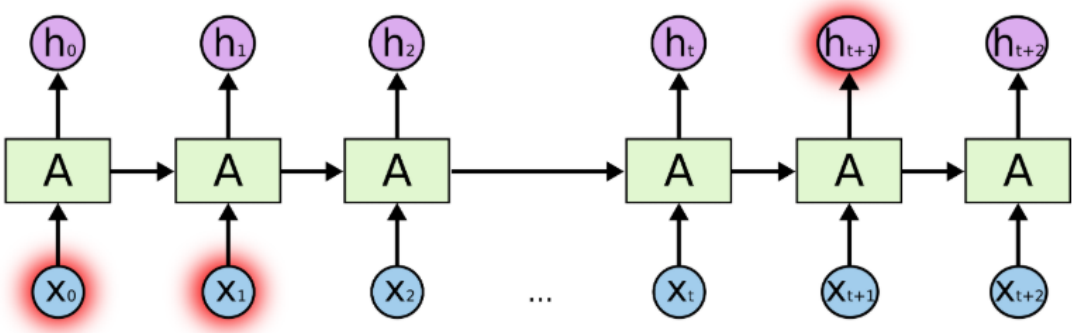

Figure 1.5: Vanishing gradient problem in recurrent neural network [55].

Long Short-Term Memory (LSTM)

Long Short-Term Memory (LSTM) neural networks, a unique type of RNN, excel at handling long-term dependencies. LSTMs incorporate internal mechanisms known as "*gates*" (refer to figure 1.6) that effectively manage information flow, thereby mitigating the vanishing gradient problem. Another crucial distinction is the presence of a "*cell state*" (C) within LSTMs, which hold essential information from the past to the present. This cell state is carried throughout the entire chain of LSTM layers, and gates are the exclusive means of updating or adding vital information to it.

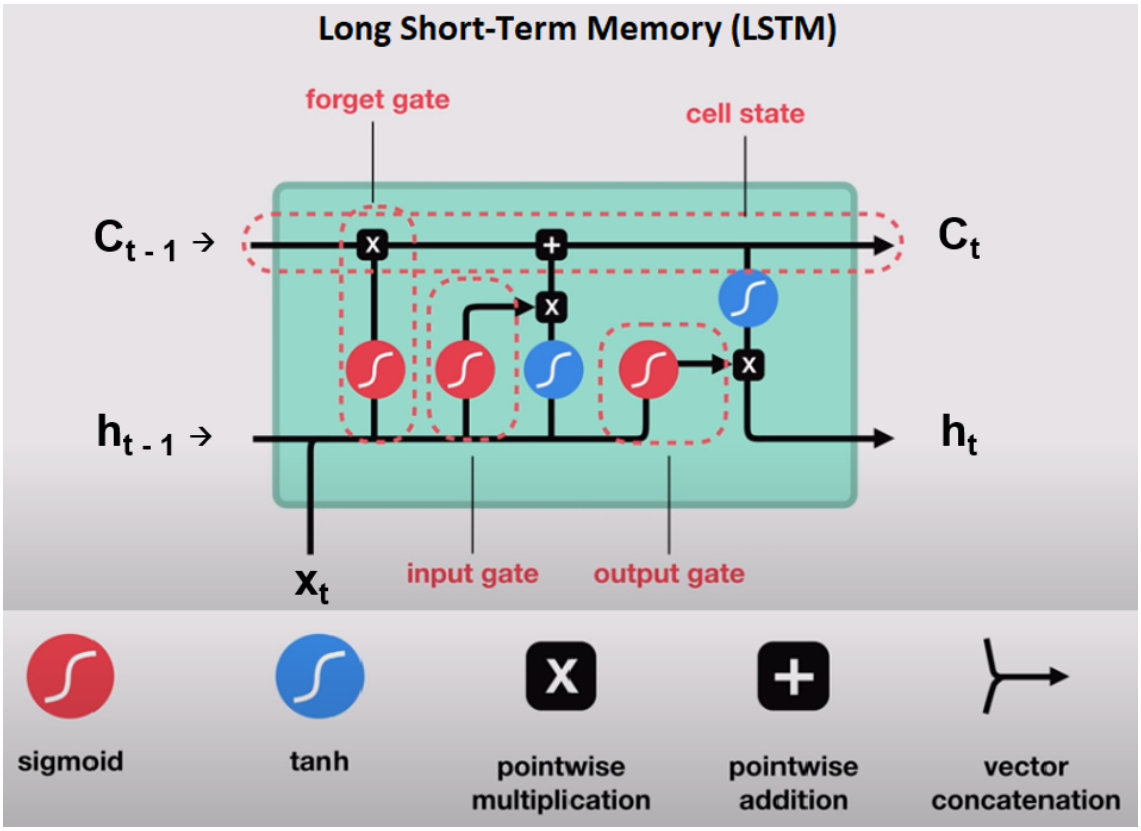

Figure 1.6: The repeating module in an LSTM with the "*gates*" mechanism [56].

The computation begins with a crucial decision: what information should be retained in the cell state and what should be discarded. To accomplish this, the "*forget gate*" comes into play, employing a sigmoid function that evaluates both the current input and the output from the previous layer h_{t-1}. This operation yields an output value between 0 and 1. The result is then multiplied by the existing previous cell state C_{t-1}. A multiplication of 1 signifies the retention of all past information, while a multiplication of 0 effectively erases everything irrelevant.

Next, we determine what information should be updated in the cell state. This involves combining the output from the "*input gate*" with the tanh function layer, which is also calculated based on the current input x_t and the previous output h_{t-1}. The new cell state, C_t, results from the combined effects of the forget gate, input gate, and the tanh function layer, as expressed in equation (1.1.11).

The entire process is mathematically detailed in equations (1.1.8 to 1.1.11), where W represents the weights, b signifies the bias, σ denotes the sigmoid function, while f_t, i_t and $\widetilde{C}_t$ represent intermediate values.

$$f_t = \sigma\left(W_f \cdot [h_{t-1}, x_t] + b_f\right) \tag{1.1.8}$$

$$i_t = \sigma\left(W_i \cdot [h_{t-1}, x_t] + b_i\right) \tag{1.1.9}$$

$$\widetilde{C}_t = \tanh\left(W_C \cdot [h_{t-1}, x_t] + b_C\right) \tag{1.1.10}$$

$$C_t = f_t * C_{t-1} + i_t * \widetilde{C}_t \tag{1.1.11}$$

Ultimately, the output of the current layer, h_t, is determined by processing the filtered cell state. This involves two key steps: first, applying the tanh function, and then multiplying the result by the output from the "*output gate*." The mathematical representation of this process is provided in equations (1.1.12) and (1.1.13).

$$o_t = \sigma\left(W_o \cdot [h_{t-1}, x_t] + b_o\right) \tag{1.1.12}$$

$$h_t = o_t * \tanh\left(C_t\right) \tag{1.1.13}$$

In this study, our goal is to train a neural network capable of predicting the extracted activation signals based on shoulder kinematics. Since both of these datasets are time-series data, it's crucial to employ a model well-suited for handling such temporal information. Given our discussed characteristics, we have chosen to build our neural network model using the Long Short-Term Memory (LSTM) architecture.

1.1.4 Deep Reinforcement Learning (DRL)

In the second chapter of this thesis, we delve into the creation of synthetic motion data using the Deep Reinforcement Learning (DRL) algorithm. DRL represents the fusion of deep learning techniques with reinforcement learning theory [57]. It's a framework that enables an agent to engage with its environment and adjust its actions based on the feedback it receives. DRL has successfully solved previously considered insurmountable problems using traditional approaches [58]. In our study, we take advantage of the phenomenon of synergy emergence observed during the DRL learning phase of a humanoid arm agent. This enables us to learn and replicate human-like reaching movements of the arm. To provide a solid foundation for the concepts explored in the following chapters, this subsection offers an explanation of the essential background of DRL.

A reinforcement learning (RL) algorithm can be mathematically described as an infinite-horizon Markov decision process (MDP), which is formally defined by the tuple $(\mathcal{S}, \mathcal{A}, p, r)$. In this tuple, the state space $\mathcal{S}$ and the action space $\mathcal{A}$ are both continuous, and we have the state transition probability $p : \mathcal{S} \times \mathcal{A} \times \mathcal{S} \to [0, \infty)$, representing the probability density of transitioning to the next state $\boldsymbol{s}_{t+1} \in \mathcal{S}$ given the current state $\boldsymbol{s}_t \in \mathcal{S}$ and action $\boldsymbol{a}_t \in \mathcal{A}$. Additionally, $r : \mathcal{S} \times \mathcal{A} \to \mathbb{R}$ signifies the reward bestowed by the environment at each transition. The symbol ρ_π denotes the trajectory distribution that results from following a policy $\pi(\boldsymbol{a}_t|\boldsymbol{s}_t)$. The visual representation of the fundamental RL framework is illustrated in Figure 1.7.

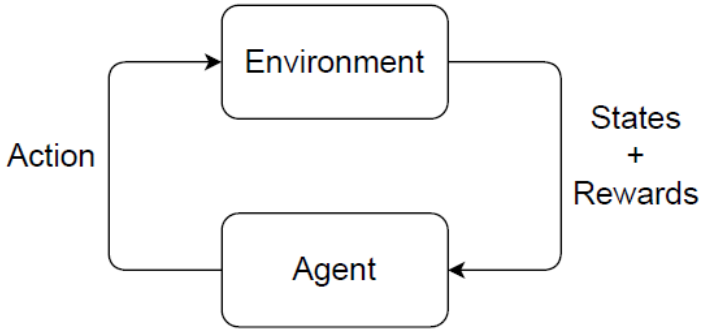

Figure 1.7: The Fundamental Reinforcement Learning (RL) framework, where an agent engages with the environment through interactive actions. Consequently, the agent obtains feedback about the environmental state triggered by its actions, along with rewards for each action, facilitating the adaptation of the agent's behavior over time.

In Reinforcement Learning (RL), we employ two fundamental metrics to assess the utility of states and actions within the agent's interaction with the environment. The Value Function denoted as $V^\pi(s)$ and expressed in Equation (1.1.14), quantifies a state's value based on the expected $\mathbb{E}_{\tau\sim\pi}[R(\tau)]$ achievable through a trajectory τ initiated from the state s, following the policy π. Correspondingly, to gauge the effectiveness of an action a within a given state s, we utilize the Q function, $Q^\pi(s, a)$, as depicted in Equation (1.1.15). The Q function provides insight into the anticipated return $\mathbb{E}_{\tau\sim\pi}[R(\tau)]$ stemming from the trajectory τ commencing at state s and action a while adhering to policy π.

$$V^{\pi}(s) = \mathbb{E}_{\tau\sim\pi}\left[R(\tau)|s_0 = s\right] \tag{1.1.14}$$

$$Q^{\pi}(s,a) = \mathbb{E}_{\tau\sim\pi}\left[R(\tau)|s_0 = s, a_0 = a\right] \tag{1.1.15}$$

To derive the accurate value function $V^*(s)$ and the precise Q function $Q^*(s,a)$, the Bellman equations come into play. These equations facilitate the refinement of the value function $V^{\pi}(s)$ and the Q function $Q^{\pi}(s,a)$, as demonstrated in Equation (1.1.16) and Equation (1.1.17), respectively.

$$V^{\pi}(s) = \mathbb{E}_{a\sim\pi, s'\sim P}\left[r(s,a) + \gamma V^{\pi}(s')\right] \tag{1.1.16}$$

$$Q^{\pi}(s,a) = \mathbb{E}_{s'\sim P}\Big[r(s,a) + \gamma \mathbb{E}_{a'\sim\pi}[Q^{\pi}(s',a')]\Big] \tag{1.1.17}$$

In DRL, the two functions $V^{\pi}(s)$ and $Q^{\pi}(s,a)$ are frequently estimated using neural networks with specific parameter sets. These estimated functions are denoted as $V_{\psi}(s)$ and $Q_{\phi}(s,a)$, where ψ and ϕ represent the parameters of their respective neural networks.

For the research conducted in this thesis, it was imperative to select a DRL algorithm capable of addressing the intricate task of manipulating an anthropomorphic 7-DOF robotic arm agent. In pursuit of this goal, Soft Actor-Critic (SAC) [59] is chosen being the state-of-the-art DRL algorithm.

Soft Actor-Critic (SAC) Algorithm

SAC stands for "*Soft Actor-Critic*", a stochastic DRL algorithm designed to acquire a policy $\pi_{\theta}(\boldsymbol{a}_t|\boldsymbol{s}_t)$ that links an agent's state to a probability distribution of actions, from which an action is selected to optimize the objective functions. SAC is distinctive in its approach: it learns a policy by concurrently maximizing the expected Q values and the expected entropy of the policy, $H(\pi_{\theta}(a_t|s_t))$, with the latter weighted by a temperature parameter α, as depicted in Equation (1.1.18). The entropy of the policy, $H(\pi_{\theta}(a_t|s_t))$, can be mathematically expressed as shown in Equation (1.1.19).

$$J_{\pi}(\theta) = E_{s_t\sim\rho_{\pi_{\theta}}}\Big[E_{a_t\sim\pi_{\theta}}\left[Q_{\phi}(s_t,a_t) + \alpha\cdot H(\pi_{\theta}(a_t|s_t))\right]\Big] \tag{1.1.18}$$

$$H(\pi_{\theta}(a_t|s_t)) = -log(\pi_{\theta}(a_t|s_t)) \tag{1.1.19}$$

Maximizing the expected entropy, as highlighted in [59], results in a policy that offers a diverse range of action choices, all leading to roughly equivalent rewards in a

given state. Their research demonstrates that this enhances exploration, accelerates learning, and significantly diminishes sub-optimal solutions.

The cost function used to update the Q_ϕ function is expressed in Equation (1.1.20), where $V_\phi(s_t)$ corresponds to the V function outlined in Equation (1.1.21). Here, ϕ_{trag} represents the parameters for the target networks.

$$J_Q(\phi) = E_{(s_t,a_t,s_{t+1})\sim\rho_{\pi_\theta}}\left[\frac{1}{2}\Big(Q_\phi(s_t,a_t) - \big(r(s_t,a_t) + \gamma V_{\phi_{trag}}(s_{t+1})\big)\Big)^2\right] \tag{1.1.20}$$

$$V_\phi(s_t) = E_{a_t\sim\rho_{\pi_\theta}}\left[Q_\phi(s_t,a_t) + \alpha \cdot H(\pi_\theta(a_t|s_t))\right] \tag{1.1.21}$$

Lastly, the temperature parameter α is automatically fine-tuned to maintain the policy entropy, $H(\pi_\theta(a_t|s_t))$, at a level approximately equal to the user-defined target entropy, H_{targ}. The cost function for adjusting the temperature is formulated as shown in Equation 1.1.14.

$$J(\alpha) = E_{a_t\sim\rho_{\pi_\theta}}\left[-\alpha log(\pi_\theta(a_t|s_t)) - \alpha H_{targ}\right] \tag{1.1.22}$$

The detailed training process of the SAC algorithm is depicted in the algorithm loop presented in 1.1.

Table 1.1: Training loop of the SAC algorithm.

Algorithm: *Soft Actor-Critic (SAC)*

Initialize policy parameters θ, Q function parameters ϕ_1; ϕ_2,
an empty replay buffer $\mathcal{D}$, the update frequency f, the number updates n,
learning rates λ_Q, λ_θ, λ_α
Set target parameters equal to main parameters $\phi_{targ_1} \leftarrow \phi_1, \phi_{targ_2} \leftarrow \phi_2$
Repeat
    Observe the current state s and sample an action $a \sim \pi_\theta(\cdot|s)$
    Execute a in the environment
    Observe the next state $s^{'}$, the reward r, and the terminal signal d
    Store $(s, a, r, s^{',d)}$ in the replay buffer $\mathcal{D}$
    If $s^{'}$ is terminal (d is true), reset the environment state.
    if iteration iter modulo f **then**
        for n times **do**
            Sample a batch of transitions, $B = (s, a, r, s^{',d)}$ from $\mathcal{D}$
            Update Q functions by one step of gradient descent using:
$$\phi_i \leftarrow \phi_i - \lambda_Q \bigtriangledown_{\phi_i} J_Q(\phi_i) \text{ for } i = 1, 2$$
            Update the policy by one step of gradient ascent using:
$$\theta \leftarrow \theta + \lambda_\theta \bigtriangledown_\theta J_\pi(\theta)$$
            Update temperature α with:
$$\alpha \leftarrow \alpha - \lambda_\alpha \bigtriangledown_\alpha J(\alpha)$$
            Update target networks with:
$$\phi_{targ_i} \leftarrow \rho\phi_{targ_i} + (1 - \rho)\phi_i \text{ for } i = 1, 2$$
        end for
    end if
until convergence

1.2 Research Objectives

1.2.1 General Objectives

This research aims to develop and evaluate an intuitive control strategy based on the residual limb motion approach for the simultaneous control of two DOFs in a transhumeral prosthesis during reaching movements: the elbow pronation-supination angle and elbow flexion-extension angle. The thesis comprises three primary chapters, each with distinct objectives that are interconnected. The general objectives are:

- Conduct a synergistic analysis of human arm reaching movements and integrate the most significant synergy components into the learning process of an ANN to construct the synergy-space neural network. This aims to improve the predictive model's transferability for amputee users.
- Develop a motion-cloning framework capable of generating human-like synergistic arm-reaching motions using a physics simulation and DRL-based arm manipulation. Evaluate the effectiveness of the cloned motion data to enhance and diversify the limited training data for training the ANN in predicting natural elbow motion. This addresses the challenge of obtaining sufficient training data for effective ANN training.
- Create a real-time interactive touching simulation using Unity 3D and integrate head movements into the predictive model for real-time estimation of the elbow joint motion during extensive arm-reaching activities. The objective is to improve the predictive model's performance by incorporating head movements as an additional input signal.

1.2.2 Specific Objectives

- Investigate motor synergy concepts and review related literature on synergy.
- Explore residual limb motion concepts and relevant research.
- Utilize a non-invasive method to record motion data during reaching movements through an inertial measurement unit (IMU) sensor-based motion capture system.
- Conduct a kinematic synergy analysis of human arm movements during reaching tasks.
- Apply the residual limb motion approach to predict elbow joint motion during reaching movements using LSTM neural networks.
- Integrate extracted synergies from reaching movements into the learning process to implement the synergy-space neural network.

- Validate the proposed methodology's effectiveness in predicting elbow joint motion and improving model transferability across diverse subjects.
- Examine concepts of Deep Reinforcement Learning (DRL) and explore energy-efficient motion learning research.
- Develop a DRL-based simulation framework for generating synthetic human-like arm reaching motion.
- Compare and analyze the similarity between DRL-based synthetic motion data and actual human subject motion data for similar reaching tasks.
- Showcase the effectiveness of cloned motion data in training ANN models to accurately predict natural elbow motion across various subjects.
- Demonstrate the benefits of motion data augmentation by combining real and cloned datasets to enhance model robustness and diversify training data.
- Study Unity 3D and virtual reality (VR) simulation concepts.
- In the final phase of the thesis, create a real-time interactive touching simulation in Unity 3D, utilizing the Neuron Pro motion capture system and Oculus VR headset.
- Incorporate head movement data as an additional signal to enhance predictive model training for far-reaching movements.
- Assess the predictive model's real-time performance in estimating elbow joint motion during far-reaching activities.
- Highlight the efficacy of the proposed methodology.

1.3 Related Work

The advancement of robust computing resources and sophisticated signal processing techniques has ushered in a remarkable era in prosthetic manipulation, representing a significant leap toward realizing the ultimate prosthetic device. However, several critical challenges must be overcome before these advancements can truly benefit the broader amputee population. With the background of several key concepts explained in the previous section, this section introduces works closely aligned with the themes of this thesis.

1.3.1 Human Motor Synergy Studies

Considering that the concept of motor synergy originates from human studies, it's valuable to delve into related research on motor synergy within human motor control. In one notable study [60], researchers examined the hand movements of infants at various developmental stages as they reached for and grasped toys. This investigation indirectly shed light on the development of motor synergies as infants grew and learned. Figure 1.8 visually illustrates the characteristic movements of infants at ages 19, 29, and 42 weeks, spanning the pre-reaching, early-reaching, and stable-reaching phases of development.

Initially, as seen in Figure 1.8a(A), infants exhibit rather erratic and indirect movements when reaching for objects during their first few months of life. However, with age and practice, their reaching and grabbing actions become faster and smoother, reducing the high variability observed during early reaches, as seen in Figure 1.8c(A). Furthermore, the coordination between the shoulder and elbow joints during early reaches, as depicted in Figure 1.8a(C), is notably poor and inconsistent. However, as they transition into a stable reaching period, the phase portrait reveals a more synchronized relationship between the shoulder and elbow joint angles, as illustrated in 1.8c(C). This alignment signifies that the motion of the shoulder and elbow becomes tightly coupled. These findings suggest that infants enhance their motor control proficiency through repetitive practice, gradually acquiring motor synergies that facilitate more efficient and coordinated movements.

In [37], the authors delved into the spatiotemporal organization of muscle patterns during fast-reaching movements, a study closely related to the themes of this thesis. Their investigation involved recording electromyographic (EMG) activity in up to 19 shoulder and arm muscles during point-to-point movements. These movements encompassed trajectories between a central location and one of eight peripheral locations arranged in either the sagittal or frontal plane, as depicted in Figure 1.9. The study examined these movements under varying conditions, such as different loads on the hand (experiment 1, see Figure 1.9 (a), (b)) and different forearm postures (experiment 2, see Figure 1.9 (d)). They also explored more intricate reaching movements (experiment 3, see Figure 1.9 (f), (g)), including continuous reversals from one central or peripheral position to another and movements from one peripheral position through the central position to another.

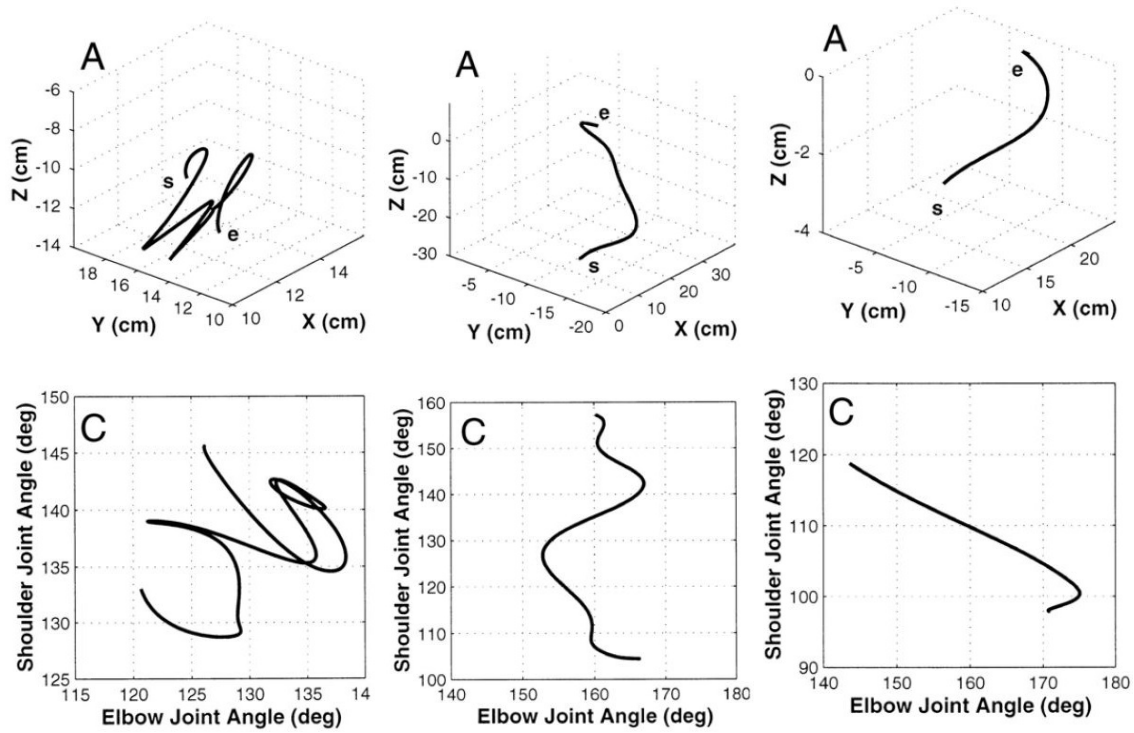

(a) Pre-reaching period (b) Early-reaching period (c) Stable reaching period

Figure 1.8: Experimental results from [60]. Hand trajectories from start to endpoint (A) and phase portraits showing the relationship between shoulder and elbow joint angles (C) for infants at 19 (a), 29 (b), and 42 (c) weeks of age.

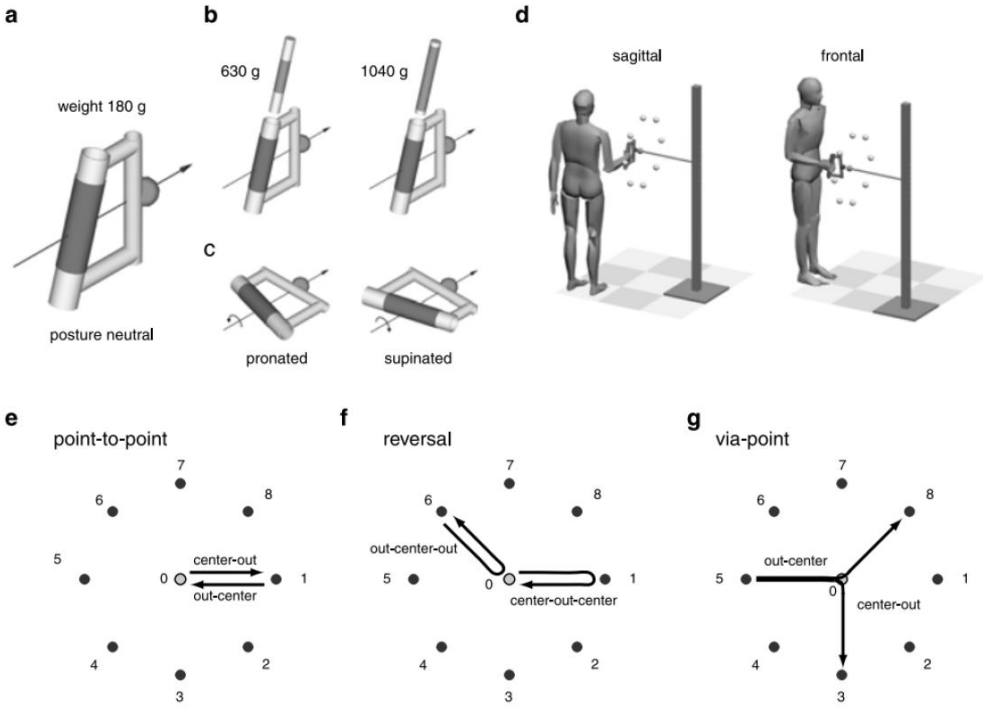

Figure 1.9: Experimental setup and conditions in [37] for fast-reaching movement control.

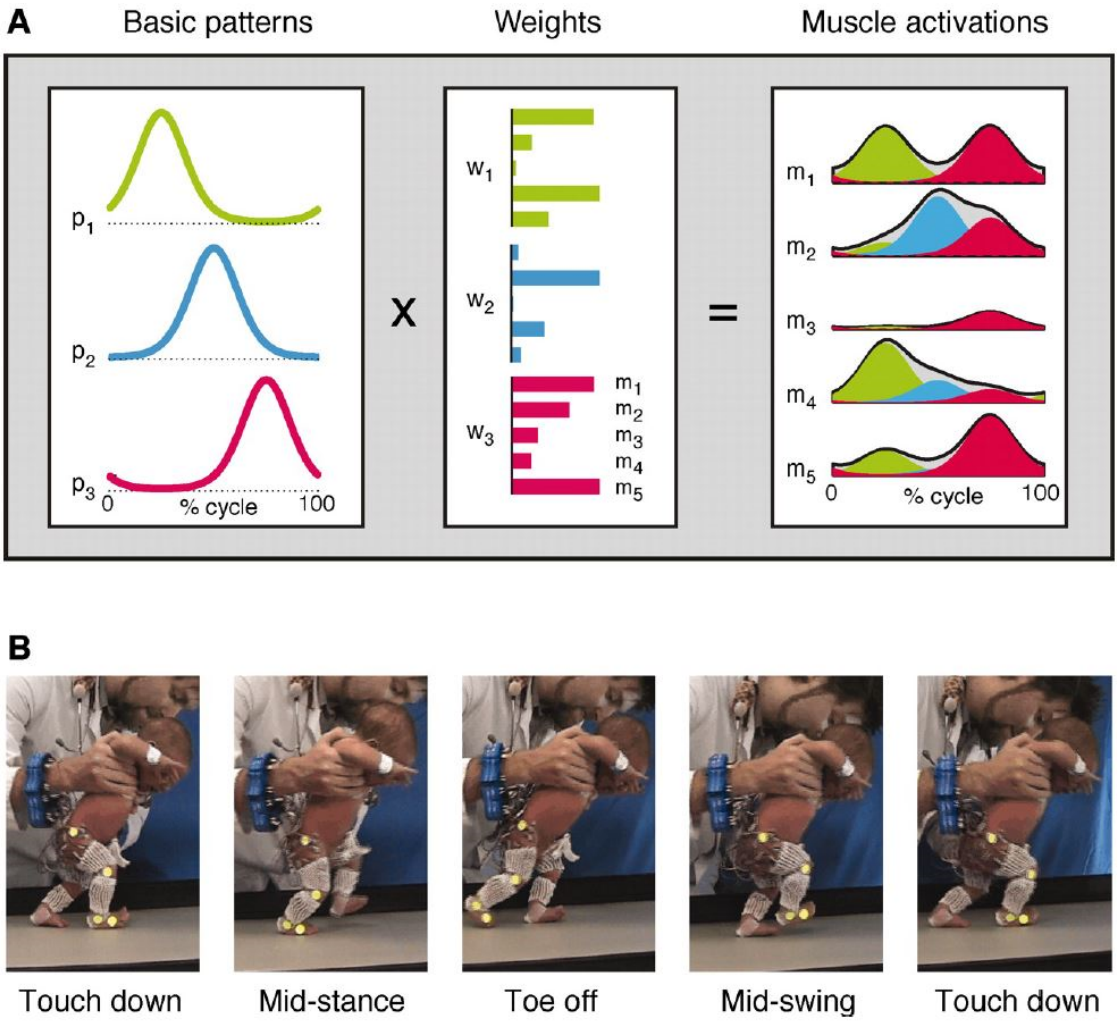

Figure 1.10: Synergy analysis of human walking as performed in [39]. In (A), the weights W_i represent spatial synergy components, and the basic patterns are denoted as activation signals C_i, as explained in preceding sections. (B) illustrates various walking phases in a baby.

The study aimed to determine if synergies could effectively reconstruct muscle patterns observed during point-to-point movements. The findings highlighted that the intricate muscle patterns involved in reaching movements could be represented by a small number of combinations of components, underscoring the role of low dimensionality in simplifying motor control. This phenomenon closely aligns with the concept of motor synergies in human motion when executing various tasks.

In [39], the authors employed PCA to investigate synergy development in human learning processes, as depicted in Figure 1.10. Additionally, the discussions in [33] regarding the role of muscle synergies in simplifying motion generation bear relevance to this thesis. Furthermore, studies in [61][62] explored the relationship between muscle synergies, performance, and energy consumption. Although this thesis focuses on the analysis of arm joint angular kinematic motion data rather than EMG and muscle synergies, the foundational concepts explored in these studies underpin the approach adopted here.

1.3.2 Automatic Prosthetic Elbow Control Strategy Using Residual Limb Motion

It is widely acknowledged that distal joint motion, such as elbow movement, can be effectively approximated using either upper arm electromyography (EMG) signals or proximal joint kinematics, like shoulder motion. Numerous studies have employed both methods to devise control strategies for transhumeral prostheses, demonstrating satisfactory performance in various reaching tasks. Our study advances the field by enhancing the residual limb motion strategy for automatic prosthetic elbow joint control, with a particular emphasis on leveraging shoulder kinematics.

In a related study [53], researchers successfully predicted elbow angular velocities based on shoulder kinematics during 3D pointing movements. To collect motion data, they employed both camera-based motion capture and an IMU sensor. Participants were instructed to point at various targets presented by a WAM arm robot while seated in an upright position, as depicted in Figure 1.11. The study utilized a radial basis functions network (RBFN) based regression algorithm to establish the connection between shoulder kinematics and elbow angular velocities.

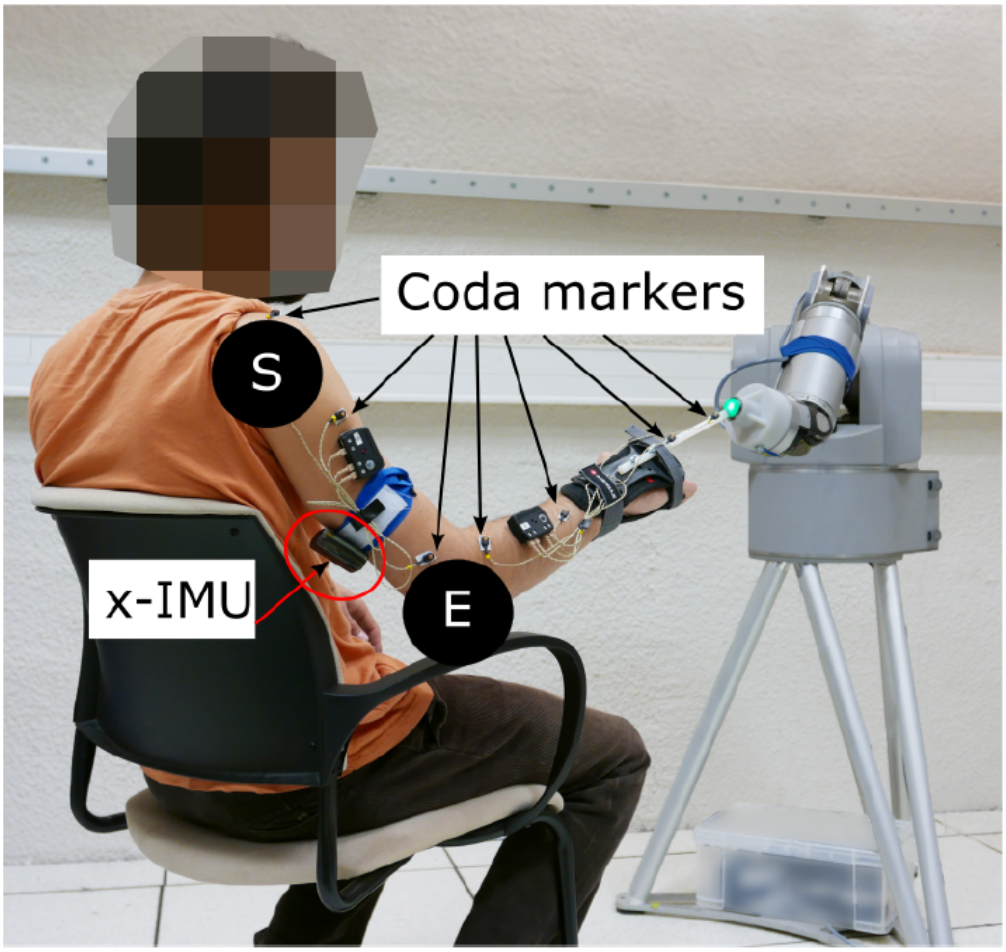

Figure 1.11: The experimental setup in [53] for pointing at various targets provided by WAM arm in 3D.

Furthermore, another investigation [49] compared myoelectric control and automatic control strategies for prosthetic elbow motion. The research uncovered that myoelectric control often led to significant compensatory trunk movements by users to adjust the final position of the end-effector. Conversely, the joint coordination strategy reduced the need for such compensatory movements.

Additionally, findings from a study [63] in which reaching movement data was recorded from a healthy subject indicate that overall estimation accuracy can be enhanced by using a combination of both signals as input. When compared to using upper arm EMG signals alone, predictions based on shoulder kinematics performed better. However, it's essential to note that the impact of prolonged EMG signal usage on ANN performance remains to be fully explored, as the quality of EMG signals tends to deteriorate over time due to factors like muscle fatigue, electrode placement, and skin impedance. In some cases, acquiring quality EMG signals may necessitate invasive surgical procedures like TMR.

The authors in [64] delves into the empirical evaluation of automatic prosthetic elbow control in the context of a reaching task, drawing comparisons with traditional myoelectric control. Six transhumeral amputees, including three with osseointegrated devices, participated in the study. The task was successfully accomplished within physiologically acceptable margins of error for both control methods. Notably, automatic elbow control substantially mitigated trunk compensatory movements and reinstated a more physiologically aligned coordination between shoulder and elbow movements, as depicted in Figure 1.12.

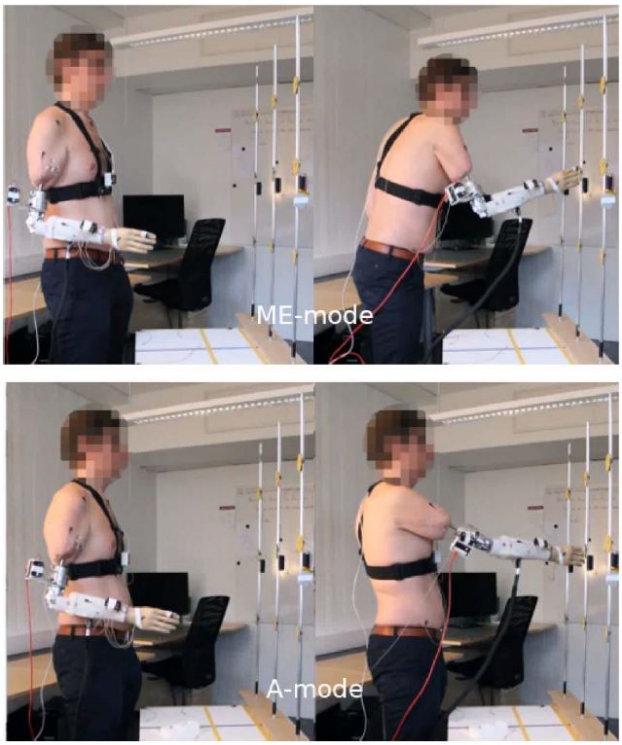

Figure 1.12: The experimental setup in [64] for reaching movements with initial and final postures towards the target with the ME-mode (myoelectric control) and with the A-mode (automatic elbow control).

It was observed through kinematic assessment that amputation and the use of prosthetic devices led to deviations in shoulder movements compared to typical physiological shoulder kinematics. Participants reported that the automatic elbow control strategy was intuitive, underscoring the potential value of automated prosthetic elbow motion.

However, in the case of the residual limb motion strategy, creating an inter-joint coordination model necessitates data from healthy subjects, as it's challenging to record such data from transhumeral amputees. One potential solution involves constructing a generic model by amalgamating inter-joint coordination data from multiple healthy subjects. Additionally, it's noteworthy that many studies employ artificial neural networks (ANNs) for their inter-joint coordination models without extracting prior information from the kinematic data of arm movements. The primary focus of the first study in this thesis is to bridge this gap, enhancing the model's transferability to amputee users.

1.3.3 Motor Synergy in Deep Reinforcement Learning

While the motor synergy concept is primarily explored in the context of human subjects, several studies have demonstrated its applicability and significance in optimal robotics control. This concept extends to the coordination of multiple robotic joints, which is essential for achieving optimal task performance.

In their study [65], the authors conducted experiments utilizing Deep Reinforcement Learning (DRL) algorithms to manage full-dimensional arm manipulation within a simulation environment. Their objective was to investigate the relationships between motion error, energy consumption, and the emergence of synergy during the learning process, shedding light on the mechanisms underlying the utilization of motor synergy. Notably, synergy information was not explicitly incorporated into the reward function; instead, synergy naturally emerged in conjunction with feed-forward control, mirroring human motion learning processes. Two types of DRL controls were examined: a simple DRL approach and a hybrid "PDRL" method, which combined a Proportional-Derivative (PD) controller with a DRL controller. These control schemes were applied to both a 3-DOF planar robotic arm for tracking a 2-D line and an anthropomorphic 7-DOF robotic arm for horizontal tracking of a 3-D circular trajectory, allowing for an analysis of motion behaviors during the learning process, as illustrated in Figure 1.13.

Figure 1.14 displays the R^2 curves at various training checkpoints for the 7-DOF agent. In this representation, the purple and blue curves represent the early training phase, while the green and red curves correspond to the later stages of training for the DRL and PDRL methods, respectively. As training progresses, the synergy level within the curves tends to increase for DRL and PDRL. This is evidenced by the convergence of fewer synergy components to achieve higher R^2 accuracy, as exemplified by the orange arrows in Figure 1.14. This observation underscores the tendency for motion to become more synergetic throughout the learning process.

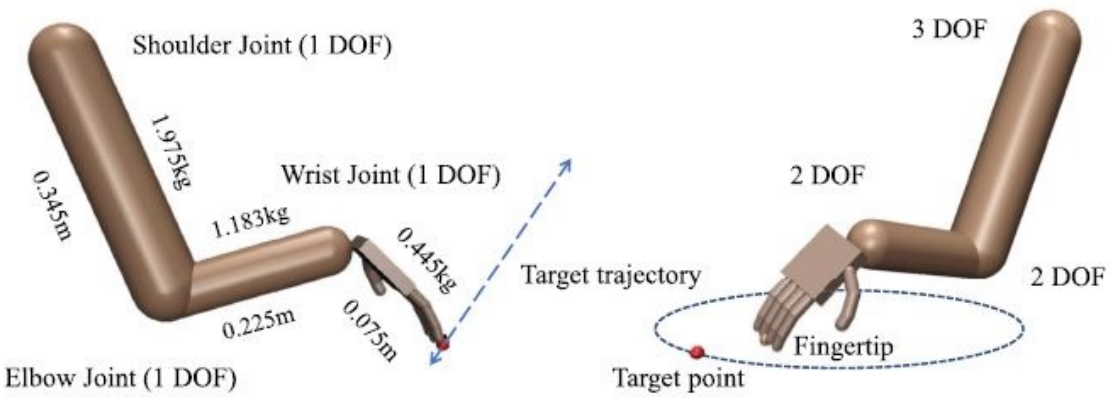

Figure 1.13: Simulated robotic agent configurations from [65]. The left arm represents vertical tracking for a 2-D line using a 3-DOF planar arm, while the right arm represents horizontal tracking for 3-D circular trajectories using a 7-DOF arm.

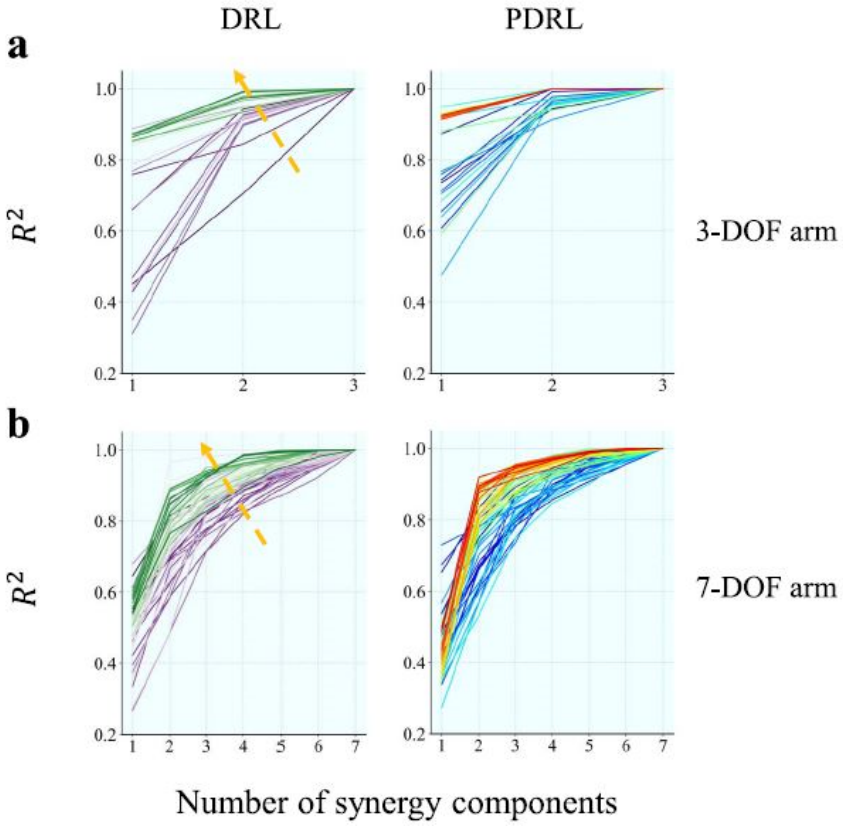

Figure 1.14: Experimental simulation results from [65] presenting R^2 accuracy curves for all checkpoints are overlaid in different colors, depicting performance under both DRL and PDRL control.

The authors of [40] conducted an investigation into joint-space synergy analysis of multi-joint running agents within simulated environments. They employed two cutting-edge deep reinforcement learning algorithms, Soft Actor-Critic (SAC) and Twin Delayed Deep Deterministic Policy Gradients (TD3), to train robotic agents from the OpenAI Gym library [66]. Specifically, they worked with three agent variants: HalfCheetah (HC), Heavy HalfCheetah (HeavyHC) with twice the weight,

and FullCheetah (FC). Each variant was trained with 15 different random seeds for both algorithms, accumulating a total of 3 million training time steps. Their study delved into the exploration of joint synergies within simulated robotic agents trained using these DRL algorithms, as depicted in Figure 1.15.

In [40], the authors successfully bridged two distinct domains of research: the human motor synergy concept and Deep Reinforcement Learning (DRL) for robotics. Their work unveiled intriguing connections between these domains. Notably, the synergy-related metrics highlighted SAC's superior learning capabilities compared to TD3. This finding suggests that embracing the synergy concept could be pivotal when designing new DRL algorithms for robotics. Integrating synergy constraints can expedite robotic agents' learning process, resulting in enhanced performance and energy efficiency.

As far as we are concerned, there is a lack of closely related work concerning the use of DRL algorithms for generating synthetic motion data and investigating its application in predicting real human motion. In the second study of this thesis, we delve into DRL-based motion cloning, with a particular emphasis on its utilization for enriching and expanding the dataset for training neural networks to predict actual human arm reaching motions.

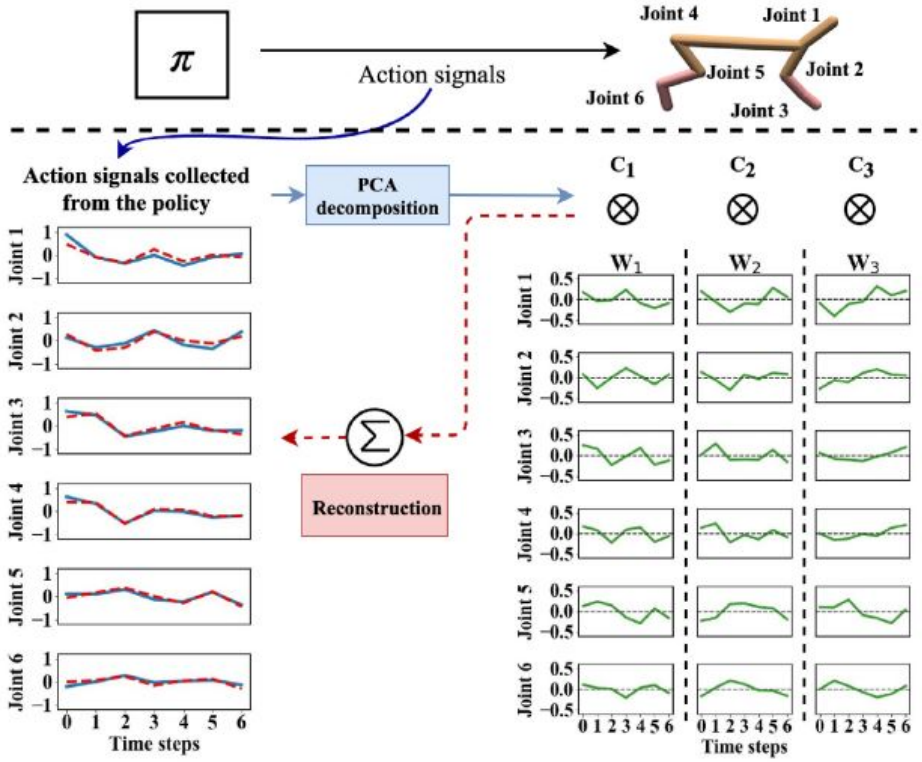

Figure 1.15: Illustration of the joint synergies extraction process in [40] utilizing PCA decomposition on action signals (blue) obtained from the policy π at specific training checkpoints. In this example, three spatiotemporal synergies are depicted by the matrices W_1, W_2, and W_3, along with their corresponding activation coefficients C_1, C_2, and C_3. The linear combination of W_i and C_i results in the reconstruction of the action signals (red).

1.4 Outline

This dissertation is organized into five chapters as follows.

Chapter 1: Introduction

In Chapter 1, we start by providing a concise overview of the motivation behind this thesis. After that, we discussed some important ideas we'll use throughout the thesis. We then proceed to discuss relevant previous research for the studies conducted in this thesis. Finally, we outline both the overarching and specific objectives of our research.

Chapter 2: Synergy-Space Recurrent Neural Network

Chapter 2 introduces the first study of this thesis, where we developed a synergy-space neural network as a transferable model for estimating forearm motion using residual shoulder movements during horizontal reaching tasks. This study proposes a novel approach that explicitly merges kinematic synergies with the learning system to overcome the limitations of conventional predictive models.

The primary objective was to establish a more robust and adaptable control strategy. Synergies, known for their repeatability and shared characteristics across similar tasks and subjects, served as a pivotal element. Thus, we extracted synergistic insights from movement data, selectively incorporating the most significant synergy components into the learning process. This strategic integration not only streamlines and enhances the training of the artificial neural networks (ANNs) but also capitalizes on the shared nature of these synergies, ultimately boosting model transferability. The study's results demonstrated our approach's effectiveness as a transferable decoder, accommodating variations between individuals and offering a more versatile model for controlling transhumeral prostheses.

The first study of this thesis was presented in a paper entitled "Synergy-Space Recurrent Neural Network for Transferable Forearm Motion Prediction from Residual Limb Motion", which was accepted for *Sensors*.

Chapter 3: Deep Reinforcement Learning-Based Synthetic Motion Cloning

Chapter 3 outlines the methodology for generating synthetic motion data using a DRL-based framework. This study introduces an innovative motion-cloning strategy to address the challenge of obtaining substantial training data required to effectively train an ANN. Our approach leverages the capabilities of DRL algorithms to replicate natural and human-like motion in simulated humanoid agents. We collected real motion data from human subjects as they performed multi-directional arm-reaching tasks in the horizontal plane. Using a physics simulation and DRL-

based arm manipulation, we generated synthetic motion data that emulated similar arm-reaching tasks.

Subsequently, we trained ANNs using various configurations of training motion data, including DRL, real, and hybrid data sets. Our evaluation results demonstrate the effectiveness of the cloned motion data in training the ANN to accurately predict natural elbow motion across multiple subjects. Additionally, the augmentation of motion data by combining real and cloned motion data sets showcases improved ANN robustness by supplementing and diversifying the limited training data.

The second study of this thesis was presented in a paper entitled "Transhumeral Arm Reaching Motion Prediction through Deep Reinforcement Learning-Based Synthetic Motion Cloning", which was accepted for *Biomimetics*.

Chapter 4: Real-time estimation of far-reaching movements

Chapter 4 focuses on the real-time prediction of elbow joint motion during arm-reaching movements. This study introduces a VR-based interactive framework for the real-time validation and evaluation of predictive models. The primary objective is to address challenges associated with clinical trials for testing transhumeral prosthesis control strategies on amputee subjects. We developed a 3D virtual workspace with a humanoid actor, enabling amputee subjects to easily control its movements by strapping on a few sensors on their body. This setup allows them to perform reaching tasks with the full range of arm motion. Our experiments and validation were conducted in the virtual workspace, initially utilized for data acquisition from healthy human subjects, and later employed to validate the efficacy of trained ANNs on an amputee subject.

Our evaluation results underscore the effectiveness of the trained ANN and the VR platform. We successfully demonstrated a right-arm transhumeral amputee executing arm-reaching movements in the virtual workspace. Despite the participant's lack of prior experience with the task or familiarity with the apparatus, our ANN model accurately predicted the motion of his amputated elbow in real-time. This capability enabled the subject to successfully reach and touch all target points in the virtual workspace. These findings bear significant implications for creating comprehensive virtual workspaces encompassing diverse arm movements, covering various activities. This approach proves valuable for validating and advancing strategies in transhumeral prosthesis control.

Chapter 5: Conclusion and Future Work

Finally, chapter 5 provides a summary of the key findings from the preceding chapters. It also outlines the primary contributions of this thesis and offers insights into potential areas for future research.

Chapter 2

Synergy-Space Recurrent Neural Network

2.1 Introduction

Amputation of the upper limb at any level can considerably affect an individual's ability to perform the activities of daily living (ADLs). The proficiency for such activities decreases with higher amputation levels [4]. The general requirements of prosthetic users can be primarily summarized as intuitive control, ease of use, and sensory feedback [6], [7]. With the advancements in robotics and sensor technologies, very sophisticated and state-of-the-art upper extremity prostheses such as the DEKA arm [11] and modular prosthetic limb [12] are currently available. However, one of the persistent drawbacks is the interface between the prosthetic device and the user, attributable to the growing gap between the control methods and hardware improvements for prosthesis development.

In the myoelectric control domain, which is the most widely used control approach for prosthetic arms [14], the number of input signals a user can provide is always less than the degree of control (DOC). The DOC refers to the number of functions of a prosthetic device controllable by the user. Hence, this issue is even more critical for the case of transhumeral amputees as they can only provide electromyography (EMG) signals from the upper arm. However, they must control a prosthesis with numerous active degrees of freedom (DOFs), such as a powered elbow, wrist, and hand. As feasible solutions, surgical innovations such as targeted muscle reinnervation (TMR) [14] and advanced signal processing techniques, such as pattern recognition [17], have been employed to classify more significant numbers of distinct commands from residual muscle activities.

Although such measures allowed transhumeral amputees better control over their multifunctional prosthetic arms, the control was slow, sequential, and unnatural as physiologically appropriate muscles were unavailable. Such counter-intuitive control strategies and a lack of functionality are often the reasons for the high rejection rates of these devices [18], [19]. Furthermore, the calibration requirements and signal

sensitivity issues associated with EMG-based control also challenge its continuous daily use.

Numerous investigations have been conducted to explore alternative solutions, such as those based on myokinetic signals [20] using the residual kinetic activity of the limb, ultrasound signals [21], mechanomyography [22] using vibrations caused by muscle contractions as the control signals, and the residual limb motion strategy [24], [25]. Bio-inspired learning approaches based on studying the central nervous system (CNS) and human motor control abilities have also been employed to develop more natural and intuitive arm control strategies [23].

Concerning the target reaching task or control of the prosthetic elbow joint motion in transhumeral amputees, the ideal case would involve the prosthetic device acting as a natural extension of the human body. A promising scheme to achieve this is automatically controlling the prosthetic elbow joint based on the natural relationships between the arm joints. Analyses of such joint coordination approaches have shown evidence that recurrent patterns exist in the joint kinematics for upper limb movements while performing reaching or grasping tasks. For example, between the elbow flexion and humeral inclination during reaching [26], between the hand azimuth and movement direction during grasping [27], as well as a variety of many other arm movements in ADLs [67]. These patterns are referred to as synergies.

In the present study, we have also focused on a synergistic method for intuitive control of the prosthetic elbow joint for transhumeral amputees. The majority of previous such motion-based approaches using residual limb motion rely on ANNs [30], [68] to identify and model the shoulder–elbow kinematic relationship, as inductive learning (IL) applied in [32] and radial basis function networks (RBFNs) used in [31], [69]. The ANN is typically trained to map the shoulder kinematics (provided as input) to the elbow or forearm kinematics (provided as output) through supervised learning. To the best of our knowledge, in such previous approaches, no prior synergistic information is extracted from the motion data used for training the ANNs. This type of approach, in simplistic terms, can be represented as in Figure 2.1a and is hereafter referred to as "direct estimation". However, the direct estimation method has a limitation due to its sensitivity to inter-individual variability. As a result, the performance of the model drops significantly when applied across multiple users, making it less suitable for generalization and transferability.

2.1.1 Transfer Learning Framework for Transhumeral Amputees

This paper presents the concept of the synergy-space neural network, whereby we explicitly combine the kinematic synergies with the learning system to address the limitation of the direct estimation method, aiming for a more robust and transferable control strategy. Synergies have been observed to be repeatable and shared across similar tasks and subjects. Therefore, we extract the synergistic information from the movement data and incorporate only the most significant synergy components in the learning process, enabling more precise and efficient training of the ANN

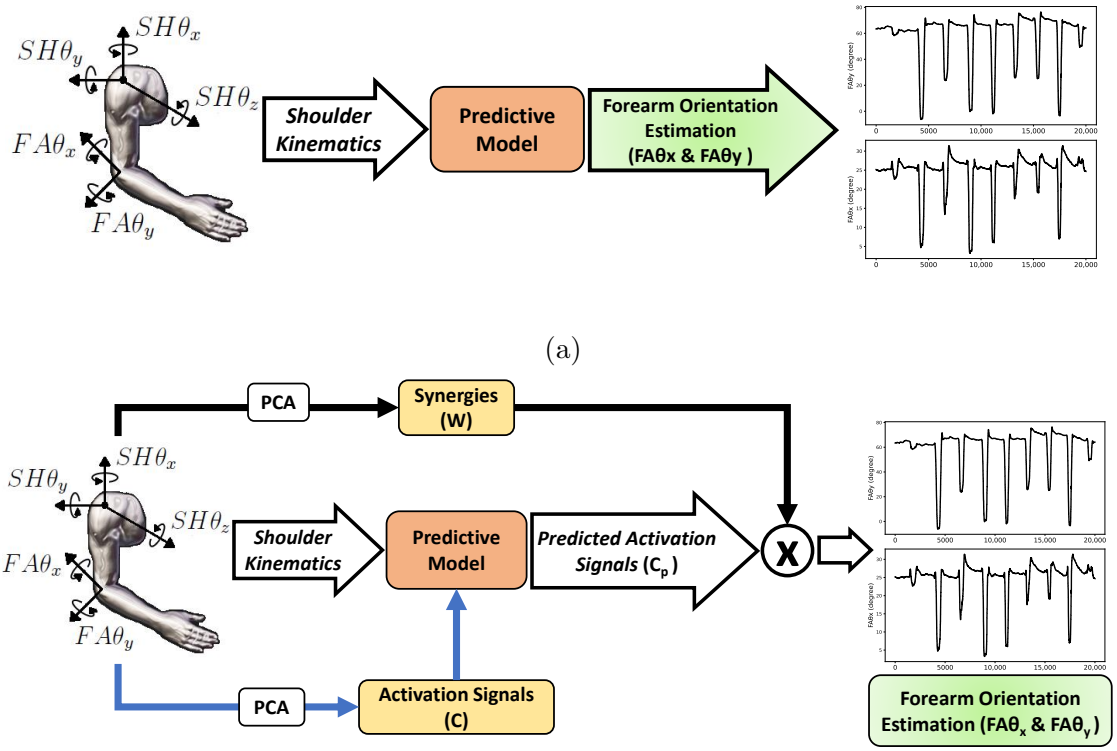

Figure 2.1: Illustration of the idea of this study: (**a**) a simplistic representation of direct estimation method; (**b**) the proposed synergy-space neural network method. Here, $SH\theta_x$, $SH\theta_y$, and $SH\theta_z$ are the shoulder kinematics, and $FA\theta_x$ and $FA\theta_y$ represent the forearm orientations. The PCA blocks symbolize the process of synergy extraction, where W represents the synergistic components and C is the corresponding activation signal matrix. The predictive model is the trained RNN that outputs the predicted activation signals C_p, with the cross-operator representing the matrix multiplication of the incoming values.

while taking advantage of the shared nature of these synergies enhancing the transferability of the model. The idea is to train the ANN to predict the corresponding activation signals (see Equation (2.2.1)), which estimates the forearm motion when combined with the extracted synergy matrix. Because the ANN is trained using the most significant synergy components, the synergy-space neural network can learn particular features common to the arm movement tasks, allowing for better cross-subject transferability. In addition, using a smaller number of synergy components aids the ANNs in learning good policies by reducing the dimensionality of the state space. Lastly, being a synergistic approach, it allows for the kinetically natural and energy-efficient motion estimation of the arm movements.

Figure 2.1b illustrates the overall workflow of the proposed synergy-space neural network approach. We first extract the spatial synergy components and their corresponding time-varying activation signals from the source data (see Equation (2.2.1)) using the principal component analysis (PCA). Long short-term memory (LSTM), a particular type of recurrent neural network (RNN), is then trained to predict the

extracted time-varying activation signals based on input shoulder kinematics. Finally, the forearm motions are estimated using Equation (2.2.2), where the extracted activation signals C are replaced with the LSTM-predicted signals C_p. Introduced by Hochreiter and Schmidhuber [70], the reason for using LSTM is its ability to learn long-term dependencies. LSTMs have internal mechanisms called gates that regulate the flow of information to handle the vanishing gradient problem in RNNs, making them very suitable for time-series prediction such as motion data or, in our case, time-varying activation signals. This paper proposes and evaluates the synergy-space neural network for forearm motion estimation, comparing its performance with the direct estimation approach. The contributions made in this paper are as follows:

- The implementation of the proposed synergy-space neural network as a transferable model for forearm motion estimation using residual shoulder kinematics during horizontal reaching movements.
- Personalized LSTM Models Evaluation: To validate the proposed methodology and its better learning capability through a detailed comparison between the performance of the synergy-space neural network and the direct estimation approach.
- Cross-Subject Evaluation: To demonstrate the strength of the synergy-space neural network as a transferable decoder, indicating its ability to handle inter-individual variabilities.

The remainder of this paper consists of the following sections:
Section 2.2 explains the materials and methods employed to achieve our objectives, describing the experimental protocol, synergy extraction, LSTM training and analysis, and evaluation strategy. Section 2.3 demonstrates the validity of the proposed method through the experimental results. Section 2.4 discusses the findings and limitations. Lastly, Section 2.5 concludes this paper and gives future direction.

2.2 Materials and Methods

2.2.1 Data Acquisition

Fourteen healthy right-handed subjects (thirteen males and one female) volunteered for this investigation. The subjects were 20–28 years old, with no known upper limb neuromuscular disorders. All subjects had given informed consent prior to participation in this experiment.

To record the motion data of a subject's arm movements during reaching tasks, we used Perception neuron pro, an inertial measurement unit (IMU) sensor-based full-body motion capture system. Although the accuracy of this system is inferior to that of optical cameras, it is possible to capture motions without spatial constraints from anywhere within the communicable range of the device. The device

uses individual sensors called neurons, each housing an IMU, attached to different body parts (Figure 2.2a). We used a total of eight sensors. Figure 2.2b shows the placement of each neuron—three on each arm (placed on the forearm, upper arm, and shoulder) and one each on the chest and lower back. The subjects can quickly wear the sensors using straps so that no additional preparations, such as special clothes, are necessary.

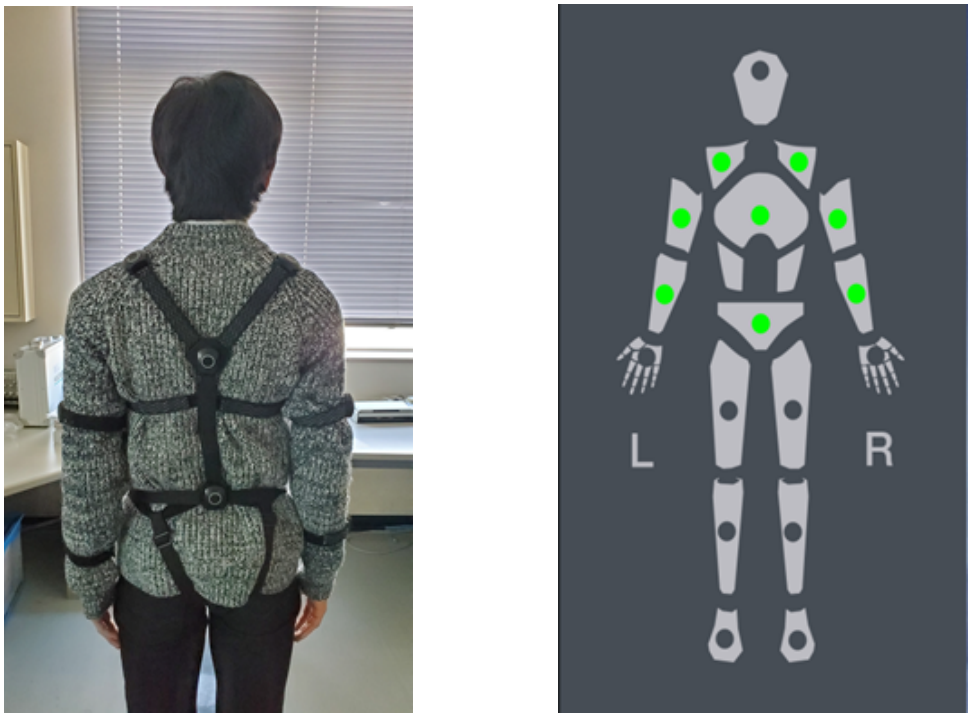

(a) (b)

Figure 2.2: Neuron pro sensor placements for capturing the required motion data: (**a**) subjects wearing neuron sensors; (**b**) green spots marking the placements of the sensors for the upper body mode of neuron pro because only arm movement data are required.

The sensor system communicates with the axis neuron pro software that processes raw motion data to formulate a 3D skeletal model in real time. Motion information from the developed skeletal model, such as the position and angle of each joint, can be obtained at a sampling frequency of 120 Hz. In our experiments, the data under consideration were the three shoulder orientation angles along X, Y, and Z axes, i.e., internal–external rotation, flexion–extension, and abduction–adduction of the shoulder joint, and two forearm orientation angles, i.e., pronation–supination and flexion–extension of the elbow joint; hereafter, these are referred to as $SH\theta_x$, $SH\theta_y$, and $SH\theta_z$ and $FA\theta_x$ and $FA\theta_y$, respectively.

2.2.2 Experimental Protocol

Bearing in mind that the purpose of a prosthetic device is to assist the user with their ADLs, we designed the workspace based on a routine activity by considering the user's everyday environment instead of constrained movements in a laboratory or restricted environment. Reaching for objects placed on a table is a common scenario in daily life, which also targets arm movements in the horizontal plane only, specifically on the top surface of a table. A 40 cm $\times$ 40 cm target grid (Figure 2.3a) with a start/rest point and 8 numbered points was placed in a horizontal position on the surface of a table. The target numbered point to be reached was projected on the screen in front of the subject. The timing and color of the displayed numbers were controlled automatically to produce more consistent and regular movements, based on which the subjects had to perform the required reaching tasks. The subjects were provided instructions at the beginning of the experiments and allowed time to familiarize themselves with the environment. Therefore, no verbal commands or communications were required during the experiments, thus making the procedures easier to follow. Eight healthy subjects participated in these behavioral experiments. They were tasked with performing reaching movements to explore the top surface of a table placed before them while sitting straight on a chair, as shown in Figure 2.3b. All the subjects performed two sets of tasks, and kinematic data were acquired for the reaching movements of only the right arm as follows:

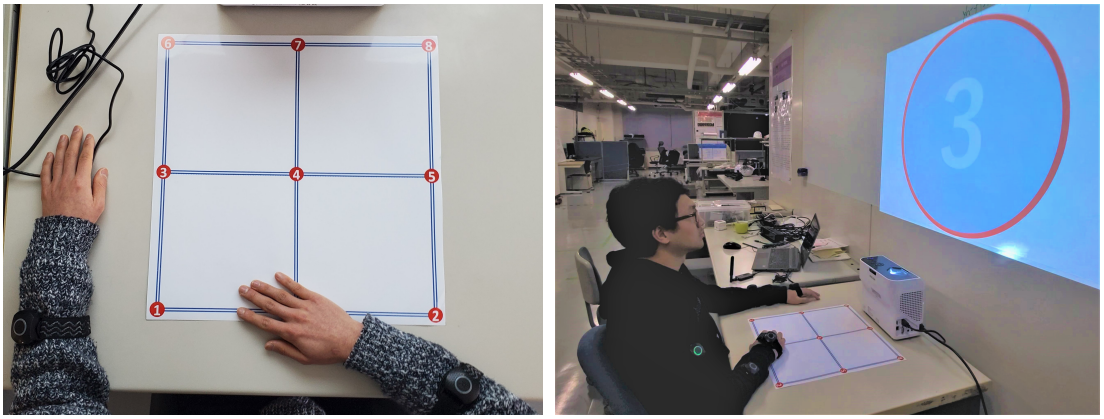

(a) Conventional Direct Estimation Method

(b) Synergy-Space Neural Network Method

Figure 2.3: Experimental setup for the target reaching tasks: (**a**) target grid with a subject's right hand at the start point; (**b**) complete experimental setup for the target reaching tasks.

- Dataset 1: with multiple (15 times) repetitive reaching movements toward each target point.
- Dataset 2: with reaching movements toward random target points (35 movements in total).

Dataset 1 with multiple repetitive movements was first used to extract the kinematic synergies and later as the training data for the neural network. Afterward, dataset 2, with reaching movements toward random target points, was used to cross-validate the trained neural network.

2.2.3 Kinematic Synergy Extraction

PCA has been used in numerous studies to investigate natural movements, such as catching [41] or reaching[45] tasks, where it was successful in representing the observed physiological complexities using fewer numbers of principal components (PCs) or synergies. One reason for this is that when capturing variances, the PCA uses a more intuitive method to exploit the coupling of the DOFs. Another important reason is that it considers linear correlations among the DOFs, which can be regarded as the minimal model of inter-joint coupling, i.e., a linear approach to explaining complex behaviors.

In this study, we performed a synergistic analysis using PCA as we are working with kinematic synergies. Dataset 1 was first segmented to acquire the data of interest, i.e., one individual reaching movement from the onset of the reaching motion until returning to the start/rest point (as in Figure 2.4). We then averaged the segmented data over the 15 trials for the same reaching movement, e.g., for target point 7. The averaged data were then low-pass filtered using a sixth-order Butterworth filter with a cutoff frequency of 10 Hz to remove motion artifacts and finally normalized to translate the angular values within the range of -1 to $+1$. For each subject, this averaged, filtered, and normalized dataset X (2.2.1) was obtained comprising submatrices $x_j^m(t_{max})$ with joint angular values during reaching motions. Here, $m = 8$ represents the total number of target points for the reaching tasks, $j = 5$ is the number of DOFs or joint angles under consideration, and t_{max} refers to a particular sample time for which the joints' angular values were obtained. The X having size $j \times (m * t_{max})$ is fed to the PCA algorithm, which then provides the PCs. Each PC is a synergy representing the covariation of the joint angular configurations. The total number of PCs or synergy components "N" (1.1.1) is equal to the number of DOFs or joint angles under consideration, which is equal to five here. Figure 2.5a represents the extracted kinematic synergy component matrix (graphical representation) for one of the subjects.

$$X = \begin{bmatrix} x_1^1(t_{max}) & \cdots & x_1^4(t_{max}) & \cdots & x_1^8(t_{max}) \\ x_2^1(t_{max}) & \cdots & x_2^4(t_{max}) & \cdots & x_2^8(t_{max}) \\ \vdots & \ddots & \vdots & \ddots & \vdots \\ x_5^1(t_{max}) & \cdots & x_5^4(t_{max}) & \cdots & x_5^8(t_{max}) \end{bmatrix} \tag{2.2.1}$$

We retained the minimum of the most significant PCs that explain at least $> 85\%$ of the total variance. Figure 2.5b presents the variations of the PCs for subject 1. We can observe that the first synergy accounts for more than 75% of the variance, and the sum of the first two synergies can account for more than 90% of the overall variance in the source data.

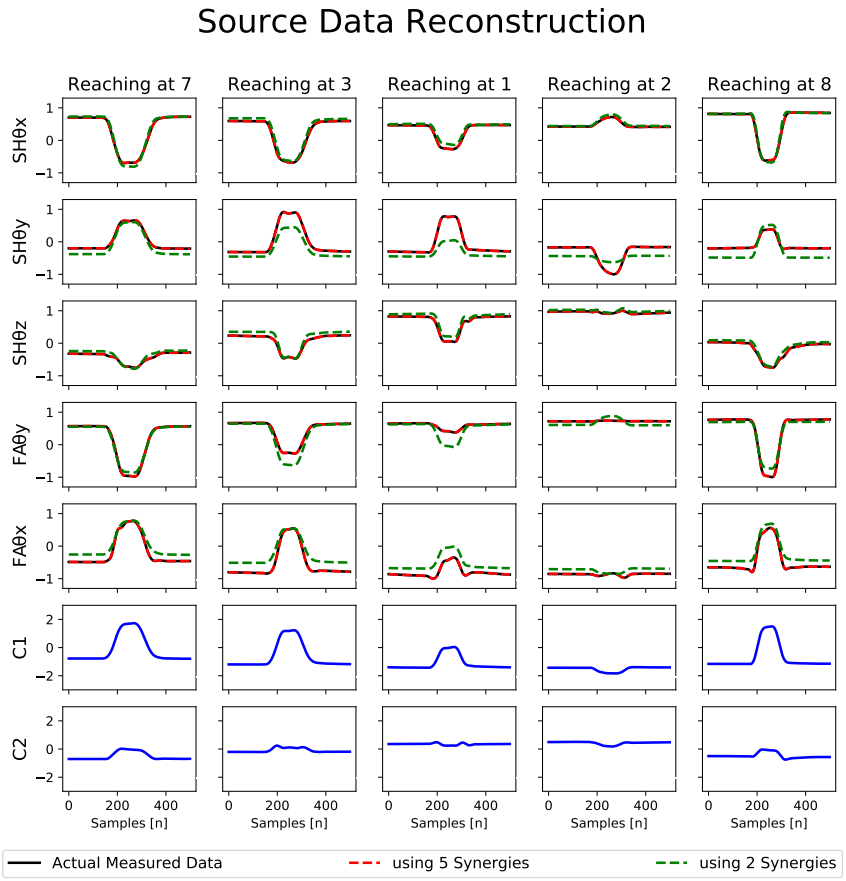

Figure 2.4: The first five rows represent the shoulder and elbow joints' angular values normalized between -1 and $+1$. It comprises the source data (solid black curves) of subject one and its reconstructions using all five synergies (red dotted curves) and only two synergies (green dotted curves). The last two rows represent the corresponding activation signals C (C1 and C2 in the case of two synergies).

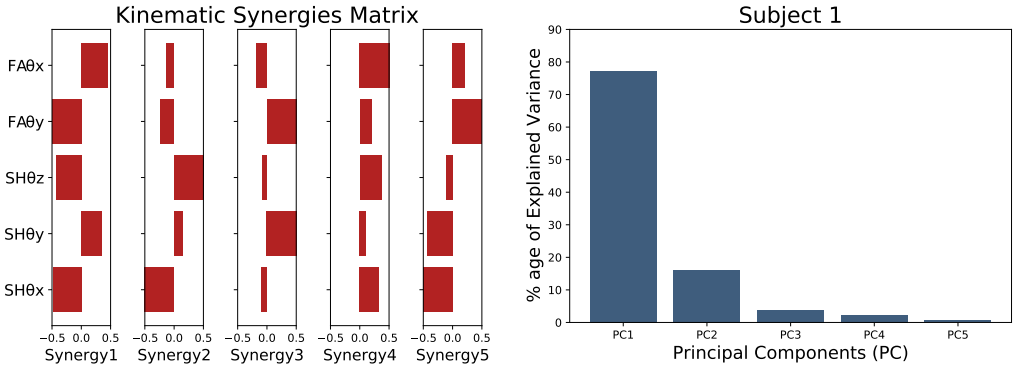

(a) (b)

Figure 2.5: Example of the kinematic synergies of subject 1. (**a**) The spatial synergies extracted from the training data. The notations $SH\theta_x$, $SH\theta_y$, $SH\theta_z$, $FA\theta_x$, and $FA\theta_y$ indicate the axis of the degree of freedom. (**b**) Bar plot showing the importance of each principal component in explaining the variance in the source data.

Following our set criteria, it suggests that we can adequately approximate the original data using only the first two synergies that capture a large portion of the variance. Thus, the subject's original movements can be reconstructed with an acceptable loss in accuracy.

Figure 2.4 also represents the difference in the reconstructed data for one of the subjects when represented using all five synergies (shown in red) and when using only two synergies (shown in green). It can be seen that the red curve is an exact match for the original movement data (shown in black). In contrast, the green curve still represents the original data reasonably accurately. The last two rows show the activation signals C (in blue) in the case of two synergies, i.e., C1 and C2. Based on these observations, using the synergy-space neural network approach, it is plausible to use only the first two synergies to estimate the forearm motions.

2.2.4 LSTM Training

In the present work, we trained a neural network to predict the extracted activation signals based on shoulder kinematics. As both sets of data are time-series signals, it is necessary to use an ANN that suitably processes the time-series or sequential data. Different ANN architectures have been employed in various studies to determine inter-joint coordination during human arm movements. The authors in [53] used a radial basis function network (RBFN)-based neural network, whereas [54] used a time-delayed adaptive neural network (TDANN) to estimate the distal joint angles. In this study, we used LSTM, a particular type of RNN capable of handling long-term dependencies. LSTMs have internal mechanisms called gates that regulate the flow of information to handle the vanishing gradient problem in RNNs, thus making them very suitable for multivariate time-series forecasting.

We used python's machine learning library, Keras, to implement the LSTM model. There are various parameters in the neural network, and the estimation accuracy may change depending on the settings of these parameters. Therefore, we first tested the learning efficiency and estimation accuracy of the LSTM model by varying the parameters, such as the batch input size, number of LSTM hidden layers, number of nodes in each layer, and number of training epochs. These parameters affect the learning and estimation efficiencies of the model. The batch size controls the number of samples shown to the network before the weight updates are applied. If the input batch size is large, the model can quickly process the entire training dataset; however, it can overlook certain features during training that might be crucial to learning.

On the other hand, we can increase the complexity and expressiveness of the model by optimizing the number of LSTM hidden layers and the number of neurons in each layer. Even in the case of using only a single hidden layer, the LSTM model can learn the characteristics of the time-series data. The efficiency can be improved by stacking multiple layers. However, if the model is made more complex than necessary, the training may not be effective. Similarly, if we increase the number of nodes, the model requires more time for learning with no significant change in

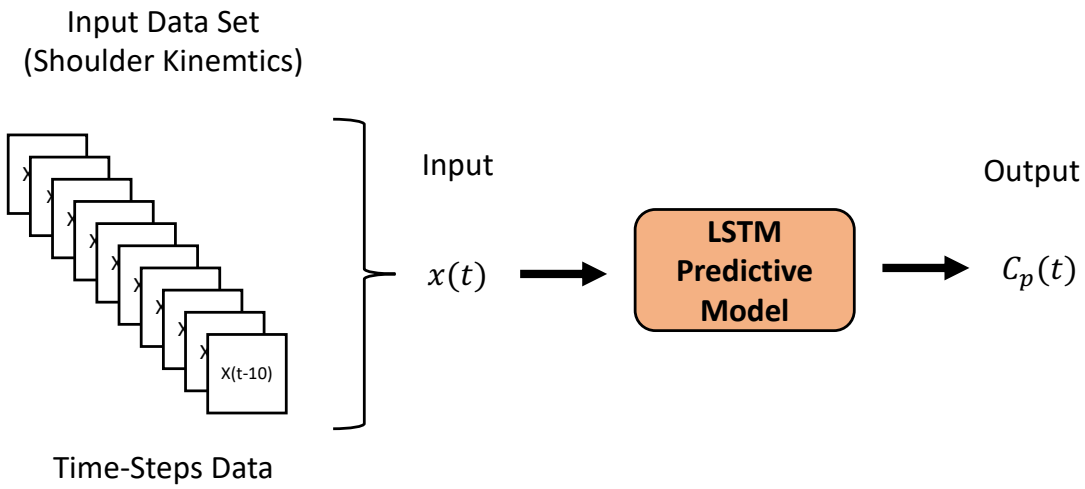

Figure 2.6: Input dataset creation: 10 previous time-steps data are combined and provided as the input $x(t)$ to the LSTM model to predict the output $C_p(t)$ at the current time step t.

accuracy. The same is also true for the number of training epochs. Estimating the time-varying activation signals is classified as a regression problem, so we use the mean squared error (MSE) as the loss function and Adam as the optimization function, as has been widely used in similar studies.

Lastly, to avoid the overfitting problem, a dropout rate of 10% is used in each layer, whereby 10% of the neurons are dropped randomly. Supervised learning is then carried out, where the neural network develops the regression model based on the input–output pairs. As for the training data, at a single time step, we can apply a total of six inputs to the model: the $SH\theta_x$, $SH\theta_y$, and $SH\theta_z$ angle of the shoulder joint and their respective derivatives $SH\dot{\theta}_x$, $SH\dot{\theta}_y$, and $SH\dot{\theta}_z$ (i.e., shoulder joint angular velocities). It is also possible to input multiple time-step data to the LSTM model at a time using the last few time-step data to predict the output for the current time step. This can improve the estimation accuracy at the cost of increasing calculations. We used the ten previous time-step data as inputs to the model (Figure 2.6). The model outputs were the activation signals, which in the case of two synergies are $C1_p$ and $C2_p$.

2.2.5 Analysis Strategy

In the present work, we compared the performances of the synergy-space neural network approach, where the shoulder kinematics are mapped to synergistic activation signals, with the direct estimation approach, wherein the neural network is used to map the shoulder kinematics to the forearm kinematics. To thoroughly investigate this comparison, we devised a comprehensive strategy to train and test 36 different LSTM models for each subject and analyze the performances. The devised strategy was based on the following criteria.

Learning Methodology

First, we devised a scenario based on our proposed learning methodology for the LSTM model. This defines the approach chosen for training the network, that is, either synergy-space or direct estimation. Three strategies were devised based on the number of synergistic components used and the learning approach.

- Synergy-Space estimation using 2 synergies components:
  In this case, we first extract the synergies W and their corresponding activation signals C from the reaching motion data considering five DOFs of the arm, i.e., $SH\theta_x$, $SH\theta_y$, $SH\theta_z$, $FA\theta_x$, and $FA\theta_y$. Subsequently, we train the LSTM model to predict two activation signals $C1$ and $C2$ based on the shoulder kinematics provided as inputs. The predicted activation signals $C1_p$ and $C2_p$ are then used along with the synergy matrix W to estimate the required forearm motions.

- Synergy-space estimation using 1 synergy component:
  In this case, we extracted the synergies W and their corresponding activation signals C from the reaching motion data considering only two DOFs of the forearm, i.e., $FA\theta_x$ and $FA\theta_y$. We then trained the LSTM model to predict only one of the activation signals $C1$, providing the shoulder kinematics as the input. Finally, the predicted activation signal $C1_p$ and the synergy matrix W are used to estimate the required forearm motions.

- Direct estimation:
  For direct estimation, no prior information or synergistic components are extracted from the reaching motion data recorded during arm movements. The LSTM model is directly trained to predict $FA\theta_x$ and $FA\theta_y$ angles of the elbow joint based on the input shoulder kinematics.

Number of LSTM Hidden Layers

As noted previously, a single layer of LSTM can learn the necessary features of the time-series data. By stacking multiple layers of LSTMs, this ability can be enhanced. Thus, to verify the appropriate number of hidden layers for our task, we tested three scenarios with varying numbers of hidden LSTM layers in our model. For each learning methodology mentioned earlier, we constructed and trained three different models, namely M1, M2, and M3, having one, two, and three hidden LSTM layers, respectively.

Number of Inputs

As previously mentioned, we can apply a total of six inputs to our model, represented by $SH\theta_x$, $SH\theta_y$, $SH\theta_z$, $SH\dot{\theta}_x$, $SH\dot{\theta}_y$, and $SH\dot{\theta}_z$. However, various combinations of these signals can also be used as inputs. This consideration was based on the fact that the level of residual limb movement control would vary for the user depending on the severity of the amputation. In addition, wearing a prosthetic socket can limit the range and types of movements the user can perform. In many cases, the shoulder internal rotation motion is the most difficult to perform for amputees. The other reason was to test whether there is any advantage to using shoulder joint angular velocities as the inputs. We created four different training scenarios with different numbers of inputs to the LSTM models. The combined and total numbers of inputs for each scenario are shown in Table 2.1.

Table 2.1: Training Scenarios based on No. of Inputs.

No. of Inputs	**Signal Combination**					
	$\boldsymbol{SH\theta_x}$	$\boldsymbol{SH\theta_y}$	$\boldsymbol{SH\theta_z}$	$\boldsymbol{SH\dot{\theta}_x}$	$\boldsymbol{SH\dot{\theta}_y}$	$\boldsymbol{SH\dot{\theta}_z}$
2		✓	✓			
3	✓	✓	✓			
4		✓	✓		✓	✓
6	✓	✓	✓	✓	✓	✓

Note: ✓cell means signal used as input

2.2.6 Evaluation

Root Mean Squared Error (RMSE)

For the evaluation of the trained LSTM model, the estimated forearm orientation angles (i.e., pronation–supination $FA\theta_x$ and flexion–extension $FA\theta_y$ angles of the elbow joint) were compared to the actual forearm orientation angles captured using the neuron pro system. Figure 2.7 presents a sample of the continuous signal plot comparing the actual vs. estimated forearm motions during one of the scenarios tested for subject 5. To assess the performance of the joint angle estimations, the standard metric used is the root mean squared error (RMSE) [54] as given in Equation (2.2.2), where $\hat{x}_t$ is the predicted joint angle, x_t is the actual joint angle at data point t, and N is the total number of data points.

To calculate the RMSE value, we used the "mean_squared_error" metric from the scikit-learn library for python and applied the square root. In the case of multiple outputs, this metric gives an average value of the RMSE.

$$\text{RMSE} = \sqrt{\frac{1}{N}\sum_{t=0}^{N}(\hat{x}_t - x_t)^2} \tag{2.2.2}$$

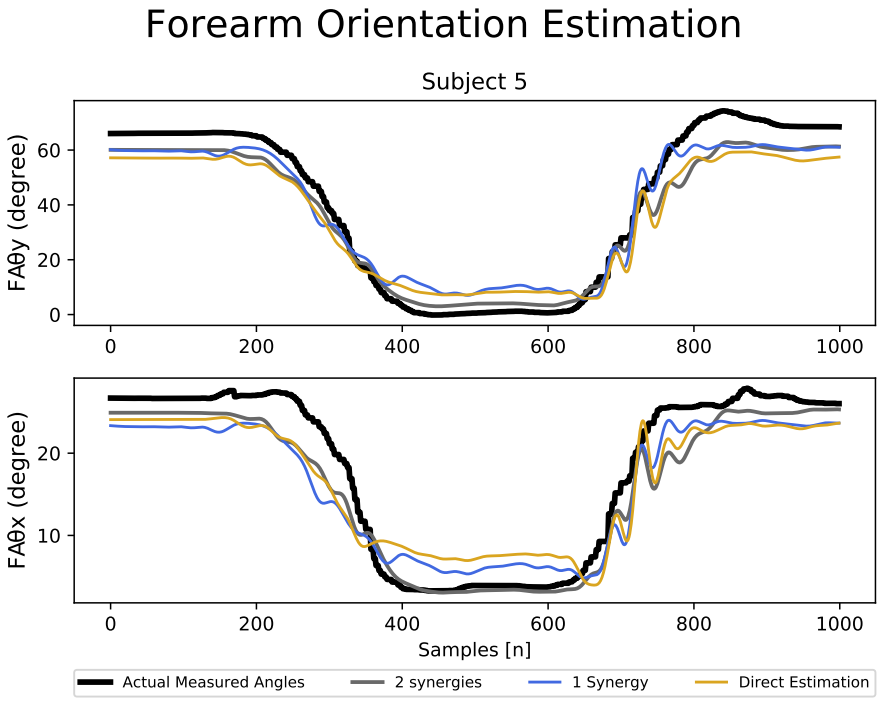

Figure 2.7: Sample of the joint angular value plots of the actual vs. estimated forearm motions using two synergies, one synergy, and direct estimation learning methodologies for one of the tested scenarios of subject 5.

Pearson Correlation Coefficient

Pearson's correlation method analyzes the linear relationship between two variables and provides a coefficient value as a measure of the correlation strength. The Pearson correlation coefficient is denoted by r and can have a value between $+1$ and -1. Table 2.2 presents the detailed interpretation of the Pearson correlation coefficient.

Table 2.2: Interpretation of Pearson Correlation Coefficient.

Range of r	**Degree of Relationship**
$-1.0 \leq r \leq -0.7$	A strong negative linear relationship
$-0.7 \leq r \leq -0.3$	A distinct negative linear relationship
$-0.3 \leq r \leq -0.1$	A weak negative linear relationship
$-0.1 \leq r \leq +0.1$	Not a linear relationship
$+0.1 \leq r \leq +0.3$	A weak positive linear relationship
$+0.3 \leq r \leq +0.7$	A distinct positive linear relationship
$+0.7 \leq r \leq +1.0$	A strong positive linear relationship

We used the "corrcoef" function from python's NumPy library, which uses the actual and estimated values of forearm orientation angles (as in Figure 2.7) to compute the Pearson correlation coefficient.

Analysis of Variance (ANOVA) Test

To statistically verify the differences between the results obtained using the synergy-space neural network and direct estimation methods, we performed the analysis of variance (ANOVA) test. The ANOVA compares three or more populations to ascertain whether the variability between group means is larger than the variability in the observations within the groups. A significance level or threshold is chosen, and a p-value less than the threshold is interpreted as evidence of the difference between the population means. In this study, the p-value indicates significant differences between the learning strategies' results.

To show the pertinence of each learning methodology, we perform the ANOVA test using the RMSE values obtained by comparing the estimated and actual forearm motions for the various LSTM models trained using the synergy-space and direct estimation approaches. We chose a significance level of 0.05, one of the standard choices. Suppose the calculated p-value is less than the threshold. In that case, the statistically significant ANOVA is followed up with the Tukey HSD (honest significant difference), a post hoc test pinpointing which learning methodology exhibits a statistically significant difference.

Cross-Subject Analysis

As discussed previously, one of the characteristics of the synergies is that they are shared among similar tasks to some extent. This suggests that a generalized or transferable control model can be developed based on the synergy-space neural network approach using the data recorded from healthy subjects. Therefore, cross-subject testing was performed to test this assumption for the robustness of the learning methodologies.

For the case of the synergy-space method, we performed the cross-subject analysis using, for example, subject A's input data fed to the LSTM models trained using the other subjects' data and then employing subject A's synergy matrix for the forearm motion prediction. However, for the case of the direct estimation method, the cross-subject analysis was performed using, for example, subject A's input data fed to the LSTM models trained using the other subjects' data for subject A's forearm motion prediction.

The evaluations were performed by calculating the RMSE values to compare the estimated motions with the actual measured values. For the cross-subject analysis, we used model M2 with six inputs (i.e., best-case scenario) and model M2 with two inputs (i.e., worst-case scenario). The ANOVA was then performed to statistically verify the difference between the cross-subject results based on the synergy-space and direct estimation approaches.

2.3 Experimental Results

In this study, we trained and evaluated 36 different LSTM models for each of the 14 subjects. The training strategy was devised based on three different learning methodologies. We constructed 3 separate LSTM models and trained each model using 4 different combinations of the input signals (i.e., $3 \times 3 \times 4 = 36$).

The acquired RMSE values of the estimated forearm motions ($FA\theta_x$ and $FA\theta_y$) for some subjects are shown as bar plots in Figure 2.8. It was observed that, overall, there are no significant differences in the results based on the learning methodology. This suggests that even with the reduced state-space representation, the synergy-space neural network is capable of keeping the performance similar to that of the direct estimation method. However, we see notable differences when using combinations of two and three inputs, implying that shoulder internal–external rotations ($SH\theta_z$) as the input significantly increase the estimation accuracy, which is the case in all the training scenarios. On the other hand, the joint angular velocities as the inputs provided a minor increase in the accuracy, as is visible when comparing the RMSE values based on the number of inputs 2 and 4 and also 3 and 6. However, no marked differences were observed in the performance based on the number of hidden LSTM layers among the models M1, M2, and M3. These observations are valid for all the subjects included in the study.

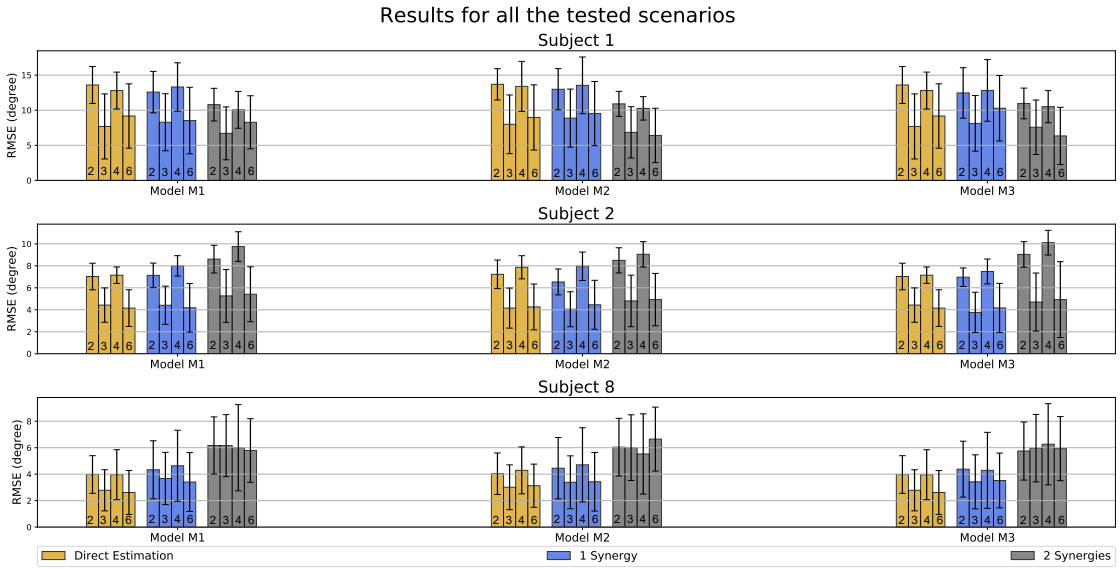

Figure 2.8: Results of the forearm motion estimations ($FA\theta_x$ and $FA\theta_y$) for all tested scenarios for subjects 1, 2, and 8, where each bar represents the calculated RMSE. The bars are first divided into M1, M2, and M3 based on the number of LSTM hidden layers in the model. The golden, blue, and gray bars represent the errors in the estimations when using two synergies, one synergy, and direct estimation learning approaches, respectively. The number inside the bar represents the number of inputs to the LSTM model (Table 2.1), whereas the error bar represents the standard deviation of estimation error values.

Regarding the minor differences for all the trained scenarios for each subject in the study, we obtained three general result types. First, similar to subject 1 (Figure 2.8), the synergy-space method (using 2 synergies) produced the lowest RMSE values with an overall RMSE and standard deviation value of 10.88° and 2.09°, respectively, for all the tested scenarios. Second, similar to subject 2 (Figure 2.8), we obtained almost similar RMSE values having some variations from an overall RMSE and standard deviation value of 7.55° and 1.16°, respectively, for all the learning methodologies. Lastly, similar to subject 8 (Figure 2.8), the direct estimation method had the lowest RMSE values with an overall RMSE and standard deviation value of 3.99° and 1.47°, respectively, for all the tested scenarios. We only selected the scenarios trained using model M2 for further analyses, i.e., with two hidden LSTM layers, as it produced the best overall results.

2.3.1 Personalized LSTM Models Evaluation

To evaluate the personalized LSTM models and compare the different learning methodologies, we used the LSTM model M2, which has two hidden LSTM layers and six inputs (Table 2.1). The average RMSE values obtained for the estimated $FA\theta_x$ and $FA\theta_y$ were 4.24° and 9.75°, 6.08° and 9.86°, and 5.84° and 7.40° for the two-synergy, one-synergy, and direct estimation methods, respectively.

We first employed Pearson's correlation coefficient to quantify the estimation performance of the different learning methodologies. Table **??** shows a mostly strong positive linear correlation ($+0.7 \leq r \geq +1.0$) for the personalized LSTM models. Furthermore, even for the few cases of a distinct or weak linear relation (highlighted cells in Table 2.3), the trend is similar for all the learning methodologies, suggesting a similar overall performance.

To show the pertinence of each learning methodology, we calculated the p-value using the ANOVA between the results of the training strategies using the RMSE values of the estimated forearm motions. The statistical ANOVA test associated with the RMSE values obtained for the three learning methodologies is reported in Table 2.4. The ANOVA provided evidence that there was no statistically significant difference, $F(2, 39) = 1.705, p = 0.195$. The summary of the ANOVA test results is shown in Table 2.5. As the p-value corresponding to the F Statistic is greater than the threshold value of 0.05, this is interpreted as there is no significant difference between the population means and eliminates the need to perform any post hoc or multiple comparison corrections test, such as the Tukey HSD. Thus, we can say that the three training strategies tend to produce similar RMSE values, and there is no significant difference between their performances for subject-specific or personalized LSTM models. This further validates that the proposed synergy-space approach for mapping the inter-joint coordination for each subject's personalized ANN models performs on par with the direct estimation method even with reduced dimensionality.

Table 2.3: Pearson's correlation coefficients "r" for Model M2 with 6 inputs.

Subject No.	Learning Methodology					
	Direct Estimation		**1 Synergy**		**2 Synergies**	
	FE	**PS**	**FE**	**PS**	**FE**	**PS**
1	0.91	0.75	0.91	0.78	0.94	0.75
2	0.95	0.89	0.92	0.89	0.96	0.90
3	0.96	0.60	0.89	0.86	0.92	0.70
4	0.96	0.71	0.91	0.70	0.97	0.71
5	0.98	0.90	0.98	0.89	0.98	0.92
6	0.97	0.83	0.93	0.76	0.95	0.84
7	0.90	0.86	0.89	0.86	0.92	0.89
8	0.97	0.38	0.93	0.67	0.96	0.51
9	0.94	0.63	0.96	0.51	0.94	0.57
10	0.91	0.31	0.92	0.29	0.88	0.34
11	0.93	0.56	0.96	0.28	0.94	0.45
12	0.98	0.80	0.98	0.83	0.97	0.81
13	0.96	0.35	0.92	0.30	0.94	0.42
14	0.96	0.70	0.92	0.57	0.95	0.65

Note: FE = flexion–extension, PS = pronation–supination. Highlighted cells mark weak correlation.

Table 2.4: Descriptive statistics of RMSE values obtained for different learning methodologies using model M2 scenarios only.

Learning Methodology	**Count**	**Sum**	**Average**	**Variance**
Direct Estimation	14	86.756	6.197	4.672
1 Synergy	14	107.930	7.709	7.335
2 Synergies	14	108.972	7.784	7.748

Table 2.5: ANOVA summary table for the results using model M2 scenarios only.

Source of Variation	**SS**	**df**	**MS**	**F Statistic**	***p*-Value**	**F Critical**
Between Methodologies	22.452	2	11.226	1.705	0.195	3.238
Within Methodology	256.826	39	6.585			
Total	279.278	41				

Note: SS = Sum of Squares, df = Degrees of Freedom, MS = Mean Square.

2.3.2 Cross-Subject Evaluation

With transhumeral amputees, the target application of this study, it is impossible to measure the elbow joint or forearm motion information. Therefore, testing the transferability of the trained predictive models is crucial.

Figure 2.9 shows a box plot summarizing the RMSE values for each subject's cross-subject evaluations using the LSTM model M2 with six inputs. The box size reflects the range where 75% of the sample values lie, with a smaller box size indicating less variation in the estimation performance. The results demonstrate that the synergy-space neural network, particularly when using two synergies, exhibits stronger robustness to inter-individual variability compared to the direct estimation method. This may be attributed to the shared nature of the synergies across simi-

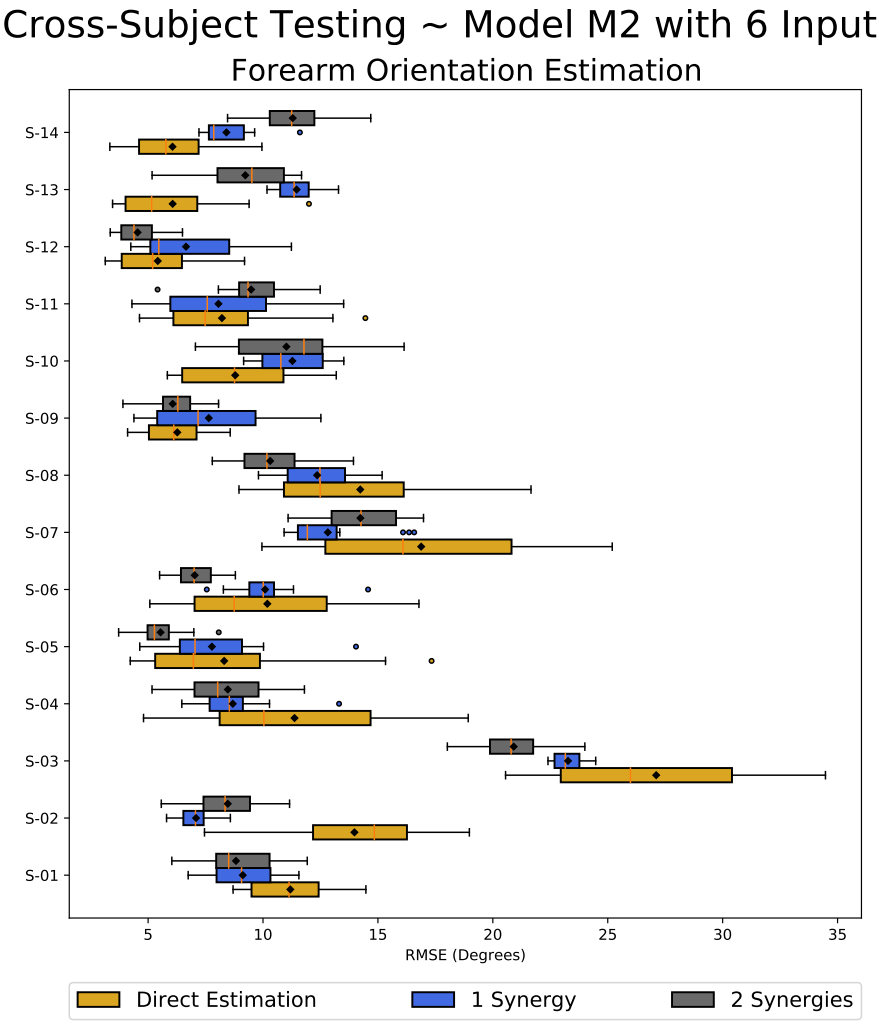

Figure 2.9: The box plot shows RMSE values for each subject's cross-subject evaluation. The box size represents the range of 75% of the values, and the solid vertical golden line inside the box represents the median, with the black diamond marker indicating the mean value. Outliers are represented by circular markers, and the whiskers show the maximum and minimum values. A smaller box size represents minor variation in results and better transferability.

Table 2.6: Descriptive statistics of the RMSE values obtained for different learning methodologies during cross-subject evaluation using model M2 with 6 inputs.

Learning Methodology	Count	Sum	Average	Variance
Direct Estimation	196	2157.122	11.006	42.696
1 Synergy	196	2025.910	10.336	19.789
2 Synergies	196	1895.985	9.673	18.365

Note: Highlighted cells mark the least values of average and variance

Table 2.7: ANOVA summary table for the cross-subject evaluation using model M2 with 6 inputs.

Source of Variation	SS	df	MS	F Statistic	p-Value	F Critical
Between Methodologies	173.962	2	86.981	3.227	0.040	3.011
Within Methodology	15765.78	585	26.950			
Total	15939.74	587				

Note: SS = Sum of Squares, df = Degrees of Freedom, MS = Mean Square.

Table 2.8: Post hoc Tukey HSD test results for the cross-subject evaluation using model M2 with 6 inputs.

Group Pair	Q Statistic	p-Value	Q Critical
Direct Estimation vs. 1 Synergy	1.805	0.411	
Direct Estimation vs. 2 Synergies	3.593	0.030	3.323
1 Synergy vs. 2 Synergies	1.788	0.418	

lar tasks and subjects, which enables the network to learn features common to the human arm's reaching task. The descriptive statistics associated with the RMSE values obtained for the cross-subject testing are reported in Table 2.6, where the proposed synergy-space RNN exhibited an average reduction of 50% in the variation in the RMSE compared to the direct estimation method (highlighted cells in Table 2.6). These results demonstrate the effectiveness of the proposed synergy-space RNN in achieving better transferability during the cross-subject evaluation.

To statistically verify whether the difference in learning methodologies affected the performance during the cross-subject evaluations, we again calculated the p-values using the ANOVA between the results using the RMSE values of the estimated forearm motions. The ANOVA yielded a statistically significant effect, $F(2, 585) = 3.227, p = 0.040$. Table 2.7 shows the summary of the ANOVA test results. As the p-value corresponding to the F Statistic is lower than the threshold value of 0.05, this suggests that the performance of one or more learning methodologies is significantly different. We further evaluated the nature of the differences between the three population means, i.e., to check which learning methodology tends to perform differently from the others.

The statistically significant ANOVA was followed-up with the Tukey HSD (honest significant difference), a post hoc test pinpointing which learning methodology exhibits a statistically significant difference. The post hoc Tukey HSD test results are reported in Table 2.8. The p-values corresponding to the Q Statistic are lower than 0.05 in the cases when comparing the direct estimation method with the synergy-space neural network approach (when using two synergies), suggesting a significant difference in the performance of the two approaches.

Similar results were also obtained for the cross-subject evaluations using the LSTM model M2 with two inputs only, presented in Tables 2.9–2.11. Even when using only two inputs (considering limited shoulder internal rotation motion (Table 2.1)) the proposed synergy-space method had about 40% less variation in the RMSE compared to the direct estimation method (highlighted cells in Table 2.9). The evaluation of the cross-subject analysis suggests that the synergy-space approach is more robust and may provide the possibility of developing a transferable model for prosthesis control.

Table 2.9: Descriptive statistics of the RMSE values obtained for different learning methodologies during cross-subject evaluation using model M2 with 2 inputs.

Learning Methodology	**Count**	**Sum**	**Average**	**Variance**
Direct Estimation	196	2792.539	14.248	41.462
1 Synergy	196	2646.628	13.503	24.561
2 Synergies	196	2440.454	12.451	23.557

Note: Highlighted cells mark the least values of average and variance

Table 2.10: ANOVA summary table for the cross-subject evaluation using model M2 with 2 inputs.

Source of Variation	**SS**	**df**	**MS**	**F Statistic**	***p*-Value**	**F Critical**
Between Methodologies	319.32	2	159.661	5.347	0.004	3.011
Within Methodology	17468.05	585	29.860			
Total	17787.37	587				

Note: SS = Sum of Squares, df = Degrees of Freedom, MS = Mean Square.

Table 2.11: Post hoc Tukey HSD test results for the cross-subject evaluation using model M2 with 2 inputs.

Group Pair	**Q Statistic**	***p*-Value**	**Q Critical**
Direct Estimation vs. 1 Synergy	1.907	0.370	
Direct Estimation vs. 2 Synergies	4.602	0.003	3.323
1 Synergy vs. 2 Synergies	2.695	0.138	

2.4 Discussion

We have proposed and evaluated the synergy-space neural network for transhumeral prosthesis control. By explicitly incorporating kinematic synergies into the model, our approach addresses the limitations of traditional ANNs and provides a more robust and superior transferability across different subjects. Our rigorous evaluation of the model has shown promising results, demonstrating its potential.

We evaluated the performance of the proposed synergy-space approach for personalized LSTM models and compared it to the direct estimation method. The results of Pearson's correlation method and the ANOVA analysis indicate that the proposed method performs comparably to the direct estimation method, with no significant difference in performance. However, the proposed approach still performs well, even with the reduction in dimensionality, suggesting its efficient and better learning capabilities for personalized LSTM models.

In the various tested scenarios, we observed that using shoulder internal–external rotations ($SH\theta_x$) as the input significantly increases the estimation accuracy of the LSTM models, which was typical for all the learning methodologies. It can be because the shoulder rotation is coupled to the forearm rotation; however, we have already extracted the kinematic synergies from the subjects' arm motion data corresponding to the five DOFs of the arm, including the shoulder and forearm rotations (i.e., $SH\theta_x$ and $FA\theta_x$). It seems not associated with the joint coordination issue and is more concerned with learning the LSTM model. An additional input (i.e., $SH\theta_x$) provides an additional parameter to the LSTM model during the supervised training/learning, and probably a more unique feature compared to using the joint angular velocities (i.e., $SH\dot{\theta}_y$ and $SH\dot{\theta}_z$). Therefore, it improves the model's accuracy.

The synergy-space approach demonstrated its superiority during the cross-subject evaluation as a more robust and transferable learning methodology. It showed more minor variations in the estimation accuracy when using one subject's motion data and extracted the synergy matrix for forearm motion estimation using the personalized LSTM models of the other thirteen subjects. However, one of the limitations of this study for the actual implementation on amputee users will be obtaining the subject-specific synergy matrix. This is because, as mentioned earlier, amputee users cannot provide the necessary motion information.

Based on the properties of synergies being repeatable and shared across similar tasks and subjects, one practical solution can be to create a generalized synergy matrix based on the data of all the able-bodied participants and use it for amputee users' forearm motion prediction. Another possibility would be to use motion data from the user's healthy arm to generate a synergy matrix for the amputated arm. As the synergy matrix represents the inter-joint coordination, the LSTM model needs to learn a simplified relation between the shoulder kinematics and the activation signals. That means effectively extracting synergies can significantly affect performance.

This first investigation of the proposed synergy-space neural network demonstrates its potential as a robust and transferable predictive model, which was successfully confirmed through the cross-subject evaluation results. This finding can contribute toward creating a synergistic and generalized control strategy for transhumeral prostheses and other rehabilitation applications.

2.5 Conclusions

The primary aim of this study was to improve the control of transhumeral prostheses, focusing on their transferability across users. A highly accurate transferable predictive model is necessary for transhumeral amputees because individual calibration or personalized learning methods cannot be used effectively as they cannot provide the required data.

In this research, we proposed the synergy-space neural networks, as a transferable model, to predict the joint angles of the forearm motion based on the residual shoulder motion. We presented the implementation and evaluation of the proposed method, discussing its learnability and robustness for transferability to amputee users. The study was conducted with able-bodied subjects, focusing on reaching movements of the arm in the horizontal plane only. We compared the synergy-space neural network approach with the direct estimation method, using the actual and estimated joint angular values for the performance evaluation. In the best-case scenario, average RMSEs of 9.75° and 4.24° were achieved using the synergy-space method (using 2 synergies) for the flexion–extension ($FA\theta_y$) and pronation–supination ($FA\theta_x$) angles of the forearm motion. Consequently, we verified that for the case of personalized predictive models, even with a reduced state space, the proposed synergy-space neural network approach produced results similar to the direct estimation method.

We investigated the transfer learning ability of the proposed model through cross-subject analysis. The results indicate that the synergy-space neural network exhibited superior learning capabilities compared to the traditional direct estimation method during cross-subject evaluations. This highlights the strength of our approach as a transferable decoder, demonstrating its ability to handle inter-individual variabilities and providing a more generalized model for transhumeral prosthesis control.

In the future, we can send the output of predicted joint angles from the proposed model to a transhumeral prosthesis for real-time control. As a next step, this approach would be extended to incorporate reaching motions in three-dimensional space. The ultimate goal in the future is to develop a framework for the real-time estimation of forearm motions to further test and improve the proposed approach, such that it can be employed on actual transhumeral prostheses that allow users to control the device intuitively.

Chapter 3

Deep Reinforcement Learning-Based Synthetic Motion Cloning

3.1 Introduction

In recent decades, significant progress has been made in the development of advanced prosthetics [11], [12] aimed at restoring lost limb function with multiple active degrees of freedom (DOF). However, despite the improvements in robotics and sensor technologies, there is a growing gap between control methods and hardware improvements, resulting in a rejection rate as high as 40% [71]. This disparity becomes even more pronounced in the case of transhumeral amputees.

The lack of intuitive controllability remains a primary challenge in enabling transhumeral amputees to control a multi-functional prosthesis, which includes a powered hand, wrist, and elbow, replicating various functions of a human arm. A significant control objective is the execution of elbow joint motion and wrist pronation–supination during target reaching tasks. Currently, commercially available prosthetic elbows are controlled through electromyographic (EMG) signals, which results in complex control schemes and the development of compensatory strategies involving large trunk and shoulder displacements [72]. However, the myoelectric control strategy lacks intuitiveness since the physiologically appropriate muscles are unavailable, necessitating highly invasive surgeries such as targeted muscle reinnervation (TMR) to overcome these limitations [73]. Furthermore, an analysis of the manipulation strategies employed by prosthetic users [74] suggests that body-powered devices tend to offer more intuitive control compared to myoelectric devices. It has been observed that myoelectric devices often make routine tasks more cumbersome and time-consuming to perform [75]. As an alternative, bio-inspired and human motor-control-based techniques have been developed to achieve more natural control of multiple DOFs [23], [76].

Recent studies have focused on enhancing the intuitive control of prosthetic elbow joints by leveraging movement synergies that govern coordinated joint movements in the upper limb [77]–[79]. Previous studies have revealed that human movements can be effectively characterized by a reduced set of primitive components known as motor synergies [37], [80]. It has also been observed that similar movements performed by different individuals exhibit *shared synergies*, indicating the reusability of motor synergy patterns [81], [82]. Researchers in [83] have successfully demonstrated the generalization ability of movement synergies for new targets in multi-directional scenarios.

Building upon this concept, recent studies such as [31], [84] have showcased the effectiveness of controlling wrist pronation–supination and elbow flexion–extension through remaining shoulder movements, which participants have found intuitive. This approach combines the residual limb motion strategy with the predictive capabilities of ANNs, harnessing the inherent movement synergies between the shoulder and elbow joints. As a result, it enables independent and simultaneous control of the multi-DOF prosthesis. In particular, radial basis function network (RBFN) models have proven effective in capturing intricate inter-joint coordination patterns in various ADLs [53], [85]. Additionally, ANNs and fuzzy logic methodologies have been successfully applied for classifying and predicting prosthetic arm motions [86]. Moreover, the combination of EMG and shoulder orientation data has also been explored to estimate distal arm joint angles [54].

However, one of the crucial challenges associated with this strategy revolves around the acquisition of a sufficient amount of training data from human experiments, as this approach relies on ANNs to identify and model the intricate coordination between the shoulder and elbow joints. This necessitates providing extensive training data to the network during the learning process. Obtaining such training data involves expensive motion capture equipment and a lengthy, repetitive process where subjects perform numerous repetitions of the desired ADLs. The quantity and quality of the motion data obtained also significantly impact the performance of the ANN, as there are certain levels of motion variations among different human subjects.

This study presents an innovative motion-cloning strategy to address the challenge of acquiring a substantial amount of training data for effective training of ANN. Our approach leverages the capabilities of DRL algorithms to create natural and human-like motion in simulated humanoid agents [87]. We introduce a DRL-based motion cloning framework that utilizes a 7-DOF robot arm model in a mujoco simulation to generate synthetic motion data. Furthermore, we explored the use of the synthetic motion data obtained from DRL simulation (hereafter referred to as DRL-Data) to train different ANNs and demonstrate the effectiveness of DRL-Data in accurately estimating the arm motion of human subjects by comparing it with their actual motion data (hereafter referred to as Real-Data). Moreover, the integration of Real-Data and DRL-Data through motion data augmentation demonstrated the enhanced robustness of the trained ANNs. This approach addresses the challenge of limited motion data availability by supplementing and diversifying the training data, thereby improving the ANN's ability to generalize across different subjects.

The fundamental concept behind the proposed framework is that the simulated robot arm has the ability to learn and replicate a wide range of desired movements. We can utilize the extracted motion data from the shoulder and elbow joints from the simulated arm to effectively supplement and diversify the training data for the ANN. To the best of our knowledge, our study represents the first successful demonstration of employing learning–synthetic motion data to estimate actual human arm movements.

This paper is organized as follows. Section 3.2 presents our proposed framework, including details of the experimental protocols and the implementation of DRL simulation. The ANN training strategy and the method employed for performance evaluation are also described in this section. The results are presented in Section 3.3 and discussed in Section 3.4. Finally, we draw conclusions and discuss future works in Section 3.5.

3.2 Materials and Methods

3.2.1 Experiment Protocols

This study focuses on estimating the elbow joint motion and wrist pronation–supination during arm reaching movements, spanning across multiple directions in the horizontal planes. We designed our experiment by drawing inspiration from the investigation carried out in [37], which explored arm reaching movements towards target points arranged in a circular manner. We created a target grid consisting of eight points positioned along the circumference of a circle with a diameter of 0.5 m, as depicted in Figure 3.1a.

The experimental task involves a reaching movement starting from a resting position at the center point, then reaching and touching the selected outer target point, and finally returning to the center point. A brief pause at the center point precedes the repetition of the process to reach the next target. This movement task is referred to as the center-out-center reaching task. Throughout the experiments, the participants were instructed to perform center-out-center reaching movements towards all eight target points within the horizontal plane, as illustrated in Figure 3.1b.

3.2.2 Human Subject Motion Data Acquisition: Real-Data

Six right-handed individuals (five males and one female) with no known upper limb neuromuscular disorders volunteered as participants for this study. The age range of the subjects was between 20 and 28 years old. Before the experiment, all participants provided informed consent to participate in the research.

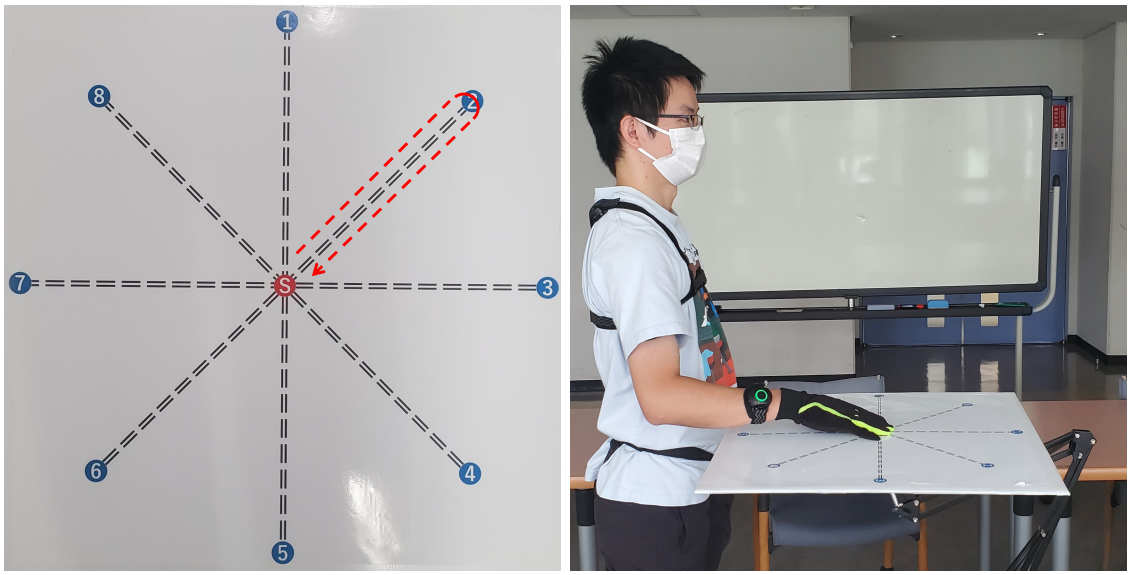

(a) (b)

Figure 3.1: The designed experimental protocol for arm reaching movements in the horizontal plane: (**a**) The target points are arranged in a circular pattern. The center point (red) represents the initial neutral/rest position, and the outer points (blue) numbered 1 to 8 indicate the target points to be reached. The arrow depicts the outline of the desired center-out-center reaching movement to be performed. (**b**) An illustration of a subject with the target grid in the horizontal plane, demonstrating the positions of the target points relative to the participant.

To acquire arm motion data from the participants, we implemented an experimental setup as depicted in Figure 3.2. The participants were instructed to execute center-out-center reaching movements with their right arm while standing. A number was displayed on a screen in front of the subjects, indicating the specific target point to be reached (Figure 3.2a). The timing of the movements was controlled passively through automatic color changes at fixed intervals. The green color indicated the start of the reaching movement towards the outer target point, and it remained green for 2 seconds. A display of red color indicated the return to the center point and the waiting phase, as it remained red for 5 seconds. The process was repeated for the next movement once the color turned green again.

We employed neuron pro, an inertial measurement unit (IMU)-sensor-based full-body motion capture system, to capture the participants' motion data. While this system's accuracy may be lower than that of optical-camera-based motion capture systems, it offers the advantage of capturing motions without spatial constraints from any location within the device's communicable range. The neuron pro system includes the axis neuron pro software (Figure 3.2b), which processes raw IMU data and generates a real-time 3D skeletal model. This skeletal model provides valuable motion information, including the position and angle of each joint, which can be saved for further analysis.

The participants were instructed to perform only four repetitions of the center-out-center reaching movements for each target point, resulting in a relatively small amount of collected data. We conducted the experiment twice per subject, recording two sets of motion data, one each for training and testing purposes. The motion data of interest included the angles of the right arm's 3-DOF shoulder joint (rotation ($S\theta_x$), flexion ($S\theta_y$)), and abduction ($S\theta_z$) and 2-DOF elbow joint (pronation ($E\theta_x$) and flexion ($E\theta_y$)) during the reaching movements toward the targets. These joint angles were saved and utilized for cross-validation testing of the trained ANNs to assess the effectiveness of the DRL-Data approach.

(a)

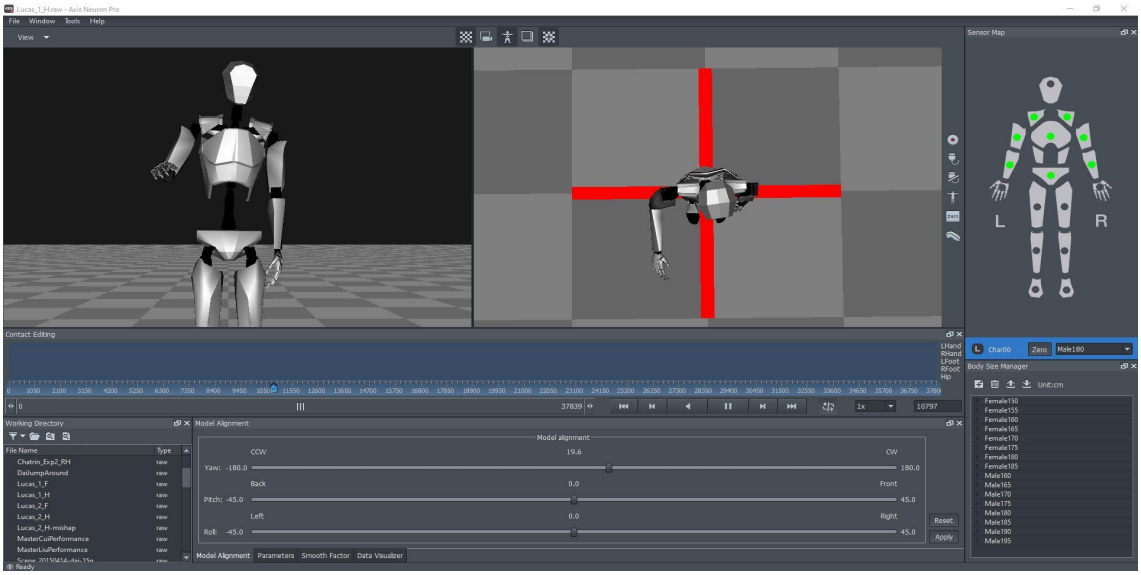

(b)

Figure 3.2: Experimental setup for capturing arm reaching motion data from human subjects. (**a**) A human subject wearing the neuron pro motion capture system and performing the reaching motion on the target grid in the horizontal plane, with the desired target point projected on the front screen. (**b**) Illustration of axis neuron pro software with a real-time 3D model.

3.2.3 Deep Reinforcement Learning (DRL)-Based Motion Cloning: DRL-Data

The model-based approach, which involves mathematical optimization for addressing high-dimensional or redundancy problems in robotics, requires prior knowledge of robot dynamics and the operating environment. In contrast, DRL presents a promising model-free strategy that learns an effective policy through iterative trial-and-error interactions with the environment without relying on dynamic parameters such as mass, inertia, or even the model itself. An essential aspect is designing a suitable reward function, as DRL algorithms enable robotic agents to learn optimal actions by maximizing cumulative rewards within their virtual environment. In a related study [40], quantitative evidence was provided to demonstrate that deep learning, like humans, also exhibits motor synergy, enabling robotic agents to achieve energetically efficient and natural human-like motion.

To generate synthetic motion data according to the predefined experimental protocols, we utilized MuJoCo [88], a widely used simulation engine in the DRL research community for studying multi-joint mechanical systems. We created an anthropomorphic 7-DOF robotic arm agent consisting of three sequentially connected modules: a 3-DOF shoulder joint with abduction, flexion, and rotation, a 2-DOF elbow joint with flexion and pronation, and a 2-DOF wrist joint with abduction and flexion, mimicking a human arm's configuration. This arrangement, depicted in Figure 3.3a, replicates the total DOFs of a real human arm, considering the forearm's axial rotation as part of the elbow joint articulation along with elbow bending. The arm's endpoint is positioned at the fingertip of the middle finger.

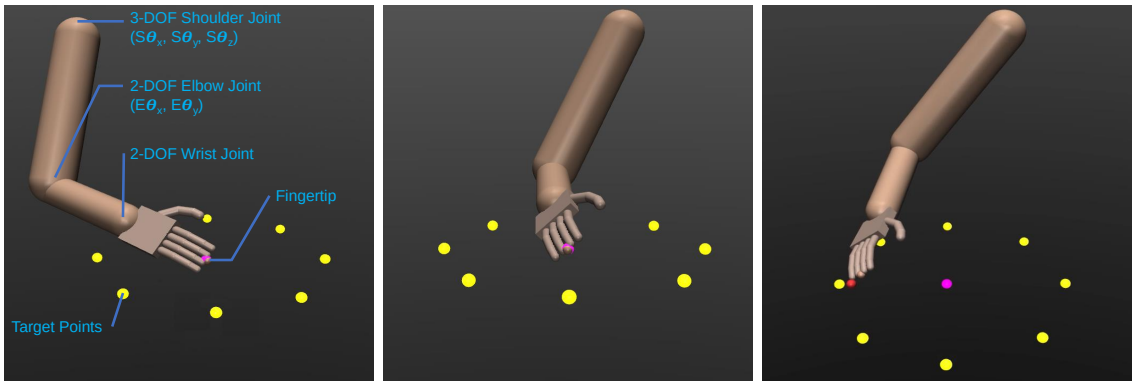

(a) (b) (c)

Figure 3.3: The simulated anthropomorphic 7-DOF robot arm and the target points in the MuJoCo simulation environment showcasing the setup: (**a**) Isometric view of the simulated robot arm with the joints and a description of the DOFs. (**b**) The simulated robot arm in a neutral pose, with target points arranged horizontally. (**c**) The simulated robot arm tracking a moving point (red) to reach and touch a designated target point (yellow).

Our study utilizes the advanced soft actor–critic (SAC) algorithm [59] for synthetic motion generation. In the DRL domain, tasks are typically represented as infinite-horizon Markov decision processes (MDP), characterized by the tuple $(\mathcal{S}, \mathcal{A}, p, r)$. Here, $\mathcal{S}$ denotes the continuous state space, $\mathcal{A}$ represents the possible action space, and $p : \mathcal{S} \times \mathcal{A} \times \mathcal{S} \rightarrow [0, \infty)$ defines the probability density of transitioning from the current state $\boldsymbol{s}_t \in \mathcal{S}$ to the next state $\boldsymbol{s}_{t+1} \in \mathcal{S}$ given the action $\boldsymbol{a}_t \in \mathcal{A}$. Additionally, $r : \mathcal{S} \times \mathcal{A} \rightarrow \mathbb{R}$ is the reward function, providing a scalar reward at each transition. The trajectory distribution induced by a policy $\pi(\boldsymbol{a}_t|\boldsymbol{s}_t)$ is denoted by ρ_π. The SAC algorithm is a cutting-edge stochastic DRL technique that learns a policy $\pi(\boldsymbol{a}_t|\boldsymbol{s}_t)$ aiming to maximize not only the rewards but also the expected entropy $E_{\rho_\pi}[H(\pi(\cdot|s_t))]$, weighted by an entropy term α as expressed in Equation (3.2.1). This maximization of expected entropy enhances the exploration of diverse behaviors during training, accelerating learning and significantly reducing sub-optimal solutions.

$$\pi_{SAC} = E_{(s_t,a_t)\sim\rho_\pi}[r(s_t, a_t) + \alpha \cdot H(\pi(\cdot|s_t))] \tag{3.2.1}$$

To make the 7-DOF robot arm learn the reaching motion toward the target points, it is assigned a task to track and follow a moving point. The trajectory of the moving point adheres to the prescribed center-out-center reaching task outlined in the experimental protocols. Starting at the center point, the moving point commences a linear movement towards a designated target in yellow (Figure 3.3b), aiming to reach and touch it, followed by a return to the center point. A brief pause occurs at the center point before the moving point transitions to the next target, ensuring that all eight target points are periodically reached during the training phase. Utilizing the SAC algorithm, the policy is learned to enable the robot arm's endpoint (the fingertip of the middle finger) to accurately track the moving target (as depicted in Figure 3.3c). The objective is to minimize the position error between the endpoint and the moving target in the task space while ensuring energy-efficient motion.

The reward function used during training is defined as in Equation (3.2.2) and has three terms with constant coefficients b, c, and d carefully chosen through experimentation to maximize performance potential. The position error $error_p$ quantifies the distance between the moving point's position and the current fingertip position computed from the state. This component enables the robot arm to effectively learn the center-out-center reaching motion. The $\|.\|$ notation represents the Euclidean Norm and captures the total energy cost associated with each action a_t. By minimizing this term, the robot arm is encouraged to optimize energy usage, generating synergistic motion that closely resembles human-like behavior. Furthermore, the palm orientation error "$error_o$" ensures proper palm orientation during the reaching motion, aligning with the observations made during the human motion data acquisition experiments, where the palm of the hand consistently faced downwards.

$$r\left(\boldsymbol{s}_t, \boldsymbol{a}_t\right) = -b \cdot error_p - c \cdot \left\|\boldsymbol{a}_t\right\|^2 - d \cdot error_o \tag{3.2.2}$$

The training involved learning the reaching movements towards the target points in the horizontal plane over 200,000 steps. Upon completion, the robot arm's learned motion was simulated within the MuJoCo environment, where it successfully executed the center-out-center reaching tasks for all target points. Subsequently, synthetic motion data were extracted from the robot arm during the target reaching movements, comprising 3-DOF shoulder joint angles (i.e., rotation, flexion, and abduction) and 2-DOF elbow joint angles (i.e., pronation and flexion). These joint angles are hereafter referred to as $S\theta_x$, $S\theta_y$, $S\theta_z$, $E\theta_x$ and $E\theta_y$, respectively, constituting our motion dataset. We acquired the DRL-Data containing four repetitions of reaching movements per target point, later used as the training dataset for the ANNs.

3.2.4 Convolutional Long Short-Term Memory (CNN-LSTM) Neural Network

This study employed convolutional long short-term memory (CNN-LSTM) neural networks to train a neural network model capable of recognizing shoulder–elbow coordination and predicting elbow joint angles based on shoulder kinematics input. The CNN-LSTM architecture combines the strengths of both convolutional neural networks (CNNs) and long short-term memory (LSTM) recurrent neural networks (RNNs), which have shown promising results in various time series prediction or classification tasks. Recent studies, such as human activity recognition in [89], have explored combining CNN and LSTM layers to enhance performance. This combination is motivated by the idea that LSTM's performance can be limited by the quality of the input features it receives [90]. We improve the overall feature representation by incorporating CNN layers, which are adept at reducing input frequency variance and extracting meaningful features. The LSTM layers then capture temporal dependencies within the extracted features. Additionally, our approach integrates CNN and LSTM layers within a unified architecture, allowing optimized training for all layers.

We utilized Python's machine learning library, Keras, to implement our CNN-LSTM model. Following the methodology outlined in [53], our CNN-LSTM network was trained to establish the relationship between shoulder and elbow joint angles during target reaching movements. The training process involved supervised learning, where the CNN-LSTM developed a regression model using input–output pairs. Specifically, the CNN-LSTM received the shoulder joint angles ($S\theta_x$, $S\theta_y$ and $S\theta_z$) as input and was trained to predict the corresponding elbow joint angles ($E\theta_x$ and $E\theta_y$).

To achieve high prediction accuracy, we fine-tuned the hyperparameters of the CNN-LSTM network, including the number of nodes and hidden layers. We found that a CNN-LSTM network with a single one-dimensional CNN layer, two LSTM layers, each containing 256 nodes, and a final dense layer along with the Adam optimization function yielded efficient results (Figure 3.4). This configuration allowed the network to effectively capture features from the input data and model the temporal dependencies necessary for accurate estimation.

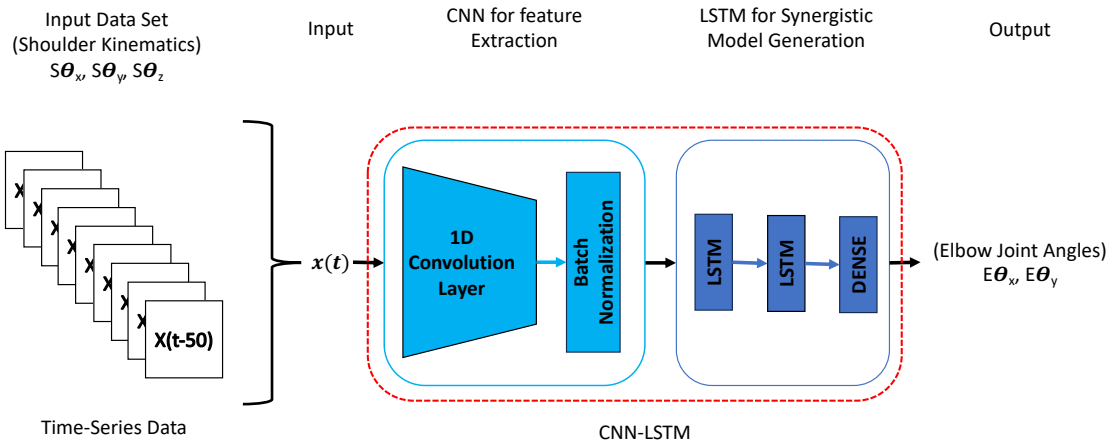

Figure 3.4: CNN-LSTM model architecture.

3.2.5 Analysis Strategy

To assess the effectiveness of the DRL-Data, we trained various CNN-LSTM models using different input data configurations. In particular, we tested two different scenarios:

Sufficient Human Motion Data Availability

In the first scenario, we evaluated how well the DRL-Data could be used for predicting the elbow joint motion of a human arm during reaching movements across different subjects. We developed two CNN-LSTM models for performance comparison: the *DRL-Model* and the *Human-Avg-Model*. The *Human-Avg-Model* was trained using an averaged motion dataset from five human subjects, making it suitable for the sufficient data scenario. On the other hand, the *DRL-Model* was solely trained on synthetic motion data. We then evaluated the performance of both models using a new motion dataset from a sixth subject. Below are the details of the trained CNN-LSTM models:

- *DRL-Model:*
  DRL-Model was trained with synthetic motion data generated from a DRL simulation without using any human joint angle information. Its purpose was to evaluate how well the decoder based only on DRL-Data could predict elbow joint motion in human arms during reaching movements across different subjects.

- *Human-Avg-Model:*
  Six distinct *Human-Avg-Models* were trained using averaged motion data obtained by combining the motion data from five human subjects. Each *Human-Avg-Model* excluded the motion data from one of the six subjects, which was later utilized for testing the model. These *Human-Avg-Models* served as the gold standard for performance comparison given that the pre-

dictive model trained using motion data from multiple human subjects' can capture typical features of human reaching motion from Real-Data.

- *Performance Assessment:*
  The efficacy of the trained CNN-LSTM models (*DRL-Model* and *Human-Avg-Model*) was tested using real motion data captured via the neuron pro motion capture system. For example, to validate the *Human-Avg-Model*, which was trained on averaged motion data from subjects two to six (S2–S6), subject one's (S1) motion data were employed. Subsequently, subject one's (S1) motion data were also used to test the *DRL-Model*. For comprehensive performance evaluation, the predicted elbow joint motion angles from both CNN-LSTM models were compared with the original elbow joint motion data of subject one (S1) and quantified using the root mean squared error ($RMSE$) (Section 3.2.6), a key metric for performance assessment. This iterative testing procedure was replicated using the motion data of each subject to ensure thorough performance evaluation across multiple subjects.

Limited Human Motion Data Availability

In the second scenario, we focused on exploring the potential enhancement of performance and efficiency in a CNN-LSTM model through motion data augmentation by the integration of DRL-Data with Real-Data. For comparison purposes, we trained two types of CNN-LSTM models: the *Hybrid-Model* and the *Human-Sparse-Model*. This scenario is considered a limited data scenario as we utilized motion data from a single human subject with a constraint. To elaborate, for training the *Human-Sparse-Model*, the motion data comprised one repetition of reaching movements towards only four out of the eight target points (specifically, target points 1, 3, 5, and 7).

Conversely, the *Hybrid-Model* was trained using an augmented motion dataset. We combined the motion data from the same human subject as before and enriched it with DRL-Data consisting of reaching movements towards an additional set of four target points (target points 2, 4, 6, and 8), thereby diversifying the training dataset.

To comprehensively assess the performance of both CNN-LSTM models, we evaluated their ability to predict reaching motions towards all eight target points utilizing new motion data from five different subjects, employing a cross-subject evaluation strategy. Details of the trained CNN-LSTM models are as follows:

- *Hybrid-Model:*
  Six distinct *Hybrid-Model*s were trained using the augmented motion dataset, which combined the motion data from only one human subject, having one repetition of reaching movements toward four target points, and the DRL-Data, with one repetition of reaching movements toward four additional target points (eight target points in total). The aim was to investigate the potential of the DRL-Data to supplement and diversify the limited training data, thereby enhancing the performance of the CNN-LSTM model.

- *Human-Sparse-Model:*
  Six separate *Human-Sparse-Model*s were trained, each using motion data from only one human subject, with the limitation of having only one repetition of reaching movements towards the specified four target points. This *Human-Sparse-Model* establishes a baseline for performance comparison and evaluation of the corresponding *Hybrid-Model*s.

- *Performance Assessment:*
  The effectiveness of the augmented motion data was assessed through a comparative analysis of the predictive capabilities of the *Hybrid-Model* and *Human-Sparse-Model*. This validation process was conducted using real motion data encompassing reaching movements toward all eight target points, employing a cross-subject methodology. To illustrate, if subject one's (S1) motion data were utilized to train the *Human-Sparse-Model* and augmented motion data from subject one (S1 + DRL) were employed for training the *Hybrid-Model*, then the performance of both models was evaluated using a cross-subject approach, involving motion data from subjects two to six (S2–S6). The root mean squared error ($RMSE$) (as described in Section 3.2.6) between the predicted and original elbow joint angular values was computed, serving as a performance assessment metric.

3.2.6 Evaluation

To evaluate the quality of the synthetic motion data and assess the performance of the CNN-LSTM models in predicting elbow joint angles, we employed well-established metrics such as Pearson's correlation coefficient and root mean squared error ($RMSE$) [52]. By utilizing Pearson's correlation coefficient, we could assess the degree of linearity between the predicted joint angles and the actual values, providing insights into the model's ability to capture the underlying synergistic patterns in the data, whereas the $RMSE$ metric enables us to gauge the overall accuracy and precision of the CNN-LSTM models' estimations.

Pearson Correlation Coefficient

Pearson's correlation method examines the linear relationship between two variables and quantifies the strength of their correlation. The resulting coefficient, denoted as *"r"*, ranges between -1 and $+1$, offering insights into the extent and direction of the correlation. Table 2.2 presents the detailed interpretation of the Pearson correlation coefficient.

To compute the Pearson correlation coefficient, we employed the "corrcoef" function available in Python's NumPy library, which uses the subject's original elbow joint angles and the CNN-LSTM estimated elbow joint angles to compute the Pearson correlation coefficient.

Root Mean Squared Error ($RMSE$)

For performance evaluation, we compared the estimated elbow joint angles (i.e., pronation–supination $E\theta_x$ and flexion–extension $E\theta_y$) with the subject's original elbow joint angles obtained during the reaching movements captured using the neuron pro system, using the root mean squared error ($RMSE$) metric as defined in the Equation (2.2.2). Here, $\hat{x}_t$ is the predicted joint angle and x_t is the actual joint angle at data point t. The total number of data points is represented by N.

Target Point Reaching Error: Unity 3D Simulation

To evaluate the accuracy of the predicted arm movements in reaching the target points, we utilized a Unity 3D simulation. This simulation was designed to animate the motion data predicted by the CNN-LSTM model. The Unity simulation replicated the setup of the human subject motion data acquisition experiment, featuring a humanoid actor in a standing position with target points arranged in the horizontal plane (as shown in Figure 3.5).

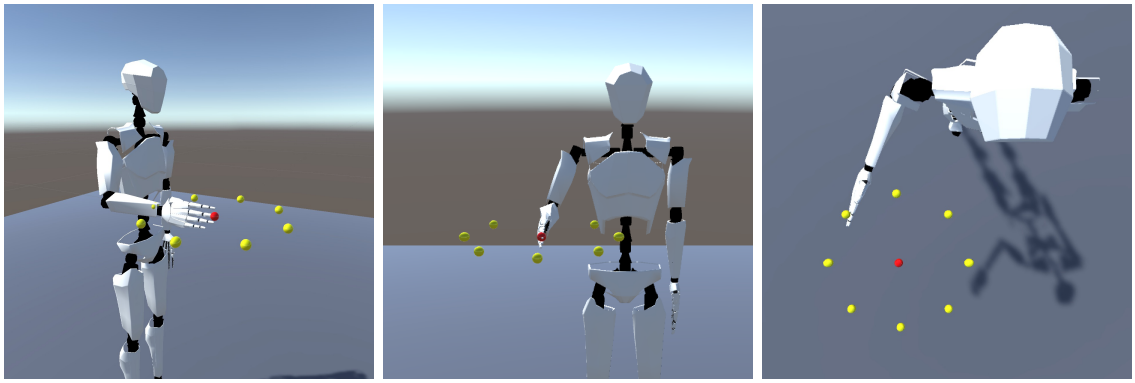

(a) (b) (c)

Figure 3.5: The Unity 3D simulated environment for estimated motion animation: (**a**) Isometric view showcasing the arrangement of target points horizontally in a circular configuration, with the humanoid actor positioned in a standing stance. (**b**) Front view of the humanoid actor in a neutral pose, with the middle finger's fingertip at the center point. (**c**) Illustration of the humanoid actor's arm reaching towards a designated target point (yellow).

The joint angles from each subject's original motion data and the corresponding predicted elbow joint angles from both the *DRL-Model* and the *Human-Avg-Model* were used for the animation. This allowed the humanoid actor to visualize the arm reaching movements toward all the target points. The target point reaching error of both the CNN-LSTM models was determined relative to the actual arm reaching movements of each human subject toward the specified target points animated in the Unity 3D simulation. The Unity-based evaluation provided valuable insights into the performance of the CNN-LSTM models through the visualization of the predicted arm reaching motions.

3.3 Results

In this section, we present the analysis results of our proposed DRL-based synthetic motion cloning approach. Firstly, we demonstrate that the generated DRL-Data accurately replicate synergistic human-like motion and exhibit joint angular movement patterns similar to those observed in human subjects during arm reaching motions. Next, we showcased the effectiveness of the *DRL-Model*, a CNN-LSTM model trained using the DRL-Data as input, in predicting the elbow joint motion of different human subjects. The *DRL-Model* achieves comparable performance to the gold-standard *Human-Avg-Model*. Most notably, our cross-subject evaluation reveals that motion data augmentation through the combination of Real-Data and DRL-Data can improve the performance of sparse CNN-LSTM models (*Hybrid-Model*) in scenarios with limited data availability.

Starting with the quality assessment of the synthetic motion data, our analysis focused on evaluating the correlation between the DRL-Data and the averaged human motion dataset from all six subjects, which served as the benchmark for this comparison. Figure 3.6 illustrates the results through a confusion matrix, presenting the Pearson's correlation coefficient obtained by comparing all of the motion datasets, including the Real-Data for each human subject and the DRL-Data.

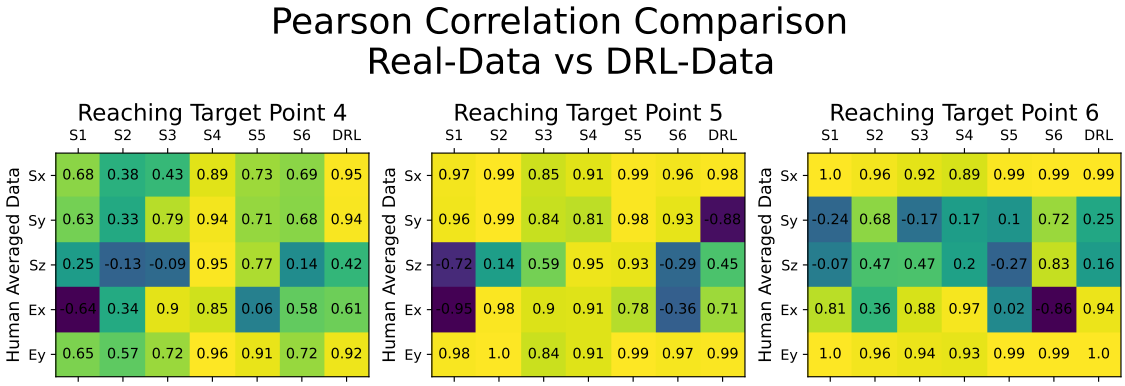

Figure 3.6: Confusion matrices illustrating the Pearson's correlation coefficients obtained by comparing the motion datasets with the averaged human motion data from all six subjects. Each confusion matrix presents Pearson's correlation comparison for reaching movements toward a specific target point. The 3-DOF shoulder and 2-DOF elbow joint angular values (Sx, Sy, Sz, Ex, and Ey) are compared. The correlation values are displayed within small boxes, with lighter colors (yellow) indicating stronger correlations and darker colors (green, purple, etc.) representing weaker correlations. The columns labeled S1 to S6 depict the comparison with motion data from each subject, while the last column (DRL) compares the generated synthetic motion data.

Figure 3.6 comprises individual confusion matrices demonstrating Pearson's correlation comparison for reaching movements towards target points, specifically the target points numbered 4, 5, and 6. The columns labeled S1 to S6 depict the comparison with motion data from each subject sequentially, while the final column presents the comparison with the generated DRL-Data. Variations in Pearson's cor-

relation values can be observed due to the subjects' inherent individual differences in reaching motion. However, the overall trend highlights the consistency among all participants and the DRL-Data, indicating a shared movement pattern. The similarity between the Pearson's coefficient values of the DRL-Data and those of any other human subject's motion data suggests that the synthetic dataset generated by our DRL-based motion cloning framework can be considered as an additional subject within the experiment.

The next step involved evaluating our framework's effectiveness in predicting elbow motion during actual human arm reaching movements. To achieve this, we utilized the synthetic motion data as the training dataset for a CNN-LSTM network called the *DRL-Model* (see Section 3.2.5). As the DRL-based motion cloning framework aimed to replicate human-like motion, we expected the performance of the *DRL-Model* to be comparable to that of the *Human-Avg-Model* (see Section 3.2.5), which was trained using the averaged human motion dataset. Although slight variations in performance were expected due to the artificially generated nature of the DRL-Data, we anticipated that it would capture the essence of reaching movement synergistic patterns to effectively train the *DRL-Model*. After training both models, we employed them to predict the elbow joint angles ($E\theta_x$ and $E\theta_y$) during reaching motions performed by actual human subjects. Their shoulder joint angles ($S\theta_x$, $S\theta_y$ and $S\theta_z$) served as input for the estimation process (see Section 3.2.4). Sub-

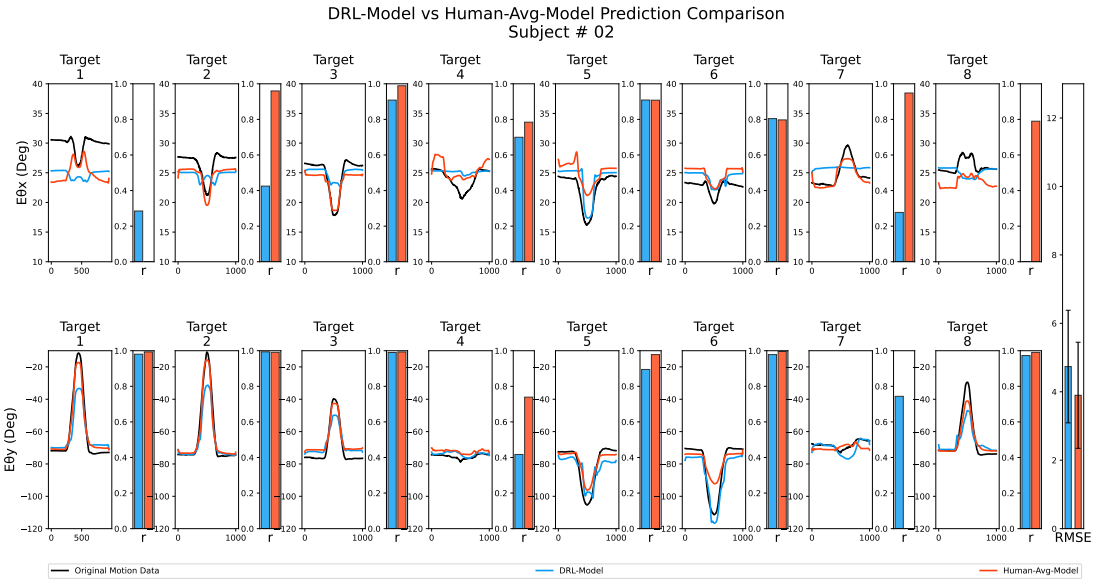

Figure 3.7: Prediction performance analysis for both the *DRL-Model* and the *Human-Avg-Model* for one of the subjects. The top row illustrates the elbow pronation–supination angle $E\theta_x$, while the bottom row represents the elbow flexion–extension angle $E\theta_y$. The line graph visually represents the joint angle variation during reaching movements toward each target point. The original joint angles are displayed in black, the *DRL-Model* estimations are shown in blue, and the *Human-Avg-Model* estimations are depicted in red. The adjacent bars correspond to Pearson's correlation coefficient values for each comparison, while the overall RMSE value is depicted in the bar graph in the last column, with the error bar representing the standard deviation of estimation error values.

sequently, the estimated elbow joint angular values were compared to the subjects' original elbow joint angular values to analyze performance.

Figure 3.7 displays the results of the prediction performance analysis for both the *DRL-Model* and the *Human-Avg-Model* for one of the subjects. The line graph illustrates the variation in the joint angles (elbow pronation–supination $E\theta_x$ and flexion–extension angle $E\theta_y$) during reaching movements towards each target point, while the adjacent bars indicate the corresponding Pearson's correlation coefficient values compared to the subject's original joint angular variation. Additionally, as depicted in the bar graph in the last column, we computed the overall RMSE value by comparing the estimated and original joint angular values for all target points along with the error bar representing the standard deviation of the estimation error values. As suggested by similar Pearson's correlation coefficient values and slight differences in overall RMSE values in Figure 3.7, both the *DRL-Model* and the *Human-Avg-Model* exhibited comparable performance.

The bar graph in Figure 3.8 presents the overall RMSE values obtained for the prediction of elbow joint motion across all six participating subjects. Since the *Human-Avg-Model* was trained using an averaged human motion dataset as input,

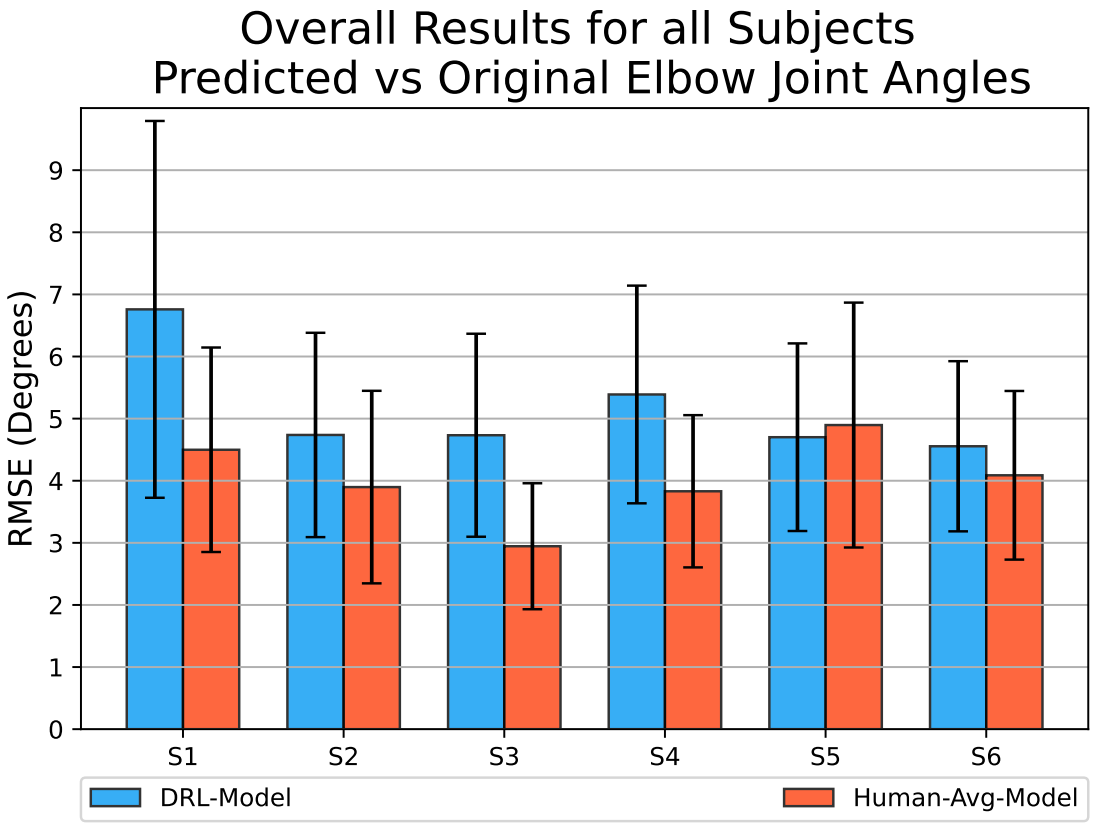

Figure 3.8: Bar graph representing the overall RMSE values obtained by comparing the estimated elbow joint angular values to the original values for reaching movements towards all target points, using both the *DRL-Model* (shown in blue) and the *Human-Avg-Model* (shown in red) across all participating subjects. The error bar represents the standard deviation of estimation error values.

it is expected to have good prediction results. Although the *DRL-Model* with an overall average RMSE value of 5.14° exhibits slightly lower performance compared to the *Human-Avg-Model* with an overall average RMSE value of 4.03°, the results demonstrate its successful prediction of elbow joint angles with sufficient accuracy for all subjects.

This highlights the effectiveness of synthetic motion data in training a neural network model for predicting natural human motion. Notably, for testing the *DRL-Model*, human motion data are used as input, which differs entirely from the synthetic motion dataset used for training. However, it still achieves reasonable accuracy in predicting elbow joint motion for all subjects. This highlights the robustness of the *DRL-Model* in accommodating inter-subject variability.

Furthermore, we analyzed the target point reaching error associated with the predicted elbow joint motion for both the *DRL-Model* and the *Human-Avg-Model*. For this evaluation, we utilized a Unity 3D simulation with a humanoid actor, as detailed in Section 3.2.6. This animation process involved visualizing not only the predicted motion data generated by both the *DRL-Model* and the *Human-Avg-Model* but also the subject's original motion data. During the simulation, we tracked the position of the middle finger's fingertip as the humanoid actor executed the reaching movements toward each designated target point. The target point reaching error was determined relative to the actual arm reaching movements for each individual

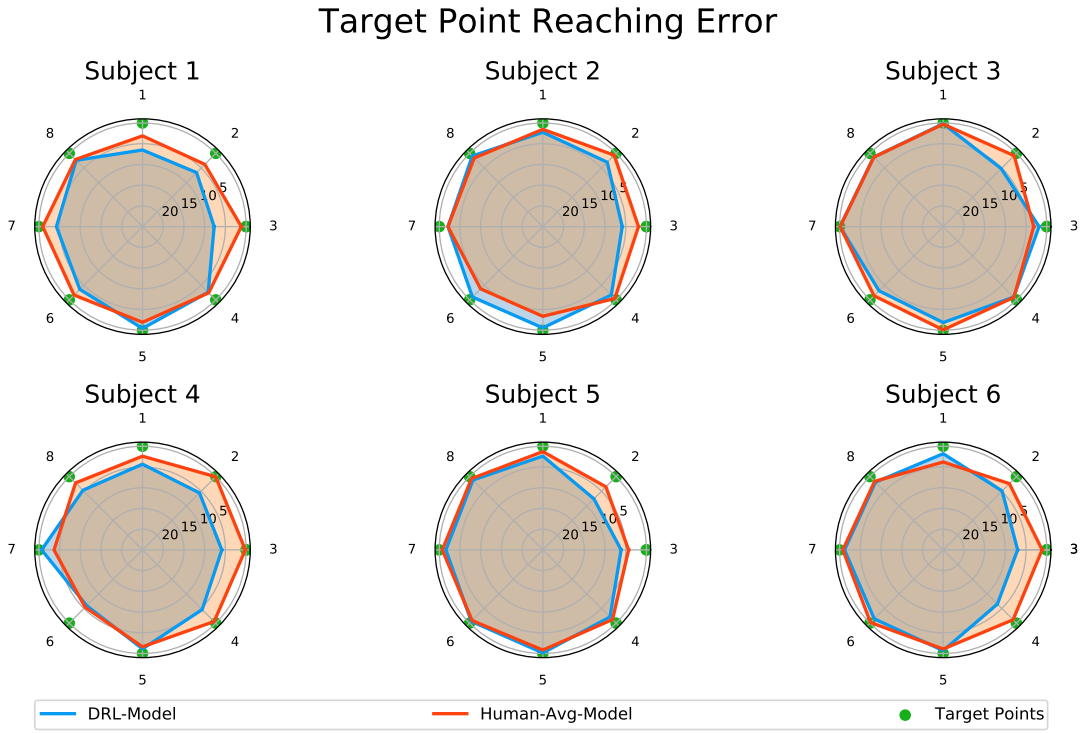

Figure 3.9: Comparison of the target reaching error for motion predictions of the *DRL-Model* and the *Human-Avg-Model*. The polar charts present the target reaching error for each point across all subjects for the *DRL-Model* in blue and the *Human-Avg-Model* in red, where the radial axis indicates the scale of the position error measured in centimeters.

subject, as animated in the Unity 3D simulation.

Figure 3.9 presents a comparison of the target reaching error based on the predictions made by the *DRL-Model* and the *Human-Avg-Model*, illustrated on polar charts. The predicted motion data from both the *DRL-Model* and the *Human-Avg-Model* demonstrated the successful reaching of most target points with reasonable accuracy across all subjects. Although there were slight variations in a few cases, the overall trend of final position errors was similar for both models, with an average overall mean value of 3.03 cm for the *DRL-Model* and 1.75 cm for the *Human-Avg-Model*, respectively.

It is important to note that the humanoid actor in the simulation solely relied on shoulder and elbow joint angular data to animate the reaching movements without incorporating compensatory movements such as trunk and shoulder displacements. In real scenarios, slight compensatory movements could further enhance the accuracy of the target point reaching error. These results further validate the effectiveness of our DRL-based synthetic motion data in accurately predicting the elbow joint motion during natural human movements.

3.3.1 Motion Data Augmentation: Cross-Subject Evaluation

To assess the impact of integrating DRL-Data with Real-Data on the performance of our predictive models, we developed CNN-LSTM models, namely the *Human-Sparse-Model* and *Hybrid-Model* (see Section 3.2.5), representing a scenario with limited training data availability. Subsequently, we conducted a cross-subject evaluation by utilizing the sparse model of one subject to predict the elbow joint motion of all other participating subjects. This approach accounts for the inherent inter-subject variability, providing valuable insights into the robustness and transferability of the trained predictive models.

Figure 3.10 presents the RMSE values obtained from the cross-subject evaluation of the *Hybrid-Model* and the *Human-Sparse-Model*, represented as a box plot. The box size indicates the range encompassing 75% of the sample values, with the solid vertical golden line inside representing the median. A black diamond marker indicates the mean value. Smaller box sizes and smaller mean and median values indicate less variation in the prediction results and better overall performance.

The results depicted in Figure 3.10 demonstrate that the *Hybrid-Model* had improved performance for all six subjects, as indicated by its smaller box size along with the lower mean RMSE values compared to the *Human-Sparse-Model*. This can also be observed from the percentage breakdown of the performance improvement presented in Table 3.1. The overall cross-subject results show that the *Hybrid-Model* had an overall average RMSE value of 5.72°, whereas the *Human-Sparse-Model* had an overall average RMSE value of 6.35° with an overall average improvement of about 10% in the prediction performance.

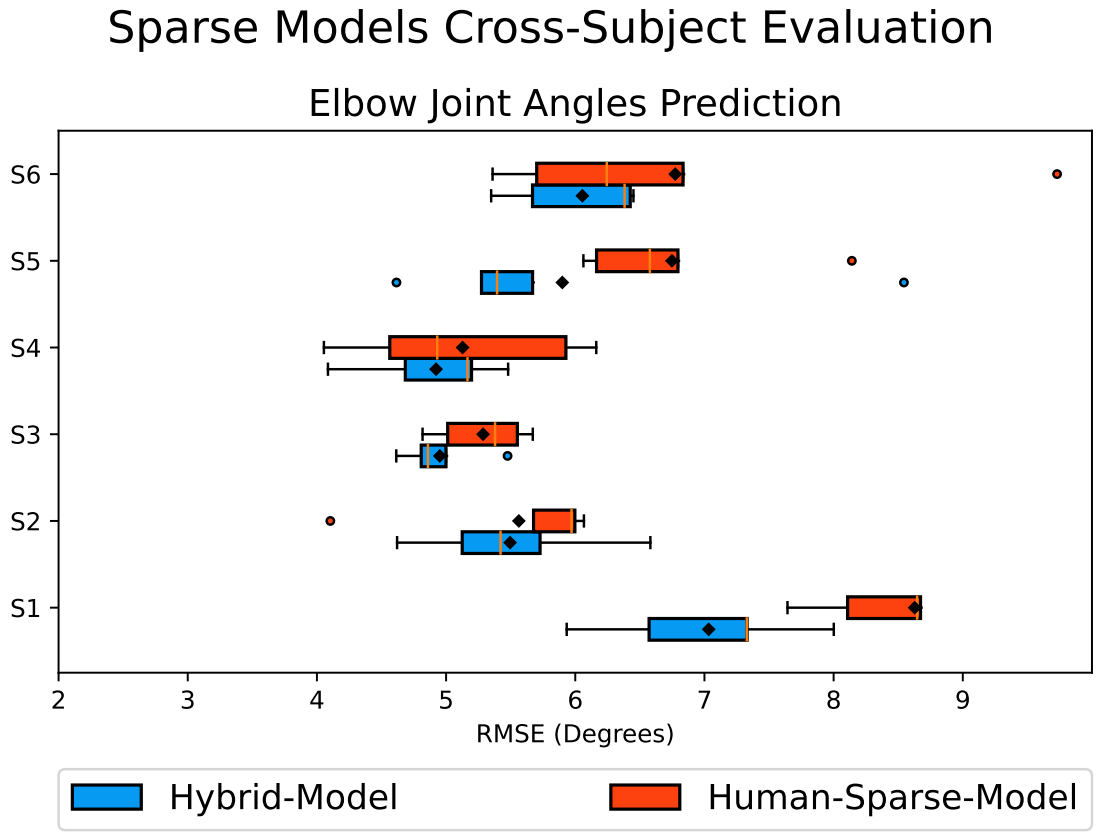

Figure 3.10: Box plot of the RMSE values comparing the predicted and actual elbow joint angles obtained from the cross-subject evaluation of the *Hybrid-Model* in blue and *Human-Sparse-Model* in red. The box size represents the range encompassing 75% of the values, with the solid vertical golden line inside indicating the median. A black diamond marker denotes the mean value. Circular markers represent outliers; the whiskers indicate maximum and minimum values. Smaller box sizes, along with lower mean and median RMSE values, indicate better performance.

These findings highlight the potential of integrating DRL-Data with Real-Data to enhance the overall performance and robustness of the predictive model. Augmenting the subject's data with the additional synthetic motion data enriches the training dataset's diversity, contributing to improved model performance.

3.4 Discussion

We propose a DRL-based motion cloning framework for the synthetic motion generation of arm reaching movements. The synthetic motion data effectively supplement and diversify the training motion data, addressing the challenge of acquiring large motion datasets from human subjects for training a predictive model. Our evaluation results showcase the efficacy of cloned motion data in accurately predicting natural human elbow joint movements. Furthermore, motion data augmentation demonstrated the enhanced performance of the predictive model across multiple subjects in the case of the decoder based on human experiments.

We assessed the quality of the cloned motion data (DRL-Data) generated through our DRL simulation by examining its correlation with the averaged human motion data and comparing the results to that of Real-Data obtained from all participating subjects. Pearson's correlation coefficient analysis revealed a strong similarity between the cloned DRL-Data and the motion data from the other subjects, albeit with slight variations in correlation values due to the inherent inter-individual variability. These results highlight that the synthetic dataset generated by our DRL-based motion cloning framework can be considered as an additional subject within the experiment. Such findings provide compelling evidence supporting the effectiveness of our DRL-based motion cloning framework in successfully synthesizing human-like synergistic motion.

We used synthetic motion data to train a predictive model, the *DRL-Model*, and evaluated its performance against the *Human-Avg-Model* (used as the gold standard), which was trained using the averaged human motion data from all the participating subjects. We employed metrics such as Pearson's correlation coefficient and RMSE values to measure the linearity and average difference between the estimated and actual joint angular values. Both predictive models exhibited a similar performance, as evidenced by comparable Pearson's correlation coefficient values and minor differences in overall RMSE values. This indicates that the synthetic motion data successfully captured the essential reaching movement synergistic patterns, enabling the effective training of the *DRL-Model*. Notably, the *DRL-Model* was tested using human motion data as input, which uniquely differs from the synthetic motion data used for training. Nonetheless, it accurately predicted the elbow joint motion across all subjects, demonstrating the robustness of the DRL-Model in accommodating inter-subject variability.

We also conducted a visual analysis of the predicted motion using a Unity 3D simulation, where a humanoid actor animated the reaching movements toward all target points. We calculated the target reaching error to assess the accuracy of the estimations. The results demonstrated that both the *DRL-Model* and the *Human-Avg-Model* successfully reached the target points with reasonable accuracy. While there were slight variations in a few cases, both models produced similar overall target reaching errors. It is important to note that the humanoid actor in the simulation solely relied on shoulder and elbow joint angular data to animate the

Table 3.1: Percentage breakdown of sparse models' cross-subject evaluation performance.

Model	**Mean RMSE Value Human-Sparse-Model**	**Mean RMSE Value Hybrid-Model**	**Percentage Improvement**
S1	8.63	7.03	18.48%
S2	5.56	5.50	1.22%
S3	5.29	4.95	6.34%
S4	5.13	4.92	4.01%
S5	6.75	5.90	12.58%
S6	6.77	6.05	10.61%

reaching movements without incorporating compensatory movements. Therefore, the target reaching errors can be further improved in real scenarios by incorporating slight compensatory movements such as trunk and shoulder displacements.

Finally, we investigated the impact of integrating DRL-Data with the Real-Data for training purposes to enhance the performance of the predictive models. We trained predictive models with sparse training data, namely *Human-Sparse-Model* and *Hybrid-Model*, and evaluated their prediction accuracy through a cross-subject evaluation. The results reveal that the *Hybrid-Model* outperformed the *Human-Sparse-Model*, demonstrating improved performance in all six subjects, as indicated by the smaller box plot size and lower overall average RMSE values. These findings highlight the potential of integrating DRL-Data with Real-Data, leading to the predictive model's enhanced overall performance and robustness. The training dataset becomes more diverse by augmenting the subject's data with additional synthetic motion data, contributing to improved model performance.

In this study, we explored synthetic motion generation with a specific focus on fundamental horizontal-plane reaching movements and its utilization in motion data augmentation to improve the predictive model's performance. Looking ahead, our research trajectory entails an in-depth exploration of the domain of synthetic motion data generation. We are striving to enhance the accuracy and diversity of the synthetic dataset through the implementation of advanced DRL techniques to encompass a broader range of dynamic movements and scenarios.

3.5 Conclusions

This study unveils the potential of synthetically generated motion data using a DRL-based motion learning approach to accurately replicate human-like synergistic arm movements and their effectiveness in training predictive models capable of accurately predicting actual human arm movements.

We present a novel DRL-based motion cloning framework designed explicitly for synthesizing motion data for arm reaching movements. Through our analysis, we confirmed that the synthetic motion data closely resemble the characteristics of motion data obtained from human subjects and effectively capture the synergistic patterns of the arm reaching movements, enabling the training of an accurate predictive model. Our trained model demonstrates the ability to predict elbow joint motion across diverse human subjects, achieving an overall average RMSE value of 5.14° and accurately reaching the target points. Notably, our results highlight the significant advantages of integrating synthetic motion data with actual motion data from human subjects during training, enhancing the performance and robustness of the predictive models in a cross-subject evaluation setting, with an overall average RMSE value of 5.72°.

This initial investigation showcases the potential of the proposed DRL-based motion cloning framework in successfully synthesizing and leveraging synthetic motion data to enhance the accuracy and reliability of predictive models in capturing

natural human-like movements. Our evaluations yield compelling evidence, affirming the ability of the cloned motion data to accurately predict natural elbow motion across multiple subjects. Moreover, the cloned motion data can supplement limited data availability and diversify the training data, contributing to improved generalization. These findings have significant implications for creating comprehensive synthetic motion dataset resources for diverse arm movements and advancing automated prosthetic elbow motion strategies.

Chapter 4

Real-Time Prediction of the Elbow Joint Motion During Extensive Arm-Reaching Activities

4.1 Introduction

Over the years, significant progress has been made in the design and control of prosthetic arms. However, a fundamental challenge persists for transhumeral amputees when utilizing a prosthesis, specifically in the intricate control of its multiple joints. Navigating the prosthetic elbow and wrist joints to position the hand accurately and coordinating these joint movements while reaching for objects remains a highly challenging task.

Transhumeral amputees experience the loss of all forearm and wrist muscles [3]. Furthermore, they must control the crucial elbow joint to effectively manage the multiple degrees of freedom (DOFs) inherent in a prosthetic arm. Various advanced practices have emerged to enhance the controllability that transhumeral amputees can exert over their prosthetic devices. Techniques such as targeted muscle reinnervation (TMR) [91], [92], a surgical procedure involving the transfer of residual arm nerves to alternative muscle sites, facilitate access to neural control information for the arm, which is compromised by amputation. Following reinnervation, these targeted muscles generate an electromyogram (EMG) on the skin's surface, measurable and providing additional signals for enhanced control.

Osseointegration [93] and neuromusculoskeletal implants [94] represent a new era in human-machine integration, where the prosthetic arm is directly anchored to the skeleton. This innovative approach combines surgical reconstruction procedures with implanted electrodes and a long-term stable neuromusculoskeletal interface for prosthesis control [95]. This skeletal interface facilitates bidirectional communication between the external prosthesis and internal neuromuscular interfaces, offering the potential for feedback to users, such as tactile sensations. These advancements can improve task performance closer to the abilities of a healthy human.

Despite their advantages, the testing and evaluation of these control strategies are challenging and expensive. They necessitate complex and highly invasive surgeries, expertise for which is available at only a few medical institutions with specialized specialists. Additionally, the optimization of these strategies requires advanced signal processing techniques, as well as the development of decoding and classification algorithms for sensorimotor signals [96], [97]. Obtaining willing subjects and extensive training requirements poses yet another limitation.

This study presents an alternative, non-invasive, and easily accessible approach based on residual shoulder motion data for predicting and evaluating elbow joint motion in transhumeral prosthesis control. Our proposed method capitalizes on the natural synergistic coordination between the arm joints [98], [99] and entails the development of artificial neural network (ANN)-based predictive models to control the pronation-supination ($E\theta_x$) and flexion-extension ($E\theta_y$) angles of the elbow joint during extensive arm reaching motions.

To overcome the challenges associated with clinical trials, we have developed a virtual reality (VR)-based interactive framework for real-time validation and evaluation of the predictive models. Amputee users can wear sensors on their bodies to control a humanoid actor in a virtual workspace, requiring minimal preparation for testing the control strategy. The overarching concept involves creating a platform for initially acquiring motion data from healthy subjects that are used to train predictive models for transhumeral prosthesis elbow control and subsequently validating their efficacy on amputee subjects. We can readily modify and adapt the experimental setup as the experiments for arm-reaching movement tasks occur in a virtual workspace. In this study, we demonstrate the real-time prediction of elbow joint motion during extensive arm-reaching activities, successfully validated with a right arm transhumeral amputee user.

This paper is organized as follows. Section 4.2 presents our proposed framework, including details on the experimental protocols and the implementation of virtual workspace. The ANN training strategy and the method employed for performance evaluation are also described in this section. The results are presented in Section 4.3 and discussed in Section 4.4. Finally, we draw conclusions and discuss future works in Section 4.5.

4.2 Materials and Methods

4.2.1 Apparatus

This study is centered on the real-time prediction of elbow joint motion, specifically with applications in transhumeral prosthesis control. To achieve this objective, we have developed a Virtual Reality (VR) platform that allows subjects to interact with a 3D workspace and perform the reaching tasks with the full range of arm motion. The fundamental framework of this VR platform is visually illustrated in Figure 4.1.

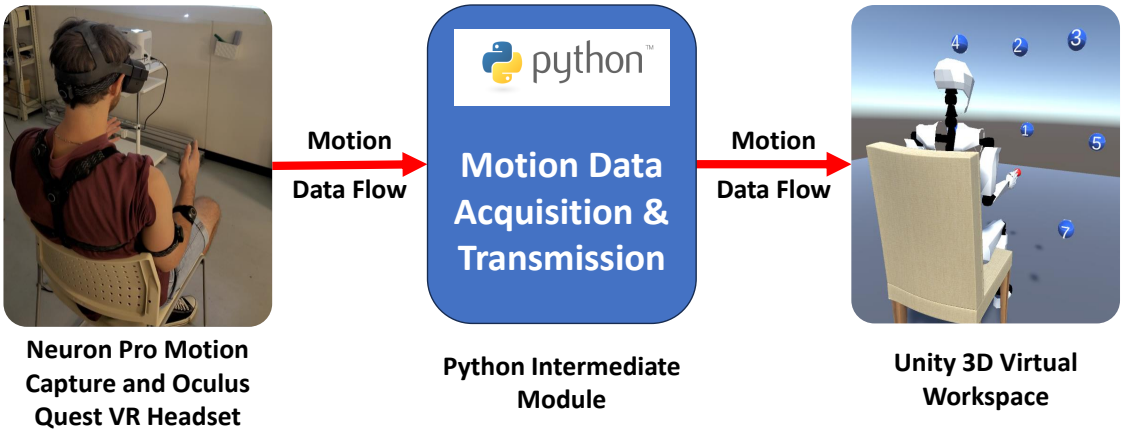

Figure 4.1: Virtual Reality (VR) platform architecture: The Neuron Pro system processes motion data, which is then relayed to the Python module. The module serves a dual role, saving the data into a file for future reference and transmitting it to the Unity 3D simulation for real-time visualization.

The VR platform has three elements. We employed the Perception Neuron Pro system to capture how a subject's arm moves while they reach for targets in VR. This system utilizes Inertial Measurement Unit (IMU) sensors for motion capture. While the precision of this system may be somewhat lower when compared to optical camera-based alternatives, it has the advantage of working without any restrictions in terms of where you can use it. Subjects can conveniently wear the sensors using adjustable straps, eliminating the need for any additional preparations. The sensor system interfaces with the Axis Neuron Pro software, facilitating the real-time processing of raw motion data and the construction of a dynamic 3D skeletal model.

The motion data from the constructed skeletal model, including joint positions and angles, is subsequently relayed to an intermediary Python module. This module operates on a dual front: it saves the angular data of the joints for future reference while simultaneously facilitating the transmission of this dataset to the Unity 3D simulation for real-time visualization. As part of this integrated system, subjects can actively control the movements of the humanoid actor's arms, torso, and head, effectively immersing them in the realm of virtual reality.

4.2.2 Data Acquisition and Experiment Protocols

Our study involved the voluntary participation of six individuals, all right-handed, comprising four males and two females, alongside one participant with a transhumeral amputation of the right arm. The healthy subjects, aged between 20 and 28, exhibited no documented upper body neuromuscular disorders, while the amputee participant was 30 years old. Before their involvement in the experiments, all subjects provided informed consent.

This study is centered on the real-time prediction of the pronation-supination and flexion-extension angles of the elbow joint during extensive arm-reaching activities within a three-dimensional workspace. Our virtual environment features a seated humanoid actor positioned on a chair, with the target points to be reached being distinctly marked as blue spheres, as depicted in Figure 4.2. Our experimental design explores the full range of arm-reaching motions, tasking subjects with reaching eight designated target points distributed across a spacious right-arm workspace, as illustrated in Figure 4.2a. To actively engage with this virtual reality setting and perform the necessary reaching tasks, participants use the Neuron Pro motion capture system and the Oculus Quest VR headset to control the actions of the humanoid actor in real-time.

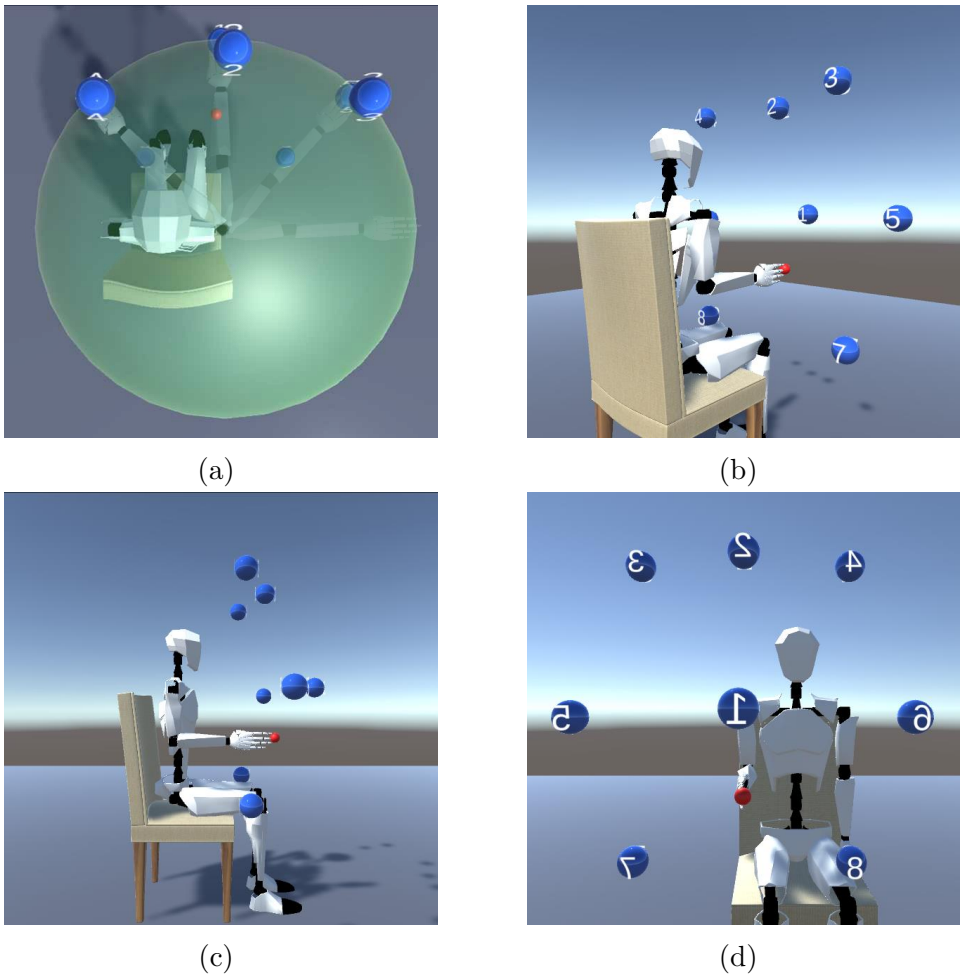

(a) (b)

(c) (d)

Figure 4.2: Experimental Setup for Extensive Arm-Reaching Movements: A humanoid actor sits on a chair in a virtual 3D workspace. Target points for reaching are denoted by numbered blue spheres, while a small red sphere indicates the rest/start point. (a) An illustration of the wide workspace with target points spanning the extensive reaching range (green-shaded region) for the subject's right arm movements. (b) An isometric view of the humanoid actor and the target points in the virtual workspace. (c) A side view of the humanoid actor with the right hand in a rest/starting pose. (d) A front view of the humanoid actor within the virtual workspace.

The experimental task involves the subjects seated straight on a chair and performing a sequence of reaching movements, commencing from a resting position marked by a distinctive red sphere, wherein the right arm is positioned in a rest stance, with the shoulder joint in a downward orientation and the elbow joint bent at a 90° angle, as depicted in Figure 4.2c. Subsequently, subjects are directed to reach and contact a designated blue target sphere, which is set to disappear upon the humanoid actor's fingertip contact. Following the target sphere's disappearance, participants must return to the central point and return the arm to the rest position. This process is followed by a brief pause at the rest point before initiating the next cycle to reach the subsequent target sphere. This movement task is referred to as the "center-out-center" reaching task. Throughout the experimental sessions, participants received instructions to execute the center-out-center reaching movements encompassing all eight target points within the virtual workspace.

We captured the natural arm movements of our healthy subjects, along with their head orientation while they performed these arm-reaching tasks and subsequently used this data to train various ANN models. These models were designed to predict elbow joint motion during similar reaching tasks, a critical aspect of transhumeral prosthesis control. In our experimental framework, the primary focus was on collecting data related to the orientation angles of the shoulder joint, encompassing internal-external rotation ($S\theta_x$), flexion-extension ($S\theta_y$), and abduction-adduction ($S\theta_z$) movements. Additionally, we recorded orientation angles of the elbow joint, covering pronation-supination ($E\theta_x$) and flexion-extension ($E\theta_y$). Furthermore, we monitored three head orientation angles: pitch (vertical movement $H\theta_x$), yaw (horizontal movement $H\theta_y$), and roll (rotational motion $H\theta_z$). Hereafter, these joint angles will be referred to as $H\theta_x$, $H\theta_y$ & $H\theta_z$ for the head, $S\theta_x$, $S\theta_y$ & $S\theta_z$ for the shoulder, and $E\theta_x$ & $E\theta_y$ for the elbow, respectively.

4.2.3 Synergy-Space Neural Network Training

The subsequent phase of our investigation involved training our ANN models to predict elbow joint motion during similar arm-reaching tasks as carried out in the experiment. This predictive framework relied on the kinematic data obtained from the shoulder joint. For this purpose, we implemented the synergy-space neural network strategy as detailed in a prior research study [77]. This strategy uniquely leveraged the principle of synergy, capitalizing on the inherent coordination observed among arm joints during reaching movements. The core objective was to facilitate the accurate prediction of elbow joint motion, characterized by both energy efficiency and human-like movements.

In contrast to the conventional approach of supervised training for ANNs, this method introduces a novel sequence of steps (Fig. 4.3). Initially, it explicitly extracts the inherent synergistic elements and time-varying activation signals from the source data, as depicted in Equation (4.2.1), through the application of Principal Component Analysis (PCA). Subsequently, the ANN's learning process integrates the most pertinent synergy components. This integration aims to refine the ANN training, capitalizing on the shared nature of these synergies, thereby augmenting

the model's overall transferability. Ultimately, the prediction of elbow joint motions is achieved using Equation (4.2.2), in which the initially extracted activation signals, denoted as C, are substituted with the ANN-predicted signals, designated as C_p.

$$x^l(t) = \sum_{n=1}^{N} w_n \cdot c_n^l(t) + residuals \tag{4.2.1}$$

$$X = W \cdot C \tag{4.2.2}$$

Convolutional Long Short-Term Memory (CNN-LSTM) Neural Network

To train a synergy-space neural network model to predict elbow joint motion for transhumeral prosthesis control, we employed convolutional long short-term memory (CNN-LSTM) neural networks. Recent investigations, exemplified by the study on human activity recognition presented in [89], have explored combining CNN and LSTM layers to enhance predictive performance. This fusion of networks is rooted in the recognition that the quality of the input can constrain LSTM's efficacy features it receives, as indicated in [90]. Including CNN layers, adept at reducing input frequency variance and distilling salient features, greatly enhances the overall feature representation. Subsequently, LSTM layers capture temporal dependencies embedded within these extracted features.

The CNN-LSTM architecture combines the inherent advantages of both CNN and LSTM layers. These neural network components have previously demonstrated remarkable efficacy in various time series prediction and classification tasks. Notably, in our approach, we unify the functionality of CNN and LSTM layers within a single cohesive architecture, facilitating optimized training across all layers.

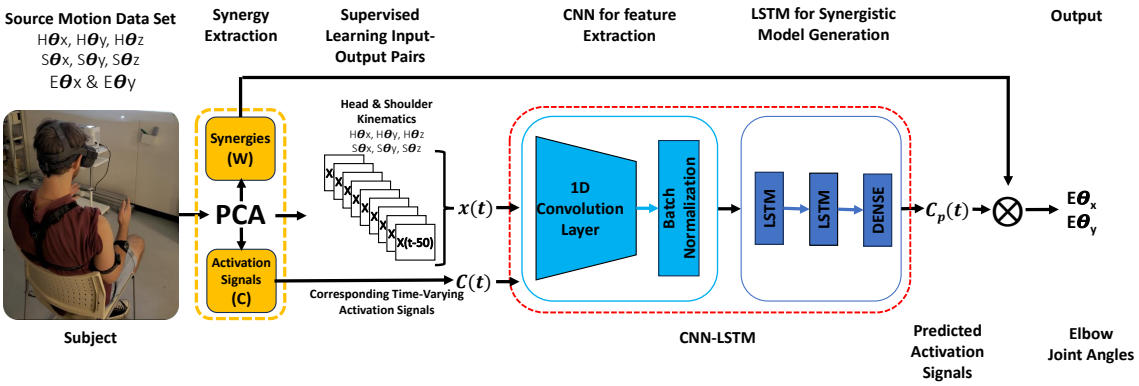

Figure 4.3: Synergy-Space Neural Network training strategy for CNN-LSTM

Our CNN-LSTM model was implemented using the Python machine-learning library Keras. The architecture features a single one-dimensional CNN layer, complemented by two LSTM layers comprising 256 nodes. A concluding dense layer, along with the Adam optimization function, was included in the configuration (see Fig. 4.3). This design facilitated the network's proficiency in feature extraction from the input data and the modeling of essential temporal dependencies, ultimately enhancing the accuracy of the estimation process.

The training process adhered to a supervised learning paradigm, in which the CNN-LSTM was made to formulate a regression model based on the input-output pairs to estimate the time-varying activation signals. Subsequently, in conjunction with the extracted synergy matrix, these predicted activation signals are utilized to predict the angular movements associated with elbow joint pronation-supination and flexion-extension as depicted in Figure 4.3.

4.2.4 Analysis Strategy

Our analytical methodology involved training various CNN-LSTM models, each rooted in distinct training data configurations. In particular, we trained 3-DOF CNN-LSTM models that exclusively incorporated the joint angular data from the three DOFs of the shoulder joint ($S\theta_x$, $S\theta_y$ & $S\theta_z$) as its input. Additionally, we developed 6-DOF CNN-LSTM models, which utilized composite joint angular data input, combining three DOFs related to head orientation angles ($H\theta_x$, $H\theta_y$ & $H\theta_z$) and the three DOFs of the shoulder joint angles ($S\theta_x$, $S\theta_y$ & $S\theta_z$).

This classification was driven by the investigation into whether the integration of head orientation information could yield improvements in the predictive capabilities of the CNN-LSTM models. Given the spatial distribution of the target points across a wide workspace, it was observed that subjects often altered their head orientation to focus on the target points during reaching tasks visually. Therefore, using head orientation data can prove to be useful for training the predictive models. Details of the different CNN-LSTM models trained in our study:

Personalized CNN-LSTM Models (P-Models)

Firstly, we conducted an assessment to ascertain whether the incorporation of head orientation data yields enhancements in the predictive capabilities of the CNN-LSTM models. We specifically developed personalized CNN-LSTM models, henceforth referred to as *P-Models*, which were trained using the motion dataset unique to each individual healthy human subject. These models are labeled as "personalized" since they are exclusively trained and tested using the motion data of a single subject, rendering the predictive model inherently individualized to that specific subject.

We developed two distinct CNN-LSTM models for each subject to facilitate a comprehensive comparison: the *3DOF-P-Model* and the *6DOF-P-Model*. Given the participation of six healthy subjects in our experiments, we consequently trained a total of 12 *P-Models* (comprising both the 3DOF and 6DOF versions for each subject). This comprehensive approach allowed us to effectively gauge the utility of integrating head orientation information in the training of predictive models. Details of the trained personalized CNN-LSTM models are provided below:

- *3DOF-P-Model:*
  We conducted training for six unique *3DOF-P-Models*, with each model being developed using the motion data exclusively acquired from an individual human subject. The *3DOF-P-Model* is characterized by its sole utilization of joint angular data from the three DOFs of the shoulder joint ($S\theta_x$, $S\theta_y$ & $S\theta_z$) as the exclusive training input for the predictive model.
- *6DOF-P-Model:*
  A total of six individual *6DOF-P-Models* were trained, using the motion data acquired from an individual human subject. The *6DOF-P-Model* stands out for its integration of the three DOFs associated with head orientation angles ($H\theta_x$, $H\theta_y$ & $H\theta_z$) with the three DOFs the shoulder joint angles ($S\theta_x$, $S\theta_y$ & $S\theta_z$) as the combined training input for the predictive model.
- Performance Assessment:
  We evaluated how well the P-Models performed by testing each model with the specific subject's motion data and then compared the predicted elbow joint angles ($E\theta_x$ & $E\theta_y$) to the subject's actual elbow joint angles.

Generic CNN-LSTM Models (G-Models)

The primary goal of this study was to create a real-time prediction platform for elbow joint motion during extensive reaching tasks, specifically geared for transhumeral prosthesis control. We developed a set of generic CNN-LSTM models to achieve this objective, referred to as *G-Models*. These models were trained using the collective motion data sets obtained from the six participating subjects. The term "generic" is aptly applied since this single predictive model is designed to predict the elbow joint motion for diverse subjects, as it has been trained using data from many subjects. Furthermore, our training methodology was reinforced by implementing the synergy-space neural network strategy [77]. This synergistic methodology was employed to enhance the robustness and adaptability of the predictive model in accommodating inter-individual variabilities commonly encountered during reaching movements.

In this particular context, we extended our exploration by developing distinct variations of the *G-Models*, each founded on specific input data configurations. More precisely, two categories of *G-Models* were trained: the simple generic model *G-Model* and the averaged generic model *G-Models-AVG*. This categorization stemmed from our interest in investigating whether using averaged motion data alone could effectively create a generic predictive model.

This was motivated by the recognition that the quantity of motion data employed for training directly impacts the computational resources and time required for the predictive model's training process. So, with this, we examined whether the amalgamation of motion data from all subjects into a consolidated dataset of refined reaching movements toward all target points could present a pragmatic solution for mitigating the computational and time requirements inherent to the training of predictive models. Details of the trained generic CNN-LSTM models are as follows:

- *G-Model:*
  We created two simple generic CNN-LSTM models, *G-Models*, trained using two different input data configurations: the 3-DOF and 6-DOF setups, as detailed in Section 4.2.4. In the training of each *G-Model*, we utilized motion data sets encompassing contributions from all six healthy subjects who participated in the study. Each subject's dataset included a single iteration of reaching movements directed at all the designated target points within the virtual workspace. Consequently, the collective training dataset comprised six iterations of reaching movements for each target point.

- *G-Model-AVG:*
  Two averaged generic CNN-LSTMs, *G-Models-AVG*, were trained based on the 3-DOF and 6-DOF input data configuration (as described in Section 4.2.4). In the training process for each *G-Model*, we leveraged an averaged motion dataset formed by pooling motion data from all six participating healthy subjects. The collective training motion dataset comprised a single iteration of refined and averaged reaching movements directed at all the specified target points within the virtual workspace.

- Performance Assessment:
  In the case of the generic models, we conducted both offline and real-time testing. For the offline assessments, we utilized the recorded motion data from the healthy participants as input for the predictive models. In contrast, the real-time testing involved an individual with a right arm transhumeral amputation who actively controlled the humanoid actor and executed the target-reaching tasks within the virtual workspace. Firstly, the amputee subject's successful reaching and touching of the target points in the virtual workspace was considered an accurate prediction of the elbow joint angles. Secondly, given that the amputee participant could not provide direct data on their actual elbow joint angles, we resorted to tracking and comparing the fingertip motions of both healthy and amputee participants during the reaching movements to evaluate model performance.

4.2.5 Evaluation

To comprehensively evaluate and assess the performance of the CNN-LSTM models in their ability to predict elbow joint angles, we utilized established evaluation metrics, including the root mean squared error ($RMSE$) and Pearson's correlation coefficient.

Root Mean Squared Error ($RMSE$)

The $RMSE$ metric is a valuable indicator for assessing the overall accuracy and precision of the elbow joint angles predicted by the CNN-LSTM models. We conducted a comparative analysis between the estimated elbow joint angles, specifically pronation-supination $E\theta_x$ and flexion-extension $E\theta_y$, and the subject's original elbow joint angles obtained during the recorded reaching movements, as captured by the neuron pro system. This comparison was made using the ($RMSE$) metric, defined in Equation (4.2.3), where $\hat{x}_t$ represents the predicted joint angle and x_t represents the actual joint angle at data point t. The total number of data points is denoted by N.

$$RMSE = \sqrt{\frac{1}{N}\sum_{t=0}^{N}(\hat{x}_t - x_t)^2} \tag{4.2.3}$$

Pearson Correlation Coefficient

Through the application of Pearson's correlation coefficient, we could gauge the extent of linearity between the predicted joint angles and their actual counterparts. This approach afforded valuable insights into the model's capacity to capture the inherent synergistic patterns within the dataset. Pearson's correlation method, employed to examine the linear relationship between two variables and quantify the strength of their correlation, yields a coefficient denoted as "r". This coefficient, which ranges between -1 and $+1$, offers a comprehensive understanding of the correlation's magnitude and direction.

The Pearson correlation coefficient was computed using Python's NumPy library's "corrcoef' function. This function was applied to the subject's actual elbow joint angles and the predicted elbow joint angles derived from the CNN-LSTM models. In addition to its application in assessing model performance, we also utilized this metric for comparative evaluations of fingertip tracking in both offline and real-time scenarios, particularly concerning the performance of the generic models.

Fingertip Tracking

To assess the accuracy of the predicted reaching movements during real-time tests, we made the decision to assess the similarity of these movements through the tracking of the right hand's fingertip of the humanoid actor. It's important to note that providing the original elbow joint angles for evaluation was impossible for the transhumeral amputee subject in the real-time testing scenario. Consequently, our evaluation involved the reanimation of the recorded joint angular data from each subject's original motion data and a comparison with the motion data predicted by the generic CNN-LSTM models, specifically the *G-Model* and *G-Model-AVG*.

The Unity simulation faithfully replicated the setup of the human subject arm motion data acquisition experiment, with a humanoid actor seated upright on a chair executing a sequence of reaching movements toward all the designated target points within the 3D virtual workspace. The position of the actor's right hand's middle finger was tracked and recorded throughout these movements.

In our evaluation, we utilized Pearson's correlation coefficient metric to conduct comparative analyses of fingertip tracking, enabling a comprehensive performance assessment. This Unity-based evaluation facilitated quantitative assessments and provided invaluable visual insights into the effectiveness of the generic CNN-LSTM models in accurately predicting arm-reaching motions.

4.3 Experimental Results

In this section, we present the results of our proposed framework's analysis for real-time prediction and evaluation of elbow joint motion in a virtual workspace for transhumeral prosthesis control. Firstly, we illustrate that integrating head orientation information with shoulder joint angles during extensive arm-reaching movements enhances the performance of predictive models. This enhancement is verified through performance comparisons between models trained with *3-DOF* and *6-DOF* input data configurations. Subsequently, we highlight the effectiveness of the *G-Model-AVG* in predicting elbow joint motion across different human subjects—a CNN-LSTM model trained using the averaged motion dataset from the recorded reaching movements of all six participating healthy subjects. The *G-Model-AVG* CNN-LSTM achieved similar performance accuracy to the simple generic model *G-Model* while utilizing approximately three times fewer resources and training time.

Finally, as the primary objective of this study, we validated the platform with a transhumeral amputee subject, showcasing the successful real-time predictive capability of the trained generic models. The amputee user reached and touched all target points within the virtual workspace without needing prior training or fine-tuning of the predictive model.

4.3.1 Personalized Models Evaluation: 3DOF vs 6DOF

Initiating our assessment with the effectiveness of incorporating the three DOFs associated with head orientation angles ($H\theta_x$, $H\theta_y$ & $H\theta_z$) along with the three DOFs of shoulder joint angles ($S\theta_x$, $S\theta_y$ & $S\theta_z$) as input for training the predictive model, our analysis centered on comparing the accuracy of personalized models (see Section 4.2.4), specifically the *3DOF-P-Model* and *6DOF-P-Model*, in predicting elbow joint motion during actual human arm reaching movements. To achieve this, each *P-Model* received the corresponding subject's original recorded motion data as input, enabling a direct comparison between the predicted and original elbow joint angles.

Observations from our experiments with healthy subjects' data acquisition revealed a consistent tendency among participants to adjust their head positions to visually focus on the specific target point in the virtual workspace during reaching tasks. We hypothesized that this coordinated head movement, synchronized with arm motions, could be effectively leveraged for training predictive models. Following the training of both the *3DOF-P-Model* and *6DOF-P-Model* personalized models for all subjects, we applied them to predict elbow joint angles ($E\theta_x$ & $E\theta_y$) during reaching motions. Subsequently, we compared the estimated elbow joint angular values with the subjects' original elbow joint angles to conduct a thorough performance analysis.

The results of the prediction performance analysis for both the *3DOF-P-Model* (in blue) and *6DOF-P-Model* (in orange) for one of the subjects are presented in Figure 4.4. The line graph illustrates the variation in the elbow joint angles (pronation-supination $E\theta_x$ and flexion-extension $E\theta_y$) during reaching movements toward each target point. Simultaneously, the adjacent bars indicate the calculated Pearson's correlation coefficient "r" values comparing the subject's original (shown in black) and predicted joint angular variation. Additionally, as depicted in the bar graph in the last column, we computed the overall $RMSE$ value by comparing the estimated and original joint angular values for reaching movements toward all target points. Based on the calculated r values, both models can predict the elbow joint angles with sufficient accuracy. However, the significant difference in the overall $RMSE$ value in Figure 4.4 indicates that the *6DOF-P-Model* exhibited superior performance, suggesting the effectiveness of using head orientation data.

In Figure 4.5, the box plot illustrates the $RMSE$ values derived from the prediction results of both the *3DOF-P-Model* and *6DOF-P-Model* personalized models across all six healthy human subjects. The box size delineates the range covering 75% of the sample values, while the solid horizontal black line signifies the median. A black diamond marker denotes the mean value. Smaller box sizes and lower mean and median $RMSE$ values are indicative of reduced variation in the prediction results, reflecting superior overall performance.

The results illustrated in Figure 4.5 reveal the enhanced performance of the personalized *6DOF-P-Model* across all six healthy subjects. This improvement is evidenced by the smaller box size and lower mean RMSE values of the box plot compared to the *3DOF-P-Model*. A detailed breakdown of performance improvement is presented in Table 4.1, showcasing the *6DOF-P-Model* with an overall mean $RMSE$ value of 4.35°, while the *3DOF-P-Model* recorded an overall mean $RMSE$ value of 5.67°. This represents an average improvement of approximately 23.24% in prediction performance. These findings underscore the potential of integrating head orientation information with shoulder joint angular data during training, emphasizing its role in enhancing the predictive model's overall performance.

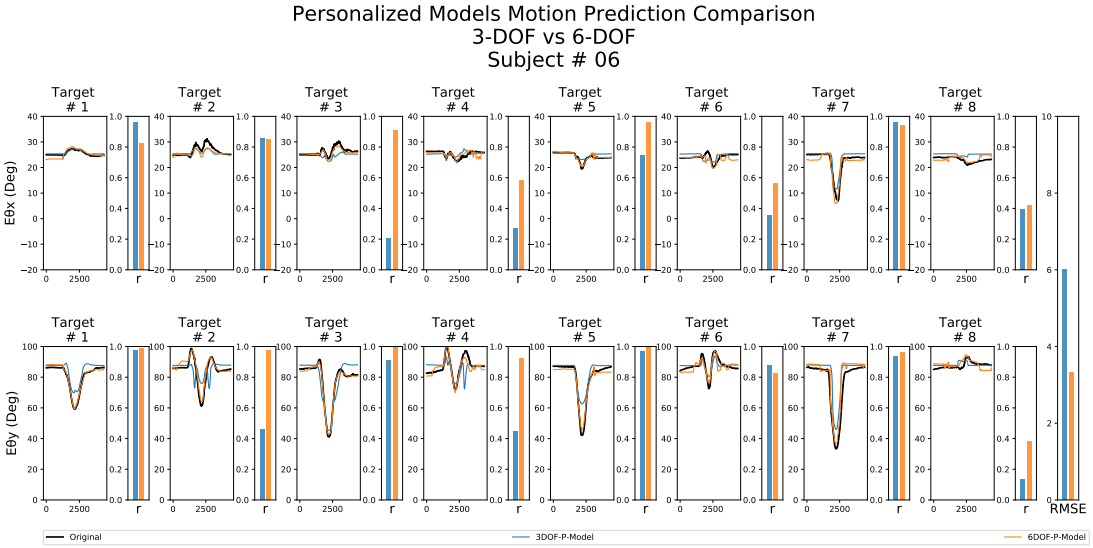

Figure 4.4: Performance Analysis of Predictive Models: Comparing the *3DOF-P-Model* and *6DOF-P-Model* for one of the healthy subjects. The top row depicts the elbow's pronation-supination angle $E\theta_x$, while the bottom row illustrates the elbow's flexion-extension angle $E\theta_y$. The line graph visually represents the variation in joint angles during reaching movements toward each target point. Original joint angles are displayed in black, the estimations from the *3DOF-P-Model* are presented in blue, and the estimations from the *6DOF-P-Model* are depicted in orange. The adjacent bars represent the corresponding Pearson's correlation coefficient values for each comparison, with the overall ($RMSE$) value displayed in the bar graph in the last column.

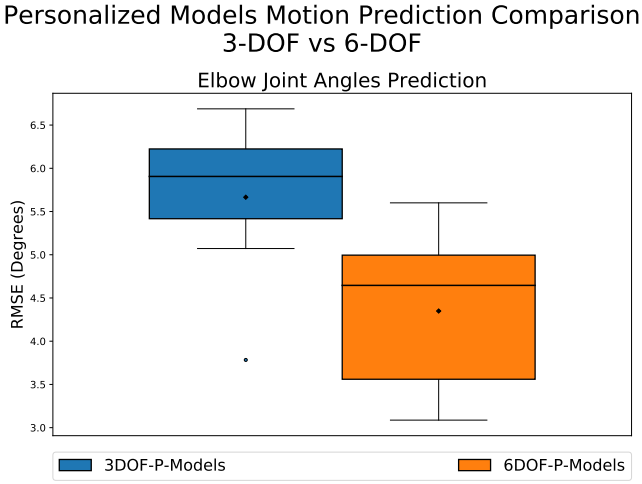

Figure 4.5: The Box Plot Illustrates the $RMSE$ Values for the *3DOF-P-Model* and the *6DOF-P-Model* Across All Subjects. The box size signifies the range encompassing 75% of the values, while the solid horizontal black line within the box denotes the median, and the black diamond marker indicates the mean value. Circular markers mark outliers, and the whiskers extend to display the maximum and minimum values. Smaller box sizes and lower $RMSE$ values correspond to improved prediction accuracy.

Table 4.1: Percentage breakdown of improvement comparing *3DOF-P-Models* and *6DOF-P-Models*.

Personalized Model Subject	RMSE Value 3DOF-P-Model	RMSE Value 6DOF-P-Model	Percentage Improvement
S1	5.76°	4.98°	13.58%
S2	3.78°	3.09°	18.40%
S3	6.69°	5.60°	16.26%
S4	5.91°	4.65°	21.34%
S5	6.43°	5.01°	22.05%
S6	6.02°	3.32°	44.81%
*Overall Mean	5.67°	4.35°	23.24%

4.3.2 Generic Models: Off-Line Evaluation

When contemplating an amputee, the feasibility of utilizing a predictive model trained with the user's own individual motion data to control the transhumeral prosthesis's elbow joint becomes impractical. In response to this challenge, we developed generic CNN-LSTM models (see Section 4.2.4), specifically the *G-Model* and *G-Model-AVG*. These models were devised by transforming reaching motion data recorded from healthy subjects into a training dataset meticulously adapted to train predictive models suitable for a diverse range of individuals.

We initially conducted an offline evaluation to assess the predictive performance of the generic CNN-LSTM models across different subjects. This involved providing the *G-Model* and *G-Model-AVG* with recorded arm reaching motion data from all six healthy subjects and analyzing the results of the predicted reaching motions. The results of the prediction performance analysis for one of the subjects using both the generic models are presented in Figure 4.6, showcasing the *3DOF-Model* (in blue) and the *6DOF-Model* (in orange).

It can be observed from Figures 4.6a and 4.6b that both the *G-Model* and *G-Model-AVG* were able to predict the elbow joint angle during the reaching movements towards all the target points in the virtual space. Additionally, as suggested by the similar Pearson's correlation coefficient "r" and the overall $RMSE$ values in Figure 4.6, both the generic models exhibited comparable performance.

Notably, in comparison to the *G-Model*, the *G-Model-AVG* was trained using a smaller subset of training data obtained by averaging the recorded motion data from all subjects. It demonstrated comparable performance while utilizing fewer resources and less training time. These results suggest that an averaged motion dataset still retains the required synergistic information and is sufficient for training a reliable predictive model.

Furthermore, we compared the fingertip position tracking of the right arm's middle finger recorded during the reaching tasks. This fingertip tracking data was obtained by visualizing each subject's original and predicted motion data in the Unity 3D simulation virtual workspace (see Section 4.2.5).

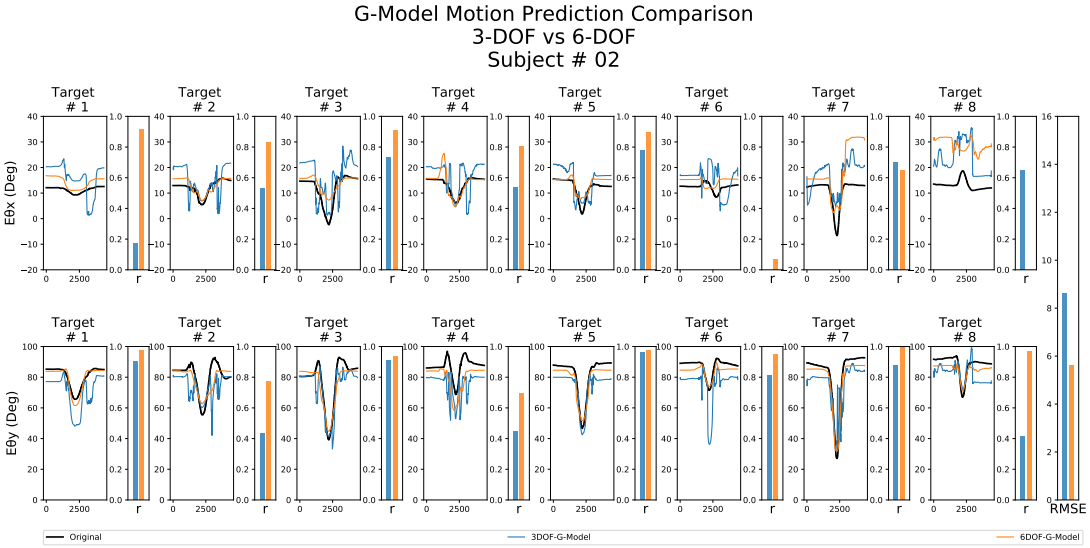

(a)

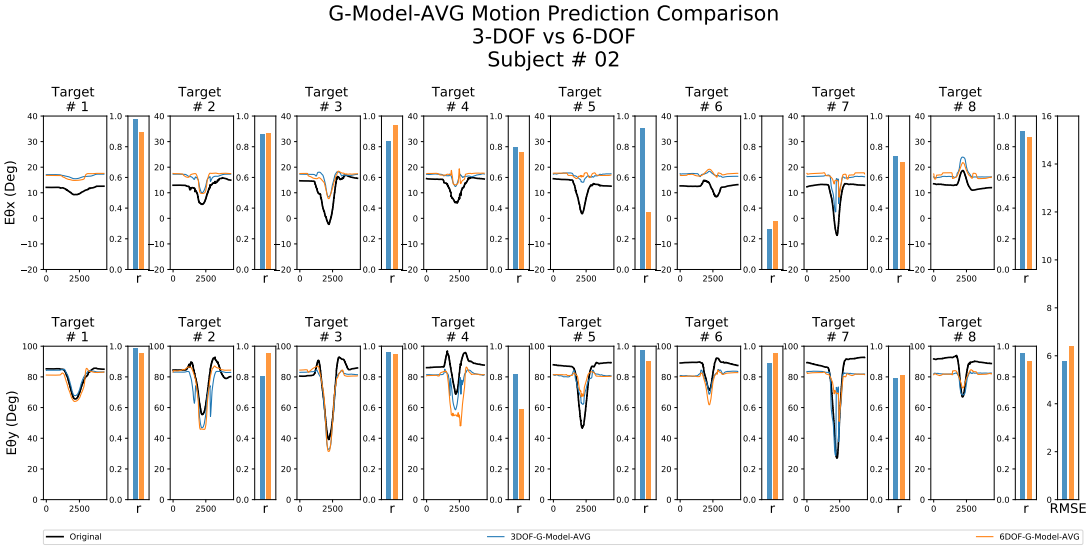

(b)

Figure 4.6: Performance Analysis for Offline Assessment of the Generic Models. (a) *G-Model*. (b) *G-Model-AVG*. The top row depicts the elbow's pronation-supination angle $E\theta_x$, while the bottom row illustrates the elbow's flexion-extension angle $E\theta_y$. The line graph visually represents the variation in joint angles during reaching movements toward each target point. Original joint angles are displayed in black, the estimations from the *3DOF-Model* are presented in blue, and the estimations from the *6DOF-Model* are depicted in orange. The adjacent bars represent the corresponding Pearson's correlation coefficient values for each comparison, with the overall ($RMSE$) value displayed in the bar graph in the last column.

Figure 4.7 presents the results of the fingertip tracking comparison during reaching movements for all six healthy subjects using both generic models, highlighting the *3DOF-Model* (in blue) and the *6DOF-Model* (in orange). The line graph portrays the variation in the right arm's middle finger's fingertip position throughout the reaching movements toward each target point (depicted in green). The fingertip

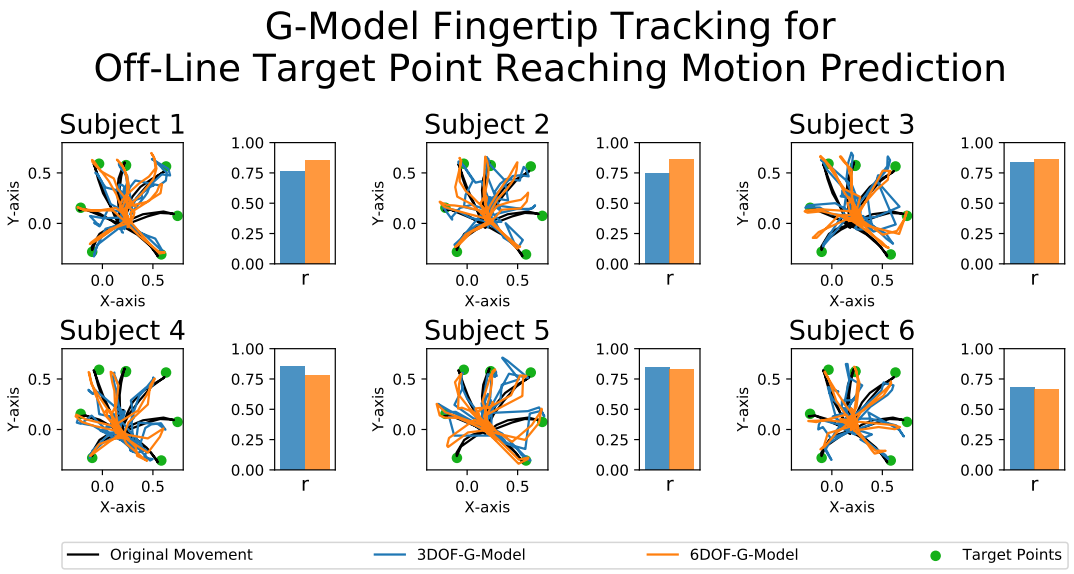

(a)

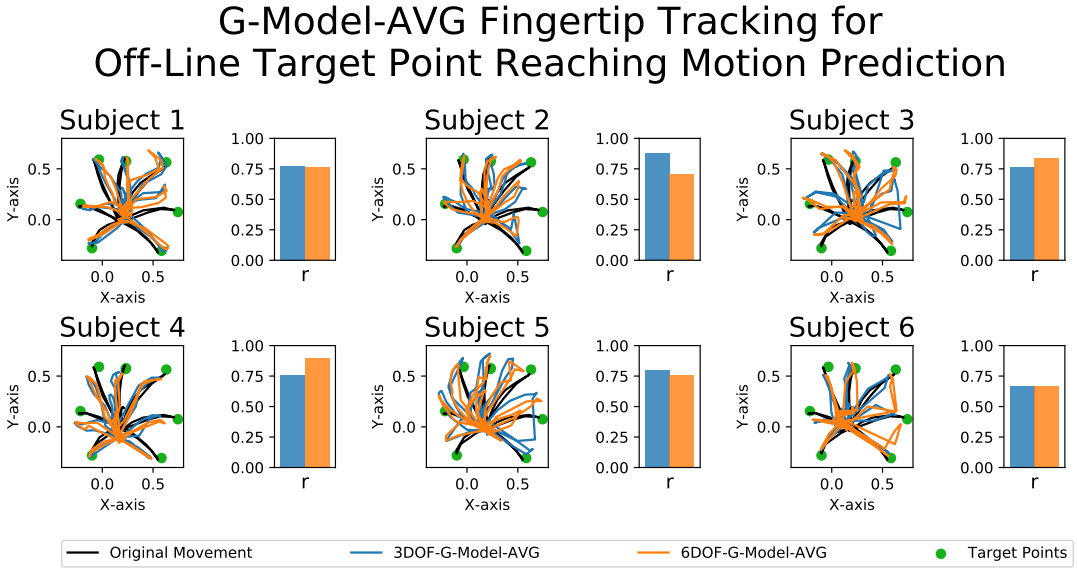

(b)

Figure 4.7: Fingertip Tracking Comparison for Offline Assessment of the Generic Models. (a) *G-Model*. (b) *G-Model-AVG*. Each line plot represents the tracking of fingertip position along the x-y plane toward individual target points (depicted in green) for each subject. Fingertip tracking for the subject's original motion is presented in black, while that for the predicted motion by the *3DOF-G-Model-AVG* and *6DOF-G-Model-AVG* is shown in blue and orange, respectively. The calculated Pearson's correlation coefficient "r" is visualized as a bar graph adjacent to the plots.

tracking is depicted along the x-y axis for simplicity. Concurrently, the adjacent bars provide insight into the calculated Pearson's correlation coefficient "r" values, offering a comparison between the fingertip position tracking for the subject's original (depicted in black) and predicted arm-reaching movements.

The predicted motion data from both generic models demonstrated effective reaching movements toward all the target points in the virtual workspace. The computed r values (Figures 4.7a and 4.7b)) indicate a reasonably accurate performance across all subjects and exhibit comparable trends for both generic models. These findings suggest that both the *G-Model* and *G-Model-AVG* display slight variations in prediction accuracy across multiple subjects and are robust to inter-individual variability. Notably, the simulation's humanoid actor relied exclusively on shoulder and elbow joint angular data to simulate reaching movements without integrating compensatory actions like trunk and shoulder displacements.

4.3.3 Generic Models: Validation on Amputee User

Lastly, we conducted real-time validation of the generic models on an amputee participant with a right arm transhumeral amputation. The amputee user actively interacted with the virtual workspace, controlling the movements of the humanoid actor in real-time through the Perception Neuron Pro sensor and the Oculus Quest VR headset, as illustrated in the experimental setup presented in Figure 4.8. The VR platform (see section 4.2.1) was slightly modified to integrate the generic CNN-LSTM predictive models into the Python intermediate module. This enabled real-time prediction of the user's elbow joint angles, allowing the execution of reaching movement tasks within the virtual workspace.

Overall, with no prior experience in the task or familiarity with the apparatus, our synergy-spaced methodology-based generic CNN-LSTM predictive models enabled the disabled participant to successfully execute reaching movements towards all the target points in the virtual workspace. Figure 4.9 illustrates the real-time

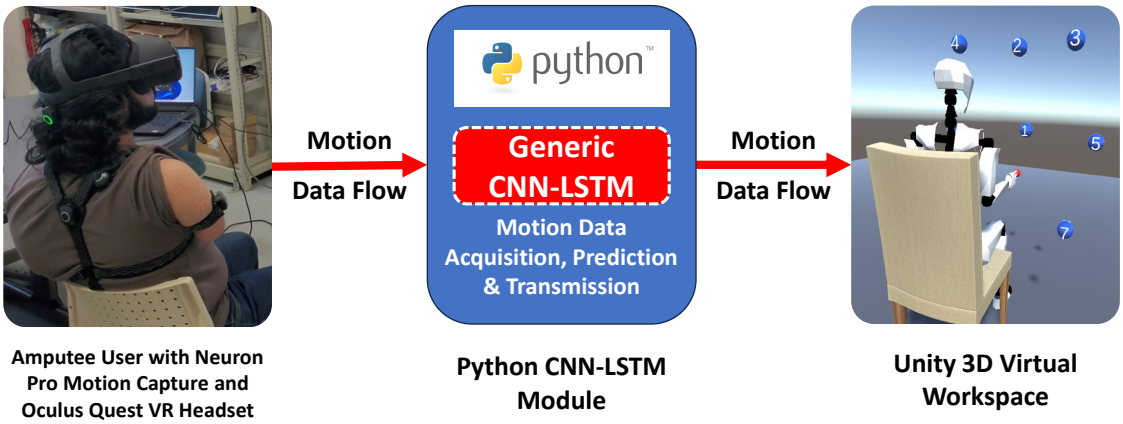

Figure 4.8: Modified Virtual Reality (VR) platform architecture for Validation on Amputee User: The Neuron Pro system processes motion data and communicates with the Python CNN-LSTM module. The module receives the user's available joint angular motion data, while the generic CNN-LSTM models simultaneously predict the corresponding elbow joint angles. These predicted angles are then transmitted to the Unity 3D simulation for real-time reaching movements toward the target points in the virtual workspace.

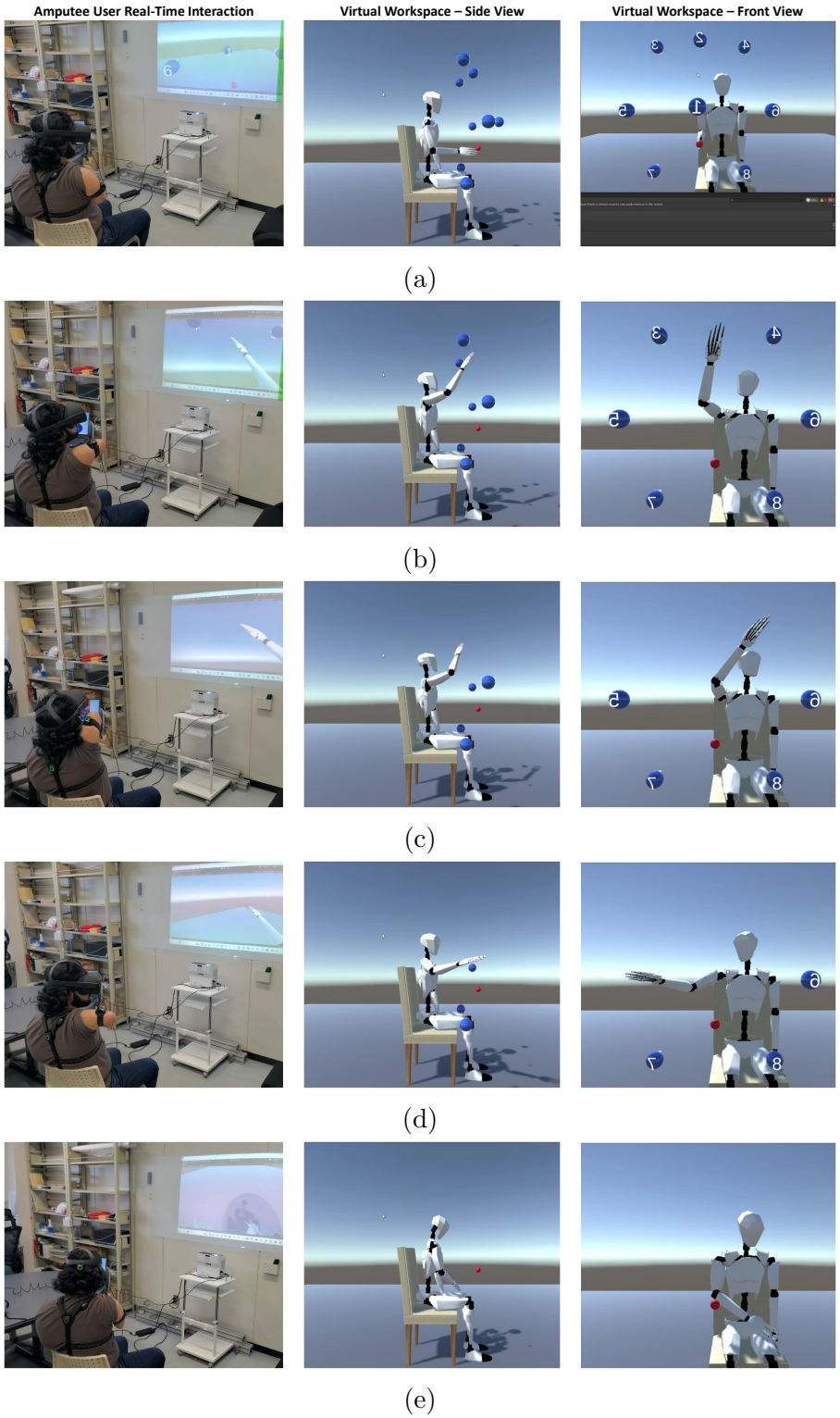

Figure 4.9: Validation with Amputee User: A right-arm transhumeral amputee actively executing reaching movements towards target points (depicted as blue spheres) within the virtual workspace in real-time. The target point disappears upon contact with the humanoid actor's finger. (a) Rest/Starting Pose. (b) Reaching Target Point 2. (c) Reaching Target Point 4. (d) Reaching Target Point 5. (e) Reaching Target Point 8.

interaction of the amputee participant with the virtual workspace, engaging in and executing reaching movements.

The amputee subject reported a smooth interaction with the virtual workspace, and the movement of the humanoid actor's arm appeared to mimic natural arm movements during the execution of reaching tasks. We compared the fingertip position tracking recorded during the reaching tasks to assess the similarity between the amputee user's reaching motion prediction and the natural arm movements recorded from healthy subjects. In this analysis, we compared the fingertip tracking during real-time motion prediction for the amputee user with the averaged motion dataset created from the recorded data of all healthy participants.

Figure 4.10 illustrates the results of the fingertip tracking comparison for real-time predictions of reaching movements for the amputee subject using both the *G-Model* and *G-Model-AVG* generic CNN-LSTM models. The *3DOF-Model* is represented in blue, while the *6DOF-Model* is depicted in orange. The line graph captures the variation in the fingertip position of the right arm's middle finger dur-

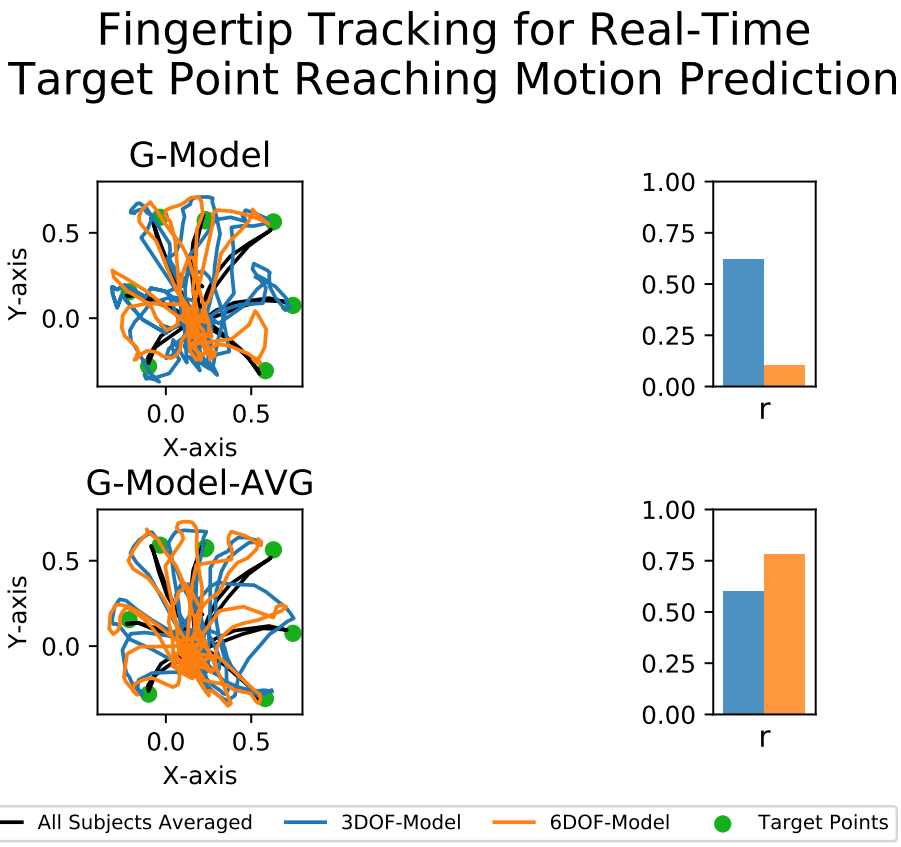

Figure 4.10: Fingertip Tracking Comparison for Real-Time Assessment of the Generic Models. Each line plot represents the tracking of fingertip position along the x-y plane toward individual target points (depicted in green) for the amputee subject. Fingertip tracking for all healthy subjects averaged motion is presented in black, while that for the predicted motion by the *3DOF* and *6DOF* generic models is shown in blue and orange, respectively. The calculated Pearson's correlation coefficient "r" is visualized as a bar graph adjacent to the plots.

ing reaching movements toward each target point (depicted in green). The fingertip tracking is presented along the x-y axis for clarity. Simultaneously, the adjacent bars provide insights into the calculated Pearson's correlation coefficient "r" values, comparing the fingertip position tracking for the averaged reaching motion data from all healthy subjects (depicted in black) with the predicted arm-reaching movements for the amputee user.

In each scenario, the amputee user successfully reached and touched all the target points in the virtual workspace. The calculated r values indicated a significant correlation with the averaged reaching motion data in all instances, except for the 6-DOF-G-Model. This discrepancy was attributed to the humanoid arm's failure to properly return to the rest pose at the conclusion of the reaching tasks.

4.4 Discussion

We presented a residual shoulder motion-based prediction of the elbow joint angle during extensive arm-reaching movements for transhumeral prosthesis control. Our experiments and validation were conducted on a VR-based platform, initially employed for data acquisition from healthy human subjects and later utilized to verify the efficacy of the trained CNN-LSTM predictive models. Our evaluation results highlight the effectiveness of incorporating head orientation information with shoulder joint angular data as training inputs, enhancing the performance of the predictive models. Moreover, training the predictive model with an averaged motion dataset demonstrated comparable performance across multiple subjects, offering efficiency gains in computing resources and training time while retaining essential synergistic characteristics of reaching movements. Lastly, real-time evaluation with a transhumeral amputee user successfully executing reaching tasks toward all target points in the virtual workspace validates the potential of our methodology and the VR-based platform.

We evaluated the integration of head orientation data ($H\theta_x$, $H\theta_y$ & $H\theta_z$) with residual shoulder joint angular motion data ($S\theta_x$, $S\theta_y$ & $S\theta_z$) by training personalized predictive models for each healthy subject: the *3DOF-P-Model* and the *6DOF-P-Model*, featuring distinct input data configurations. The predictive performance of these *P-Models* was scrutinized by comparing and correlating the results with the original motion data obtained from each subject. Employing metrics such as Pearson's correlation coefficient "r" and $RMSE$ values, we gauged the linearity and average difference between the estimated and actual joint angular values.

Pearson's correlation coefficient analysis revealed a strong similarity between the predicted and original motion data for individual subjects. However, the considerable difference in overall $RMSE$ values across all subjects underscored the superior performance of the *6DOF-P-Model*. These findings highlight the nuanced coordination between head orientation and arm motion during extensive reaching movements, emphasizing the effectiveness of integrating head orientation data to enhance the accuracy of predictive models.

We used arm-reaching motion data from all healthy subjects to train the generic predictive models: the *G-Model* and the *G-Model-AVG*. Subsequently, we assessed their performance across all subjects. Notably, the *G-Model-AVG* was trained using the averaged human motion data from all participants, resulting in a model that required approximately three times fewer computational resources and training time.

Both generic models demonstrated accurate predictions of elbow joint motion across all subjects, showcasing their robustness in accommodating inter-subject variability. Their performance was similar, supported by comparable Pearson's correlation coefficient values and minor differences in overall $RMSE$ values. This result suggests that the averaged motion data from multiple subjects retained essential synergistic patterns of reaching movements, facilitating the effective training of generic predictive models while concurrently reducing computational and timing requirements.

In the conclusive phase, we validated the performance of the generic models on an amputee participant. The subject, a right-arm transhumeral amputee, interacted with and controlled a humanoid actor by strapping on a few sensors on his body. He executed reaching movements toward specified target points in a virtual workspace while the generic model concurrently predicted the motion of his amputated elbow in real-time. We conducted a visual analysis of the predicted motion and a comparative examination of fingertip tracking during the target-reaching movements to assess the accuracy of the predictions.

The results demonstrated the amputee user's adeptness in reaching and touching all designated target points in the virtual workspace without prior experience in the task or familiarity with the apparatus. Although variations were observed in the fingertip tracking comparison, the overall performance of both models remained similar, substantiated by comparable Pearson's correlation coefficient values. These findings underscore the potential efficacy of a synergy-based arm joint coordination strategy for predicting elbow joint motion and endorse the viability of VR-based platforms for developing and validating transhumeral prosthesis control.

This study explored real-time prediction of elbow joint motion during extensive arm-reaching activities within a 3D virtual workspace for transhumeral prosthesis control. Moving forward, our endeavor is to elevate the precision and scope of elbow joint motion prediction for transhumeral prosthesis, encompassing a more extensive range of dynamic arm movements and scenarios within the VR-based platform.

4.5 Conclusions

This study introduces the potential of synergistic movement data-based prediction of elbow joint motion and the effectiveness of a virtual reality-based platform for evaluating strategies for transhumeral prosthesis control.

We presented a framework for real-time prediction and evaluation of elbow joint motion during extensive arm-reaching activities. Our analysis confirmed that integrating head orientation data with shoulder joint angular data enhances predictive model performance. The personalized predictive models, trained with combined head orientation data, exhibited an average improvement of approximately 23.24% in prediction accuracy. Our results also emphasize the advantage of using averaged motion data from all healthy participants, which can offer comparable performance while significantly reducing overall computational and training time. Lastly, successful validation on an amputee subject performing reaching movements towards target points in a virtual workspace demonstrates the potential efficacy of our approach.

These findings carry significant implications for creating comprehensive virtual workspaces with diverse arm movements covering various activities for validating and advancing strategies in transhumeral prosthesis control.

Chapter 5

Conclusion and Future Work

5.1 Summary

In this thesis, three distinct studies have been conducted, stemming from the initial objective of developing and evaluating an intuitive strategy for controlling the elbow joint of a transhumeral prosthesis during arm-reaching movements. These studies are interrelated and revolve around the concept of motor synergies, with the aim of generating prosthetic elbow joint motion that closely resembles natural human movement. We utilized residual shoulder motion-based, non-invasive, intuitive, and easy-to-acquire joint angular data signals as control input and training data for our predictive models.

Our methodology delves into the synergistic inter-joint coordination of the human arm during reaching movements, specifically focusing on simultaneously controlling two degrees of freedom (DOFs) of the elbow joint. Leveraging synergy allowed us to develop more transferable predictive models capable of operating across multiple subjects with minimal loss in performance. The inclusion of DRL algorithms was pivotal in our exploration, where we investigated the emergence of synergy to generate synthetic arm-reaching motion data. This supplementation aimed to diversify and enrich the training data, ultimately enhancing the performance of the predictive models. Lastly, we ventured into the realm of Unity 3D simulation to create a virtual reality-based real-time interactive workspace to validate the effectiveness of our methodology through real-time elbow joint motion prediction for a transhumeral amputee user.

In Chapter 2, with the aim of enhancing the controllability of a transhumeral prosthesis, we conducted a study focusing on the transferability of control across users. We introduced synergy-space neural networks as a transferable model for predicting elbow joint motion based on residual shoulder motion during arm-reaching movements in the horizontal plane. We employed LSTM RNN to implement the proposed synergy-space approach. This approach extracts synergistic information from the motion data, explicitly incorporating only the most significant synergies into the learning process of the predictive model. This facilitated more precise and efficient

training of the predictive model. To validate the proposed approach and its efficient learning capability, we conducted a detailed cross-subject evaluation between the performance of predictive models trained using the synergy-space methodology and those employing the conventional direct estimation methodology.

For the transferability analysis, we utilized RMSE, and the statistically significant ANOVA was followed up with the Tukey HSD. The results indicated that the proposed synergy-space method exhibited approximately 40% less variation in the RMSE compared to the direct estimation method, showcasing its capability to manage inter-individual variabilities. This observation suggests that the synergy-space neural network can capture specific features common to arm movement tasks, given that the predictive model is trained using the most significant synergy components. Furthermore, due to the shared nature of these synergies among different subjects performing similar tasks, the synergy-space neural network demonstrated improved cross-subject transferability. This underscores the potential of the proposed synergy-space approach to develop a transferable model for prosthesis control.

In Chapter 3, our focus was on addressing the challenge of obtaining a substantial amount of training motion data to effectively train predictive models, as large quantities of human motion data collected from different subjects for various activities of daily living are required for this purpose. To overcome this, we introduced a DRL-based motion cloning framework that employed a 7-DOF robot arm model in a mujoco simulation to generate synthetic motion data. The underlying idea was to enable the simulated robot arm to learn and replicate arm-reaching movements, harnessing the capabilities of DRL algorithms to produce natural and human-like motion in simulated humanoid agents. By extracting motion data from the shoulder and elbow joints of the simulated arm, we could effectively supplement and diversify the training data, thereby enhancing the predictive model's ability to generalize across different subjects.

Our analysis verified that the synthetic motion data closely mirrored the characteristics of human arm motion data. Pearson's correlation coefficient analysis revealed a robust similarity between the synthetic motion data and the real motion data collected from human subjects. These findings underscore the effectiveness of DRL-based synthetic motion data in capturing the synergistic patterns of arm-reaching movements, essentially serving as an additional subject within the experiment. We delved into the impact of integrating real motion data with synthetic motion data, specifically for reaching movements towards new target points, as part of the training process to enhance the performance of predictive models. The results indicate that the predictive model trained using the augmented motion dataset exhibited improved performance compared to the model trained solely on real motion data when predicting motion toward new targets. This emphasizes the potential of synthetically generated motion data through DRL-based simulation to faithfully replicate human-like synergistic arm movements and underscores its role in augmenting motion data to enhance the performance and robustness of predictive models.

In Chapter 4, our focus shifted towards the real-time prediction of elbow joint motion and the validation of our proposed synergy-space approach on a transhumeral amputee user. Up to this point, our work had primarily involved healthy subjects, and the assessment of predictive models had been conducted offline using recorded motion datasets. Recognizing the challenges inherent in clinical trials for transhumeral prostheses, we devised a virtual reality (VR)-based interactive framework specifically tailored for real-time validation and evaluation of the predictive models. Within this framework, amputee users can easily affix sensors to their bodies to control a humanoid actor within a virtual workspace, requiring minimal preparation for testing the control strategy. The overarching concept involves establishing a platform for initially acquiring motion data from healthy subjects. This data is then utilized to train predictive models for transhumeral prosthesis elbow control, with subsequent validation of their efficacy on amputee subjects executing arm-reaching tasks in the virtual workspace.

We trained generic predictive models based on the synergy-space approach, using recorded motion data from healthy human subjects performing extensive arm-reaching movements towards targets in a 3D virtual workspace. The performance of the predictive models was initially assessed offline, utilizing motion data from the healthy subjects. The results of the elbow joint motion prediction demonstrated sufficient accuracy and robustness across all subjects, signifying the effectiveness of the predictive model's training. Subsequently, we validated the performance of the trained predictive model on a participant with a right arm transhumeral amputation. Remarkably, despite the participant lacking prior experience in the task and familiarity with the apparatus, our synergy-space methodology-based predictive model facilitated the successful execution of reaching movements toward all target points in the virtual workspace. These findings highlight the potential efficacy of the synergy-space neural network strategy for predicting elbow joint motion and endorse the viability of VR-based platforms for the development and validation of transhumeral prosthesis control.

5.2 Contribution

The primary contributions of this thesis include:

- The introduction of the synergy-space neural network as a transferable model for predicting elbow joint motion in transhumeral prosthesis control.
- The illustration of the transferability characteristics of the synergy-space neural network through a comprehensive cross-subject evaluation.
- The proposal of a DRL-based motion cloning framework for the generation of synthetic motion data.
- The demonstration of motion data augmentation to enhance the performance and robustness of predictive models.

- The creation of a VR-based interactive workspace for real-time validation and evaluation of predictive models.
- The demonstration of real-time elbow joint motion prediction for a transhumeral amputee user during arm-reaching movements in the virtual workspace.

5.3 Future Work

There are several improvements and further investigations that can be done to the studies carried out in this thesis.

Firstly, the focal point of all the studies has been the control of elbow joint motion during target-reaching tasks, a fundamental aspect of transhumeral prosthesis control. However, there is potential for future work to diversify the spectrum of tasks. Incorporating activities such as drinking from a glass or engaging in specific exercises would present a significant challenge, demanding itricate control of multiple joints in the transhumeral prosthesis. Training a generalized predictive model for such diverse tasks would be a formidable yet valuable undertaking.

Another area for improvement involves refining the DRL-based motion cloning framework to handle more intricate movements. While the current simulation employs a 7-DOF arm agent to replicate arm-reaching motions, accurately mimicking complex movements may necessitate the use of a full-body agent. Additionally, exploring and designing effective reward functions for the DRL algorithm is crucial to ensure optimal learning and convergence. Hence, further research is imperative to exploit the potential of synthetic motion data generation fully.

In this thesis, our emphasis was on the concurrent control of two DOFs of the elbow joint, specifically pronation-supination and flexion-extension. While regulating these two DOFs proves adequate for many daily tasks, an alternative avenue for exploration involves expanding control to include manipulation of the DOFs of the wrist joint. This extension would be essential for more intricate movement control, such as playing a violin. The concept underlying this extended control is to empower amputee users to either sustain or cultivate hobbies that can help foster self-esteem and social inclusion.

Finally, the most crucial aspect is the validation of the control strategy. In our thesis, we constructed a VR platform for the real-time validation of our approach with an amputee subject. This platform can be enhanced further to encompass a variety of arm movements and, in general, provide a more immersive experience for users. However, real-world validation on transhumeral prostheses is indispensable. A potential avenue for future work involves creating a modular transhumeral prosthesis that users can easily wear without special preparations, facilitating the testing of the control strategy.

Bibliography

[1] D. Latour, "Advances in upper extremity prosthetic technology: Rehabilitation and the interprofessional team," *Current Physical Medicine and Rehabilitation Reports*, vol. 10, pp. 71–76, 2022. DOI: 10.1007/s40141-022-00342-x.

[2] K. Ziegler-Graham, E. J. MacKenzie, P. L. Ephraim, T. G. Travison, and R. Brookmeyer, "Estimating the prevalence of limb loss in the united states: 2005 to 2050," *Archives of Physical Medicine and Rehabilitation*, vol. 89, no. 3, pp. 422–429, 2008. DOI: 10.1016/j.apmr.2007.11.005.

[3] P. Blog, *Upper limb amputation levels*, 2022. [Online]. Available: https://www.prostheticsindia.org/upper-limb-amputation/.

[4] C. Francesca, C. A. Lisa, S. Rinaldo, *et al.*, "Literature review on needs of upper limb prosthesis users," *Frontiers in Neuroscience*, vol. 10, p. 209, 2016. DOI: 10.3389/fnins.2016.00209.

[5] T. P. Sheehan and G. C. Gondo, "Impact of limb loss in the united states," *Physical medicine and rehabilitation clinics of North America*, vol. 25, no. 1, pp. 9–28, 2014. DOI: 10.1016/j.pmr.2013.09.007.

[6] P. J. Kyberd and W. Hill, "Survey of upper limb prosthesis users in sweden, the united kingdom and canada," *Prosthetics and Orthotics International*, vol. 35, pp. 234–241, 2011. DOI: 10.1177/0309364611409099.

[7] D. J. Atkins, D. C. Y. Heard, and W. H. Donovan, "Epidemiologic overview of individuals with upper-limb loss and their reported research priorities," *Journal of Prosthetics and Orthotics*, 1996. DOI: 10.1097/00008526-199600810-00003.

[8] A. Manfredo and M. Henning, "Control capabilities of myoelectric robotic prostheses by hand amputees: A scientific research and market overview," *Frontiers in Systems Neuroscience*, vol. 9, p. 162, 2015. DOI: 10.3389/fnsys.2015.00162.

[9] W. Schweitzer, M. J.Thali, and D. Egger, "Case-study of a user-driven prosthetic arm design: Bionic hand versus customized body-powered technology in a highly demanding work environment," *Journal of NeuroEngineering and Rehabilitation*, 2018. DOI: 10.1186/s12984-017-0340-0.

[10] B.Phillips, G.Zingalis, S.Ritter, and K.Mehta, "A review of current upper-limb prostheses for resource constrained settings," *IEEE Global Humanitarian Technology Conference (GHTC)*, pp. 52–58, 2015. DOI: 10.1109/GHTC.2015.7343954.

[11] L. Resnik, S. L. Klinger, and K. Etter, "The deka arm: Its features, functionality, and evolution during the veterans affairs study to optimize the deka arm," *Prosthetics and Orthotics International*, vol. 38, pp. 492–504, 2014. DOI: 10.1177/0309364613506913.

[12] B. N. Perry, C. W. Moran, R. S. Armiger, P. F. Pasquina, J. W. Vandersea, and J. W. Tsao, "Initial clinical evaluation of the modular prosthetic limb," *Frontiers in Neurology*, vol. 9, p. 153, 2018. DOI: 10.3389/fneur.2018.00153.

[13] M. S. Johannes, J. D. Bigelow, J. M. Burck, S. D. Harshbargerx, M. V. Kozlowski, and T. V. Doren, "An overview of the developmental process for the modular prosthetic limb," *Johns Hopkins APL Technical Digest (Applied Physics Laboratory)*, vol. 30, pp. 207–216, 2011.

[14] N. Jiang, S. Dosen, K. Muller, and D. Farina, "Myoelectric control of artificial limbs—is there a need to change focus? [in the spotlight]," *IEEE Signal Processing Magazine*, vol. 29, pp. 152–150, 2012. DOI: 10.1109/MSP.2012.2203480.

[15] Ottobock, *Dynamicarm*. [Online]. Available: https://shop.ottobock.us/Prosthetics/Upper-Limb-Prosthetics/Myoelectric-Elbows/DynamicArm-Elbow/c/2125.

[16] Ottobock, *Ergoarm*. [Online]. Available: https://shop.ottobock.us/Prosthetics/Upper-Limb-Prosthetics/Myoelectric-Elbows/ErgoArm-Elbow/c/2127.

[17] K. Englehart and B. Hudgins, "A robust, real-time control scheme for multifunction myoelectric control," *IEEE Transactions on Biomedical Engineering*, vol. 50, pp. 848–854, 2003. DOI: 10.1109/TBME.2003.813539.

[18] E. Biddiss and T. Chau, "Upper-limb prosthetics: Critical factors in device abandonment," *American Journal of Physical Medicine Rehabilitation*, vol. 86, pp. 977–987, 2007. DOI: 10.1097/PHM.0b013e3181587f6c.

[19] E. Biddiss and T. Chau, "Upper limb prosthesis use and abandonment: A survey of the last 25 years," *Prosthetics and Orthotics International*, vol. 31, pp. 236–257, 2007. DOI: 10.1080/03093640600994581.

[20] M. Kuttuva, G. Burdea, J. Flint, and W. Craelius, "Manipulation practice for upper-limb amputees using virtual reality," *Presence*, vol. 14, no. 2, pp. 175–182, 2005. DOI: 10.1162/1054746053967049.

[21] D. Sierra Gonzalez and C. Castellini, "A realistic implementation of ultrasound imaging as a human-machine interface for upper-limb amputees," *Frontiers in Neurorobotics*, vol. 7, p. 17, 2013. DOI: 10.3389/fnbot.2013.00017.

[22] J. Silva, W. Heim, and T. Chau, "A self-contained, mechanomyography-driven externally powered prosthesis," *Archives of Physical Medicine and Rehabilitation*, vol. 86, no. 10, pp. 2066–2070, 2005. DOI: 10.1016/j.apmr.2005.03.034.

[23] M. Hayashibe and S. Shimoda, "Synergetic learning control paradigm for redundant robot to enhance error-energy index," *IEEE Transactions on Cognitive and Developmental Systems*, vol. 10, no. 3, pp. 573–584, 2018. DOI: 10.1109/TCDS.2017.2697904.

[24] Y. Losier, K. Englehart, and B. Hudgins, "Evaluation of shoulder complex motion-based input strategies for endpoint prosthetic-limb control using dual-task paradigm," *The Journal of Rehabilitation Research and Development*, vol. 48, no. 6, p. 669, 2011. DOI: 10.1682/jrrd.2010.08.0165.

[25] R. Lipschutz, B. Lock, J. Sensinger, A. Schultz, and T. Kuiken, "Use of two-axis joystick for control of externally powered shoulder disarticulation prostheses," *The Journal of Rehabilitation Research and Development*, vol. 48, no. 6, pp. 719–737, 2011. DOI: 10.1682/JRRD.2010.08.0161.

[26] F. Lacquaniti and J. F. Soechting, "Coordination of arm and wrist motion during a reaching task," *Journal of Neuroscience*, vol. 2, no. 4, pp. 399–408, 1982. DOI: 10.1523/JNEUROSCI.02-04-00399.1982.

[27] A. Roby-Brami, N. Bennis, M. Mokhtari, and P. Baraduc, "Hand orientation for grasping depends on the direction of the reaching movement," *Brain Research*, vol. 869, no. 1, pp. 121–129, 2000. DOI: 10.1016/S0006-8993(00)02378-7.

[28] M. Desmurget and C. Prablanc, "Postural control of three-dimensional prehension movements," *Journal of Neurophysiology*, vol. 77, pp. 452–464, 1997. DOI: 10.1152/jn.1997.77.1.452.

[29] J. Soechting and F. Lacquaniti, "Invariant characteristics of a pointing movement in man," *Journal of Neuroscience*, vol. 1, pp. 710–720, 1981. DOI: 10.1523/JNEUROSCI.01-07-00710.1981.

[30] R. R. Kaliki, R. Davoodi, and G. E. Loeb, "Evaluation of a noninvasive command scheme for upper-limb prostheses in a virtual reality reach and grasp task," *IEEE Transactions on Biomedical Engineering*, vol. 60, no. 3, pp. 792–802, 2013. DOI: 10.1109/TBME.2012.2185494.

[31] S. Iftime, L. Egsgaard, and M. Popovic, "Automatic determination of synergies by radial basis function artificial neural networks for the control of a neural prosthesis," *IEEE Transactions on Neural Systems and Rehabilitation Engineering*, vol. 13, no. 4, pp. 482–489, 2005. DOI: 10.1109/TNSRE.2005.858458.

[32] M. Popovic and D. Popovic, "Cloning biological synergies improves control of elbow neuroprostheses," *IEEE Engineering in Medicine and Biology Magazine*, vol. 20, no. 1, pp. 74–81, 2001. DOI: 10.1109/51.897830.

[33] E. Bizzi and V. C. Cheung, "The neural origin of muscle synergies," *Frontiers in Computational Neuroscience*, vol. 7, 2013. DOI: 10.3389/fncom.2013.00051.

[34] M. Turvey, "Action and perception at the level of synergies," *Human Movement Science*, vol. 26, pp. 657–697, 2007. DOI: 10.1016/j.humov.2007.04.002.

[35] A. de Rugy, G. E. Loeb, and T. J. Carroll, "Are muscle synergies useful for neural control?" *Frontiers in Computational Neuroscience*, vol. 7, 2013. DOI: 10.3389/fncom.2013.00019.

[36] M. Tagliabue, A. L. Ciancio, T. Brochier, S. Eskiizmirliler, and M. A. Maier, "Differences between kinematic synergies and muscle synergies during two-digit grasping," *Frontiers in Human Neuroscience*, vol. 9, 2015. DOI: 10.3389/fnhum.2015.00165.

[37] A. d'Avella, A. Portone, L. Fernandez, and F. Lacquaniti, "Control of fast-reaching movements by muscle synergy combinations," *Journal of Neuroscience*, vol. 26, no. 30, pp. 7791–7810, 2006. DOI: 10.1523/JNEUROSCI.0830-06.2006.

[38] M. C. Tresch and A. Jarc, "The case for and against muscle synergies," *Current Opinion in Neurobiology*, vol. 19, pp. 601–607, 2009. DOI: 10.1016/j.conb.2009.09.002.

[39] N. Dominici, Y. P. Ivanenko, G. Cappellini, *et al.*, "Locomotor primitives in newborn babies and their development," *Science*, vol. 334, no. 6058, pp. 997–999, 2011. DOI: 10.1126/science.1210617.

[40] J. Chai and M. Hayashibe, "Motor synergy development in high-performing deep reinforcement learning algorithms," *IEEE Robotics and Automation Letters*, vol. 5, no. 2, pp. 1271–1278, 2020. DOI: 10.1109/LRA.2020.2968067.

[41] T. Bockemühl, N. F. Troje, and V. Dürr, "Inter-joint coupling and joint angle synergies of human catching movements," *Human Movement Science*, vol. 29, no. 1, pp. 73–93, 2010. DOI: 10.1016/j.humov.2009.03.003.

[42] M. L. Latash, A. S. Aruin, and V. M. Zatsiorsky, "The basis of a simple synergy: Reconstruction of joint equilibrium trajectories during unrestrained arm movements," *Human Movement Science*, vol. 18, pp. 3–30, 1999. DOI: 10.1016/S0167-9457(98)00029-3.

[43] N. Lambert-Shirzad, V. der Loos, and H. F. Machiel, "On identifying kinematic and muscle synergies: A comparison of matrix factorization methods using experimental data from the healthy population," *Journal of Neurophysiology*, vol. 117, pp. 290–302, 2017. DOI: 10.1152/jn.00435.2016.

[44] A. Scano, L. Dardari, F. Molteni, H. Giberti, L. M. Tosatti, and A. d'Avella, "A comprehensive spatial mapping of muscle synergies in highly variable upper-limb movements of healthy subjects," *Frontiers in Physiology*, vol. 10, 2019. DOI: 10.3389/fphys.2019.01231.

[45] S. Tang, M. Barsotti, F. Stroppa, A. Frisoli, X. Wu, and W. Hou, "Upper limb joint angular velocity synergies of human reaching movements," *2018 IEEE International Conference on Cyborg and Bionic Systems (CBS)*, pp. 641–646, 2018. DOI: 10.1109/CBS.2018.8612235.

[46] E. Chiovetto, A. D'Avella, and M. Giese, "A unifying framework for the identification of motor primitives," *arXiv preprint 1603.06879*, 2016.

[47] F. M. Ramos, A. d'Avella, and M. Hayashibe, "Identification of time-varying and time-scalable synergies from continuous electromyographic patterns," *IEEE Robotics and Automation Letters*, vol. 4, pp. 3053–3058, 2019. DOI: 10.1109/LRA.2019.2924854.

[48] S. Overduin, A. D'Avella, J. Roh, J. Carmena, and E. Bizzi, "Representation of muscle synergies in the primate brain," *The Journal of neuroscience : The official journal of the Society for Neuroscience*, vol. 35, 2015. DOI: 10.1523/JNEUROSCI.4302-14.2015.

[49] M. Merad, É. de Montalivet, A. Touillet, N. Martinet, A. Roby-Brami, and N. Jarrassé, "Can we achieve intuitive prosthetic elbow control based on healthy upper limb motor strategies?" *Frontiers in Neurorobotics*, vol. 12, p. 1, 2018. DOI: 10.3389/fnbot.2018.00001.

[50] S. Micera, J. Carpaneto, F. Posteraro, L. Cenciotti, M. Popovic, and P. Dario, "Characterization of upper arm synergies during reaching tasks in able-bodied and hemiparetic subjects," *Clinical Biomechanics*, vol. 20, pp. 939–946, 2005. DOI: 10.1016/j.clinbiomech.2005.06.004.

[51] D. T. Gibbons, M. D. O'riain, and S. Philippe-Auguste, "An above-elbow prosthesis employing programmed linkages," *IEEE Transactions on Biomedical Engineering*, vol. BME-34, pp. 493–498, 1987. DOI: 10.1109/TBME.1987.325978.

[52] R. R. Kaliki, R. Davoodi, and G. E. Loeb, "Prediction of distal arm posture in 3-d space from shoulder movements for control of upper limb prostheses," *Proceedings of the IEEE*, vol. 96, no. 7, pp. 1217–1225, 2008. DOI: 10.1109/JPROC.2008.922591.

[53] M. Merad, A. Roby-Brami, and N. Jarrassé, "Towards the implementation of natural prosthetic elbow motion using upper limb joint coordination," *2016 6th IEEE International Conference on Biomedical Robotics and Biomechatronics (BioRob)*, pp. 821–826, 2016. DOI: 10.1109/BIOROB.2016.7523729.

[54] A. Akhtar, N. Aghasadeghi, L. Hargrove, and T. Bretl, "Estimation of distal arm joint angles from emg and shoulder orientation for transhumeral prostheses," *Journal of Electromyography and Kinesiology*, vol. 35, pp. 86–94, 2017. DOI: 10.1016/j.jelekin.2017.06.001.

[55] C. Olah, *Understanding lstm networks*, 2015. [Online]. Available: https://colah.github.io/posts/2015-08-Understanding-LSTMs/.

[56] M. Phi, *Illustrated guide to lstm's and gru's: A step by step explanation*, 2018. [Online]. Available: https://towardsdatascience.com/illustrated-guide-to-lstms-and-gru-s-a-step-by-step-explanation-44e9eb85bf21.

[57] R. S. Sutton and A. G. Barto, *Reinforcement Learning: An Introduction, Second Edition*. The MIT Press, 2018, ISBN: 9780262039246.

[58] K. Arulkumaran, M. P. Deisenroth, M. Brundage, and A. A. Bharath, "Deep reinforcement learning: A brief survey," *IEEE Signal Processing Magazine*, vol. 34, no. 6, pp. 26–38, 2017. DOI: 10.1109/MSP.2017.2743240.

[59] T. Haarnoja, A. Zhou, P. Abbeel, and S. Levine, "Soft actor-critic: Off-policy maximum entropy deep reinforcement learning with a stochastic actor," *Proceedings of the 35th International Conference on Machine Learning*, vol. 80, pp. 1861–1870, 2018.

[60] F. T. Zaal, K. Daigle, G. L. Gottlieb, and E. Thelen, "An unlearned principle for controlling natural movements," *Journal of Neurophysiology*, vol. 82, no. 1, pp. 255–259, 1999. DOI: 10.1152/jn.1999.82.1.255.

[61] S. Shaharudin, D. Zanotto, and S. Agrawal, "Muscle synergy during wingate anaerobic rowing test of collegiate rowers and untrained subjects," *International Journal of Sports Science*, vol. 4, pp. 165–172, 2014. DOI: 10.5923/j.sports.20140405.03.

[62] J. M. Inouye and F. J. Valero-Cuevas, "Muscle synergies heavily influence the neural control of arm endpoint stiffness and energy consumption," *PLOS Computational Biology*, vol. 12, pp. 1–24, 2016. DOI: 10.1371/journal.pcbi.1004737.

[63] A. Akhtar, L. J. Hargrove, and T. Bretl, "Prediction of distal arm joint angles from emg and shoulder orientation for prosthesis control," *2012 Annual International Conference of the IEEE Engineering in Medicine and Biology Society*, pp. 4160–4163, 2012. DOI: 10.1109/EMBC.2012.6346883.

[64] M. Merad, E. de Montalivet, M. Legrand, *et al.*, "Assessment of an automatic prosthetic elbow control strategy using residual limb motion for transhumeral amputated individuals with socket or osseointegrated prostheses," *IEEE Transactions on Medical Robotics and Bionics*, vol. 2, no. 1, pp. 38–49, 2020. DOI: 10.1109/TMRB.2020.2970065.

[65] J. Han, J. Chai, and M. Hayashibe, "Synergy emergence in deep reinforcement learning for full-dimensional arm manipulation," *IEEE Transactions on Medical Robotics and Bionics*, vol. 3, no. 2, pp. 498–509, 2021. DOI: 10.1109/TMRB.2021.3056924.

[66] G. Brockman, V. Cheung, L. Pettersson, *et al.*, "Openai gym," 2016. DOI: arXiv:1606.01540.

[67] G. Averta, C. Della Santina, E. Battaglia, F. Felici, M. Bianchi, and A. Bicchi, "Unvealing the principal modes of human upper limb movements through functional analysis," *Frontiers in Robotics and AI*, vol. 4, 2017. DOI: 10.3389/frobt.2017.00037.

[68] W. D. I. G. Dasanayake, R. A. R. C. Gopura, V. P. C. Dassanayake, and G. K. I. Mann, "Estimation of prosthetic arm motions using stump arm kinematics," *7th International Conference on Information and Automation for Sustainability*, pp. 1–6, 2014. DOI: 10.1109/ICIAFS.2014.7069615.

[69] M. Merad, É. de Montalivet, A. Roby-Brami, and N. Jarrassé, "Intuitive prosthetic control using upper limb inter-joint coordinations and imu-based shoulder angles measurement: A pilot study," *2016 IEEE/RSJ International Conference on Intelligent Robots and Systems (IROS)*, pp. 5677–5682, 2016. DOI: 10.1109/IROS.2016.7759835.

[70] S. Hochreiter and J. Schmidhuber, "Long short-term memory," *Neural Computation*, vol. 9, no. 8, pp. 1735–1780, 1997. DOI: 10.1162/neco.1997.9.8.1735.

[71] B. Stephens-Fripp, G. Alici, and R. Mutlu, "A review of non-invasive sensory feedback methods for transradial prosthetic hands," *IEEE Access*, vol. 6, pp. 6878–6899, 2018. DOI: 10.1109/ACCESS.2018.2791583.

[72] A. J. Metzger, A. W. Dromerick, R. J. Holley, and P. S. Lum, "Characterization of compensatory trunk movements during prosthetic upper limb reaching tasks," *Archives of Physical Medicine and Rehabilitation*, vol. 93, no. 11, pp. 2029–2034, 2012. DOI: 10.1016/j.apmr.2012.03.011.

[73] J. E. Cheesborough, L. H. Smith, T. A. Kuiken, and G. A. Dumanian, "Targeted muscle reinnervation and advanced prosthetic arms," *Seminars in Plastic Surgery*, vol. 29, no. 1, pp. 62–72, 2015. DOI: 10.1055/s-0035-1544166.

[74] A. J. Spiers, J. Cochran, L. Resnik, and A. M. Dollar, "Quantifying prosthetic and intact limb use in upper limb amputees via egocentric video: An unsupervised, at-home study," *IEEE Transactions on Medical Robotics and Bionics*, vol. 3, no. 2, pp. 463–484, 2021. DOI: 10.1109/TMRB.2021.3072253.

[75] B. H. Young, "The bionic-hand arms race: High-tech hands are complicated, costly, and often impractical," *IEEE Spectrum*, vol. 59, no. 10, pp. 24–30, 2022. DOI: 10.1109/MSPEC.2022.9915629.

[76] S. Mick, M. Lapeyre, P. Rouanet, *et al.*, "Reachy, a 3d-printed human-like robotic arm as a testbed for human-robot control strategies," *Frontiers in Neurorobotics*, vol. 13, 2019. DOI: 10.3389/fnbot.2019.00065.

[77] M. H. Ahmed, J. Chai, S. Shimoda, and M. Hayashibe, "Synergy-space recurrent neural network for transferable forearm motion prediction from residual limb motion," *Sensors*, vol. 23, no. 9, 2023. DOI: 10.3390/s23094188.

[78] M. Merad, E. de Montalivet, M. Legrand, *et al.*, "Assessment of an automatic prosthetic elbow control strategy using residual limb motion for transhumeral amputated individuals with socket or osseointegrated prostheses," *IEEE Transactions on Medical Robotics and Bionics*, vol. 2, no. 1, pp. 38–49, 2020. DOI: 10.1109/TMRB.2020.2970065.

[79] M. Merad, E. de Montalivet, M. Legrand, *et al.*, "Improving the control of prostheses in arm amputees with approaches based on motor coordination," *Computer Methods in Biomechanics and Biomedical Engineering*, vol. 22, no. sup1, S445–S447, 2019. DOI: 10.1080/10255842.2020.1714976.

[80] M. Santello, M. Flanders, and J. F. Soechting, "Postural hand synergies for tool use," *Journal of Neuroscience*, vol. 18, no. 23, pp. 10 105–10 115, 1998. DOI: 10.1523/JNEUROSCI.18-23-10105.1998.

[81] A. d'Avella and E. Bizzi, "Shared and specific muscle synergies in natural motor behaviors," *Proceedings of the National Academy of Sciences*, vol. 102, no. 8, pp. 3076–3081, 2005. DOI: 10.1073/pnas.0500199102.

[82] S. Chvatal and L. Ting, "Common muscle synergies for balance and walking," *Frontiers in Computational Neuroscience*, vol. 7, 2013. DOI: 10.3389/fncom.2013.00048.

[83] K. Kutsuzawa and M. Hayashibe, "Motor synergy generalization framework for new targets in multi-planar and multi-directional reaching task," *Royal Society Open Science*, vol. 9, no. 5, p. 211 721, 2022. DOI: 10.1098/rsos.211721.

[84] D. B. Popovic, M. B. Popovic, and T. Sinkjaer, "Life-like control for neural prostheses: "proximal controls distal"," *2005 IEEE Engineering in Medicine and Biology 27th Annual Conference*, pp. 7648–7651, 2005. DOI: 10.1109/IEMBS.2005.1616283.

[85] M. Merad, É. de Montalivet, A. Roby-Brami, and N. Jarrassé, "Intuitive prosthetic control using upper limb inter-joint coordinations and imu-based shoulder angles measurement: A pilot study," *2016 IEEE/RSJ International Conference on Intelligent Robots and Systems (IROS)*, pp. 5677–5682, 2016. DOI: 10.1109/IROS.2016.7759835.

[86] W. D. I. G. Dasanayake, R. A. R. C. Gopura, V. P. C. Dassanayake, and G. K. I. Mann, "Estimation of prosthetic arm motions using stump arm kinematics," *7th International Conference on Information and Automation for Sustainability*, pp. 1–6, 2014. DOI: 10.1109/ICIAFS.2014.7069615.

[87] J. Han, J. Chai, and M. Hayashibe, "Synergy emergence in deep reinforcement learning for full-dimensional arm manipulation," *IEEE Transactions on Medical Robotics and Bionics*, vol. 3, no. 2, pp. 498–509, 2021. DOI: 10.1109/TMRB.2021.3056924.

[88] E. Todorov, T. Erez, and Y. Tassa, "Mujoco: A physics engine for model-based control," *2012 IEEE/RSJ International Conference on Intelligent Robots and Systems*, pp. 5026–5033, 2012. DOI: 10.1109/IROS.2012.6386109.

[89] S. K. Yadav, K. Tiwari, H. M. Pandey, and S. A. Akbar, "Skeleton-based human activity recognition using convlstm and guided feature learning," *Soft Comput.*, vol. 26, no. 2, pp. 877–890, 2022. DOI: 10.1007/s00500-021-06238-7.

[90] R. Pascanu, C. Gulcehre, K. Cho, and Y. Bengio, "How to construct deep recurrent neural networks," *Proceedings of the Second International Conference on Learning Representations (ICLR 2014)*, 2014.

[91] T. A. Kuiken, G. Li, B. A. Lock, *et al.*, "Targeted muscle reinnervation for real-time myoelectric control of multifunction artificial arms," *JAMA*, vol. 301, no. 6, pp. 619–628, 2009. DOI: 10.1001/jama.2009.116.

[92] J. E. Cheesborough, L. H. Smith, T. A. Kuiken, and G. A. Dumanian, "Targeted muscle reinnervation and advanced prosthetic arms," *Seminars in Plastic Surgery*, vol. 29, no. 1, pp. 62–72, 2015. DOI: 10.1055/s-0035-1544166.

[93] S. Jönsson, K. Caine-Winterberger, and R. Brånemark, "Osseointegration amputation prostheses on the upper limbs: Methods, prosthetics and rehabilitation," *Prosthetics and Orthotics International*, vol. 35, no. 2, pp. 190–200, 2011. DOI: 10.1177/0309364611409003.

[94] A. Middleton and M. Ortiz-Catalan, "Neuromusculoskeletal arm prostheses: Personal and social implications of living with an intimately integrated bionic arm," *Frontiers in Neurorobotics*, vol. 14, 2020. DOI: 10.3389/fnbot.2020.00039.

[95] an Zbinden, P. Sassu, E. Mastinu, *et al.*, "Improved control of a prosthetic limb by surgically creating electro-neuromuscular constructs with implanted electrodes," *Science Translational Medicine*, vol. 15, no. 704, eabq3665, 2023. DOI: 10.1126/scitranslmed.abq3665.

[96] D. Farina, I. Vujaklija, R. Brånemark, *et al.*, "Toward higher-performance bionic limbs for wider clinical use," *Nature Biomedical Engineering*, vol. 7, pp. 473–485, 2023. DOI: 10.1038/s41551-021-00732-x.

[97] W. W. G. Sašo Jezernik and T. Sinkjaer, "Neural network classification of nerve activity recorded in a mixed nerve," *Neurological Research*, vol. 23, no. 5, pp. 429–434, 2001. DOI: 10.1179/016164101101198811.

[98] M. Desmurget, C. Prablanc, Y. Rossetti, *et al.*, "Postural and synergic control for three-dimensional movements of reaching and grasping," *Journal of Neurophysiology*, vol. 74, no. 2, pp. 905–910, 1995. DOI: 10.1152/jn.1995.74.2.905.

[99] J. F. Soechting and F. Lacquaniti, "Invariant characteristics of a pointing movement in man," *Journal of Neuroscience*, vol. 1, no. 7, p. 710 720, 1981. DOI: 10.1523/JNEUROSCI.01-07-00710.1981.

[100] M. H. Ahmed, K. Kutsuzawa, and M. Hayashibe, "Transhumeral arm reaching motion prediction through deep reinforcement learning-based synthetic motion cloning," *Biomimetics*, vol. 8, no. 4, 2023. DOI: 10.3390/biomimetics8040367.

Appendix A

Achievements

A.1 Journals

1. M. H. Ahmed, J. Chai, S. Shimoda, and M. Hayashibe, "Synergy-Space Recurrent Neural Network for Transferable Forearm Motion Prediction from Residual Limb Motion," *Sensors*, vol. 23, no. 9, pp. 4188, April 2023. DOI: 10.3390/s23094188.

2. M. H. Ahmed, K. Kutsuzawa, and M. Hayashibe, "Transhumeral Arm Reaching Motion Prediction through Deep Reinforcement Learning-Based Synthetic Motion Cloning," *Biomimetics*, vol. 8, no. 4, pp. 367, August 2023. DOI: 10.3390/biomimetics8040367.

Appendix B

Copyright Notice

This dissertation contains reprints from the author's original publications as follows:

1. Chapter 2, contains reprints from [77]. M. H. Ahmed, J. Chai, S. Shimoda, and M. Hayashibe, "Synergy-Space Recurrent Neural Network for Transferable Forearm Motion Prediction from Residual Limb Motion," *Sensors*, vol. 23, no. 9, April 2023.
   DOI: 10.3390/s23094188.

2. Chapter 3, contains reprints from [100]. M. H. Ahmed, K. Kutsuzawa, and M. Hayashibe, "Transhumeral Arm Reaching Motion Prediction through Deep Reinforcement Learning-Based Synthetic Motion Cloning," *Biomimetics*, vol. 8, no. 4, August 2023.
   DOI: 10.3390/biomimetics8040367.

Acknowledgements

Foremost, I would like to express my sincere gratitude to my advisor, Professor Mitsuhiro Hayashibe, for his unwavering support, guidance, and invaluable insights throughout the entire journey of my Ph.D. His expertise, encouragement, and commitment to excellence have been instrumental in shaping the direction and quality of this thesis.

Heartfelt appreciation is extended to my thesis committee members, Professor Takeshi Yamaguchi, Professor Mami Tanaka, and Professor Ahmed Chemori, for their constructive feedback, thoughtful suggestions, and expert evaluation, which greatly enriched the content and rigor of this work.

Special thanks go to Professor Shingo Shimoda, Dr. Kyo Kutsuzawa, Dr. Jia Zheng Chai, Dr. Wei Zhu, and Dr. Yonatan Hutabarat, whose collaboration and discussions significantly contributed to the depth and breadth of my research. Their perspectives and shared enthusiasm made the academic pursuit rewarding and intellectually stimulating. I am equally grateful to all my colleagues and members of the Neuro-Robotics Lab.

I extend a special acknowledgment to Dr. Ertuğrul Yalçın, Dr. Shiddiq Hashuro, and Dr. Muhammad Jehanzeb Khan for always listening to my banter and providing positive motivation.

Heartfelt appreciation is extended to my friends Dr. Ahmed Raza, Dr. Ali Haider, Dr. Ishfaq Ahmed, Dr. Fahad Iqbal, Dr. Sikander Azam, Majid Ansari, Dr. Anam Bhatti, Dr. Shreya Santra, Dr. Jowesh Gounder, Dr. Muhammad Salman Al Farisi, Atsushi Hamada, Takashi Yoshida, Amged Elshiekh, Adam Syammas Zaki, Chatrin Phunruangsakao, Hassan Matout, Tahara Momoka, Rabia Çelik, Hardiani Alexandera, Dr. Imane Sioud, Dr. Seohee Ashley Viguera, students at Sendai NIKA Highschool, Osamu Jinushi Sensei, Reimi Hayasaka, and Miss Cẩm Tú. They formed an invaluable support group throughout this academic journey. Their encouragement, understanding, camaraderie, and emotional support provided the foundation for me to navigate the challenges and triumphs of the doctoral journey.

This work would not have been possible without the collective contributions of all those mentioned above. Thank you for being an integral part of this academic endeavor.